1998

Coupling of baroclinic waves, cumulus convection, and surface processes

Weidong Jiang
Iowa State University

INFORMATION TO USERS

This manuscript has been reproduced from the microfilm master. UMI films the text directly from the original or copy submitted. Thus, some thesis and dissertation copies are in typewriter face, while others may be from any type of computer printer.

The quality of this reproduction is dependent upon the quality of the copy submitted. Broken or indistinct print, colored or poor quality illustrations and photographs, print bleedthrough, substandard margins, and improper alignment can adversely affect reproduction.

In the unlikely event that the author did not send UMI a complete manuscript and there are missing pages, these will be noted. Also, if unauthorized copyright material had to be removed, a note will indicate the deletion.

Oversize materials (e.g., maps, drawings, charts) are reproduced by sectioning the original, beginning at the upper left-hand corner and continuing from left to right in equal sections with small overlaps. Each original is also photographed in one exposure and is included in reduced form at the back of the book.

Photographs included in the original manuscript have been reproduced xerographically in this copy. Higher quality 6" x 9" black and white photographic prints are available for any photographs or illustrations appearing in this copy for an additional charge. Contact UMI directly to order.

UMI

A Bell & Howell Information Company
300 North Zeeb Road, Ann Arbor MI 48106-1346 USA
313/761-4700 800/521-0600

Coupling of baroclinic waves, cumulus convection, and surface processes

by

Weidong Jiang

A dissertation submitted to the graduate faculty
in partial fulfillment of the requirements for the degree of
DOCTOR OF PHILOSOPHY

Major: Meteorology
Major Professor: William J. Gutowski, Jr.

Iowa State University
Ames, Iowa
1998

Graduate College

Iowa State University

This is to certify that the Doctoral dissertation of

Weidong Jiang

has met the dissertation requirements of Iowa State University

Signature was redacted for privacy.

Committee Member

Signature was redacted for privacy.

Committee Member

Signature was redacted for privacy.

Committee Member

Signature was redacted for privacy.

Committee Member

Signature was redacted for privacy.

Major Professor

Signature was redacted for privacy.

For the Major Program

Signature was redacted for privacy.

For the Graduate College

TABLE OF CONTENTS

LIST OF FIGURES

LIST OF TABLES

ABSTRACT

This dissertation study, consisting of two papers, investigates the coupling of baroclinic waves, cumulus convection, and surface processes.

In the first paper, the role of convection in the dynamics of eddy life cycles is examined through numerical experiments using initial states that are baroclinically and conditionally unstable in midlatitudes. The location of wave-induced convection and its influence on the growing wave depends on how strongly the wave is coupled to the lower boundary through surface fluxes. For all three convective schemes used here, convective destabilization is favored in the wave's warm sector when there are no surface fluxes included in the simulation and in the cold sector when there are. Convection is also shallower when it occurs in the cold sector, though still precipitating. For simulations using Emanuel convection, the relatively shallow convection plays a central role in a water cycle wherein (1) evaporation gives moisture to the cold sector's boundary layer, (2) convection pumps some of the moisture into the lower troposphere above the boundary layer, (3) the large-scale circulation transports the moisture eastward and upward into the wave's warm sector, and (4) stable precipitation condenses the moisture into precipitation. The additional condensation catalyzes a more energetic life cycle by inducing stronger vertical motion and, hence, a greater conversion of available potential energy to kinetic energy. This enhancement, however, is parameterization-dependent, with the key factor being how much lower-tropospheric moistening a convection scheme produces.

The second paper of this dissertation is a theoretical, linear analysis of the moist instability of a baroclinic zonal flow with conditionally unstable stratification in the presence of surface temperature damping. In the two-dimensional continuous model on an f-plane, the effect of surface temperature damping is assumed to exponentially decrease with height, and the cumulus convective heating is parameterized in terms of either (1) eddy meridional velocity

or (2) eddy temperature at a certain level p_m which approximately is the top of the unstable PBL. The results showed that the moist unstable waves are modified by the effect of convective latent heating. With weak convection, the wave's structure does not change much while the wave's energy generation is hampered by the negative contribution of convection. In the presence of moderate convective heating, although the wave's energy's generation is decreased by convection, the wave adjusts its structure accordingly to minimize the negative effect of convection and keep growing. Strong convective heating invokes a non-Eady mode in the cloud region which separates and modifies the Eady mode in the upper and lower atmosphere.

GENERAL INTRODUCTION

Introduction

Although its amount is relatively small, water vapor is an important component of our atmosphere. Not only is it related to the hot topic of global warming, latent heat release during water vapor condensation is a major heating source for the atmosphere. Moisture condensation accompanying various weather systems affects the daily life of human beings, and the development of weather systems itself (for instance, midlatitude eddies) is affected by moisture condensation. Studies on water vapor in the atmosphere help to improve our understanding about weather and climate.

The linear theory of baroclinic instability developed from the pioneering work of Charney (1947) and Eady (1949) explains well propagating synoptic-scale disturbances in midlatitudes, and it can predict approximately the scale, growth, and structure of midlatitude cyclones. However, linear instability theory can not explain the eddy statistics of a general circulation model in which nonlinear processes exist (Gall, 1976). Since nonlinear effects are important in the mature and decay stages of eddy life cycles, baroclinic instability theory has been extended to the nonlinear regime by later studies such as that of Simmons and Hoskins (1978). Baroclinic instability has been shown by observational studies as a primary mechanism in maintaining the observed mean flow and atmospheric energetics.

One of the nonlinear processes pointed out by Gall (1976) that affects baroclinic growth is convective processes and the release of latent heat. The release of latent heat is usually considered to consist of two parts: cumulus convection and large-scale supersaturation. The importance of cumulus convection was first noticed in the

development of tropical large-scale disturbances (Riehl and Malkus, 1958, 1961; Yanai, 1961a,b). Cumulus convection supplies heat to drive the large-scale dynamics, and the large-scale system produces low-level moisture convergence to drive the cumulus convection. The unstable growth of a large-scale disturbance due to this cooperative interaction is referred as conditional instability of the second kind (CISK) (Charney and Eliassen, 1964; Ooyama, 1964). Wave-CISK theory gives a satisfactory description to large-scale equatorial waves (Hayashi, 1970), and it has also been used to explain the interaction between convection and extratropical waves (e.g., Rasmussen, 1979).

The importance of convection to the development of extratropical waves can be found in many case studies. Comparing synoptic analysis results with numerical forecast output of some observed storms, Tracton (1973) pointed out that cumulus convection plays a crucial role in initiating development through the release of latent heat in the vicinity of the cyclone center. Using synoptic analysis of the storm that battered the liner Queen Elizabeth II on 10 and 11 September 1978, Gyakum (1983a) suggested that the convection associated with the cyclone during its explosive deepening may have played a role similar to convection in tropical cyclogenesis. Potential vorticity analysis of the case (Gyakum, 1983b) further substantiated the CISK-like importance of convection in this explosive cyclone, which suggests the mechanism may be important in other explosively-developing extratropical cyclones. Ninomiya (1980) studied two typical cases of Baiu front and compared simulations for three different versions of his model: (1) no condensation, (2) large-scale condensation included, and (3) both large-scale condensation and convective adjustment included. The Baiu front was remarkably enhanced in the last model compared with other two, thus demonstrating the enhancement of the Asian subtropical front due to the thermodynamic influence of convection. Smith et al. (1984) investigated the influence of stable and convective latent heat release on synoptic-scale vertical motions during strong development of an extratropical cyclone. The results indicated that latent heating was not

significant early in the development of this cyclone, but its significance increased sharply as the cyclone grew and reached a maximum after 12 hours. The convective component dominated the vertical motions forced by latent heat release which in itself accounted for over 50% of the total upward vertical motion.

Gutowski et al. (1992) examined the interaction between moisture and baroclinic eddies through eddy life-cycle experiments. The numerical experiments were performed using a global, primitive equation model and initial states corresponded to climatological winter and summer zonal average states of the northern hemisphere. Focusing on large-scale supersaturation, the study showed the moisture condensation induced a faster evolution of the eddy life cycle by intensifying conversion from available potential to kinetic energy. The energetic analysis indicated that the influence of convection on wave dynamics was smaller than that of large-scale supersaturation. In the experiments, however, no conditional instability was generated in midlatitudes, so the experiments might have underestimated the effect of convection. The study also did not explore the influence of surface fluxes which were computed according to the bulk formulas. To further understand the role of convection in the development of baroclinic waves, in this thesis study, we have extended the work of Gutowski et al. (1992) focusing on the ability of waves to induce convection and convection's feedback on the waves. We have performed numerical experiments using climatological initial states with conditional instability in midlatitudes. A sophisticated paramterization of boundary layer physics was implemented in our model to facilitate examining the effect of surface fluxes, and three convection parameterization schemes were used to examine the sensitivity of the model results. Our study has revealed the important regulation of the boundary layer on the coupling of convection and baroclinic waves. Convection in our study played an important role in the wave's evolution and hydrological cycle, which is different from the traditional wave-CISK mechanism.

The fundamentals of baroclinic instability were delineated by Charney (1947) and Eady (1949) in elegant, analytical form. The beauty of analytical study is that it can explain a theory in simple, conceptual, and systematic ways. However, it is difficult to incorporate analytically the effect of convective heating into the baroclinic theory. Many studies have been performed to examine analytically the potential effect of convection on baroclinic instability (e.g., Tokioka 1973; Mak 1982, 1983, 1994; Moorthi and Arakawa 1985; Bannon 1986; Wang and Barcilon 1986; Emanuel et al. 1987; Fantini 1990; Balasubramanian and Yau 1994). Most of these analytical studies used a wave-CISK like parameterization, which assumes that the low-level convergence organizes the location and horizontal extent of convection. The degree of low-level convergence in these studies was measured by the large-scale, low-level vertical motion generated by the wave, either by itself or in conjunction with Ekman pumping. In the work of Emanuel et al. (1987) and Fantini (1990), the parameterization was modified slightly to a requirement that at each level in the atmosphere, the location of the wave's upward motion determined where moist convective effects modify the large-scale flow. In these studies, it is shown that convection tends typically to increase growth rates of the most unstable waves and shift the wavelength of maximum instability toward shorter waves.

In the second paper of this thesis work, we performed an analytical study on the effect of convection on baroclinic instability to extend the prior studies of this kind, motivated by the results of our numerical study. In the numerical study, wave-induced cumulus convection is more likely to occur where the wave-induced unstable boundary layer creates favorable conditions. In the winter, substantial surface fluxes and shallow convection are often observed in the unstable boundary layer formed by marine storms over the warm ocean (e.g., Kuo and Low-Nam, 1990; Kuo et al., 1991). To explore baroclinic instability for such cases, in this study, we parameterize convective heating by relating it to either the eddy meridional velocity or eddy temperature field that helps create the wave-induced unstable boundary layer, which distinguishes from the traditional wave-CISK

formulation of convective heating. Using our convective heating formulation with the Eady model, baroclinic instability exhibits some characteristics in our study not found in previous work.

Thesis Organization

This thesis contains two papers. The first paper presents the numerical study on the surface-flux regulation of the coupling between cumulus convection and baroclinic waves. In the first paper, relevant literature is first reviewed as the introduction, then the numerical model and initial conditions used in the study are described. After an introduction to the vertical temperature structure of a growing wave, the interaction of convection and eddy dynamics is examined by analyzing the results at different stages of the wave development. Last is a summary and discussion. This paper has been modified and published in the Journal of the Atmospheric Sciences (Gutowski and Jiang, 1998). Weidong Jiang was responsible for all the numerical computations presented in the paper, and his major contributions include implementing the Emanuel scheme into the PL/GD-AER global spectral model, modifying the Kuo scheme and the Grell scheme, and performing the trajectory analysis.

The instability study on coupling between cumulus convection and baroclinic waves is presented as the second paper of this thesis. After reviewing relevant literature, the model formulation is described, followed by the model results and analysis. Similarly, the summary and discussion concludes the paper.

A general conclusion is given after the second paper. Some mathematical details of the two papers can be found in Appendices.

References

Balasubramanian, G., and M. K. Yau, 1994: Baroclinic instability in a two-layer model with parameterized slantwise convection. *J. Atmos. Sci.*, **51,** 971-990.

Bannon, P. R., 1986: Linear development of quasi-geostrophic baroclinic disturbances with condensational heating. *J. Atmos. Sci.*, **43**, 2261-2274.

Charney, J. G., 1947: The dynamics of long waves in a baroclinic westerly current. *J. Meteor.*, **4**, 135-163.

Charney, J. G., and A. Eliassen, 1964: On the growth of the hurricane depression. *J. Atmos. Sci.*, **21**, 68-75.

Eady, E. T., 1949: Long waves and cyclone waves. *Tellus*, **1**, 33-52.

Emanuel, K. A., M. Fantini and A. J. Thorpe, 1987: Baroclinic instability in an environment of small stability to slantwise moist convection. Part I: Two-dimensional models. *J. Atmos. Sci.*, **44,** 1559-1573.

Fantini, M., 1990: Nongeostrophic corrections to the eigensolutions of a moist baroclinic instability problem. *J. Atmos. Sci.*, **47,** 1277-1287.

Gall, R., 1976: A comparison of linear baroclinic instability theory with the eddy statistics of a general circulation model. *J. Atmos. Sci.*, **33**, 349-373.

Gutowski, W. J., L. E. Branscome, and D. Stewart, 1992: Life cycle of moist baroclinic eddies. *J. Atmos. Sci.*, **49**, 306-319.

Gutowski, W. J. and W. Jiang, 1998: Surface-flux regulation of the coupling between cumulus convection and baroclinic waves. *J. Atmos. Sci.*, **55**, 940-953.

Gyakum, J. R., 1983a: On the evolution of the QE II storm. I: Synoptic aspects. *Mon. Wea. Rev.*, **111**, 1137-1155.

Gyakum, J. R., 1983b: On the evolution of the QE II storm. II: Dynamic and thermodynamic structure. *Mon.Wea. Rev.*, **111**, 1156-1173.

Kuo, Y.-H., and S. Low-Nam, 1990: Prediction of nine explosive cyclones over the Western Atlantic Ocean with a regional model. *Mon. Wea. Rev.*, **118**, 3-25.

Kuo, Y.-H., M. A. Shapiro and E. G. Donall, 1991: The interaction between baroclinic and diabatic processes in a numerical simulations of a rapidly intensifying extratropical marine cyclone. *Mon. Wea. Rev.*, **119**, 368-284.

Hayashi, Y., 1970: A theory of large-scale equatorial waves generated by condensation heat and accelerating zonal wind. *J. Meteor. Soc. Japan*, **48**, 140-160.

Jiang, W., 1994: The role of convection in eddy life cycles. M.S. Thesis, Iowa State University, 86 pp.

Mak, M., 1982: On moist quasi-geostrophic baroclinic instability. *J. Atmos. Sci.*, **39**, 2028-2037.

Mak, M., 1983: On moist quasi-geostrophic baroclinic instability in a general model. *J. Atmos. Sci. Sin.*, **B26**, 850-864.

Mak, M., 1994: Cyclogenesis in a conditionally unstable moist baroclinic atmosphere. *Tellus*, **46A**, 14-33.

Moorthi, S., and A. Arakawa, 1985: Baroclinic instability with cumulus heating. *J. Atmos. Sci.*, **42**, 2007-2031.

Ninomiya, K., 1980: Enhancement of Asian subtropical front due to thermodynamic effects of cumulus convection. *J. Meteor. Soc. Japan*, **58**, 1-15.

Ooyama, K., 1964: A dynamical model for the study of tropical cyclone development. *Geofis. Intern.*, **4**, 187-198.

Rasmussen, E., 1979: The polar low as an extratropical CISK disturbance. *Quart. J. Roy. Meteor. Soc.*, **105**, 531-550.

Riehl, H., and J. S. Malkus, 1958: On the heat balance in the equatorial trough zone. *Geophysica*, **6**, 503-538.

Riehl, H., and J. S. Malkus, 1961: Some aspects of hurricane Daisy, 1961. *Tellus*, **13**, 181-213.

Simmons, A. J. and B. J. Hoskins, 1978: The life cycles of some nonlinear baroclinic waves. *J. Atmos. Sci.*, **35**, 414-432.

Smith, P. J., P. M. Dare, and S-J. Lin, 1984: The impact of latent heat release on synoptic-scale vertical motions and the development of an extratropical cyclone system. *Mon. Wea. Rev.*, **112**, 2421-2430.

Tokioka, T., 1973: A stability study of medium-scale disturbances with inclusion of convective effects. *J. Meteor. Soc. Japan*, **51**, 1-10.

Tracton, M. S., 1973: The role of cumulus convection in the development of extratropical cyclones. *Mon. Wea. Rev.*, **101**, 573-593.

Wang, B., and A. Barcilon, 1986: Moist stability of a baroclinic zonal flow with conditionally unstable stratification. *J. Atmos. Sci.*, **43**, 705-719.

Yanai, M., 1961a: A detailed analysis of typhoon formation. *J. Meteor. Soc. Japan*, **39**, 187-214.

Yanai, M., 1961b: Dynamical aspects of typhoon formation. *J. Meteor. Soc. Japan*, **39**, 283-309.

SURFACE-FLUX REGULATION OF THE COUPLING BETWEEN CUMULUS CONVECTION AND BAROCLINIC WAVES: RESULTS OF THE NUMERICAL STUDY

A paper published in the Journal of the Atmospheric Sciences

William J. Gutowski Jr. and Weidong Jiang

Introduction

The release of latent heat during condensation is an important heating source for the atmosphere. The effect of condensation on the development of midlatitude eddies can be significant and is suggested by early instability analyses and many case studies. A previous study on the life cycles of moist baroclinic eddies (Gutowski et al. 1992, hereafter GBS) helped to delineate the role of moisture condensation in large-scale, non-linear baroclinic instability. One mechanism of water vapor condensation in the atmosphere is convection. In GBS, convection had a nearly negligible role in the life cycle. However, convection is an important source of heat to the atmosphere, so we have performed further study, focusing on conditions more conducive to the development of convection than the midlatitude climatology used in GBS. As in GBS, we retain a focus on climatological development and the largest amplitude waves in the atmosphere, synoptic and planetary-scale waves, and so we do not stray very far from climatological initial conditions. Thus our focus is on the relationship between convection and the growing, baroclinic waves that attain largest amplitude in the atmosphere, and not on events such as explosive development or polar cyclones, which tend to be smaller in scale. We also focus on the potential role of eddy moisture transport in fostering convection.

Many case studies have concluded that convective condensation was crucial in the development of the extratropical cyclones examined. Tracton (1973) compared synoptic analyses with numerical forecasts for twenty-one intense cyclones occurring east of the Rocky Mountains, concluding that cumulus convection played a critical role in initiating development through the release of latent heat in the vicinity of the cyclone center. However, the cases he chose were close to a source of warm moist air, the Gulf of Mexico, thus making them particularly susceptible to the generation of the convective instability and perhaps not representative of general climatological behavior.

Gyakum (1983a, 1983b) analyzed the explosive development of the "QE II" storm of 10-11 September 1978, and hypothesized that a CISK-like mechanism (Charney and Eliassen 1964; Ooyama 1964) operated in which relatively weak baroclinic forcing organized convective heating effects on a scale comparable to the cyclone itself. He further hypothesized that the mechanism may be important to other explosively developing extratropical cyclones. A case study of an extratropical cyclone by Smith et al. (1984) found that convective heating played a dominant role in forcing cyclone-scale vertical motions during the period of rapid development.

Many analytic studies have also been performed that examine the potential effect of convection on baroclinic instability (e.g., Tokioka 1973; Mak 1982, 1983, 1994; Moorthi and Arakawa 1985; Bannon 1986; Wang and Barcilon 1986; Emanuel et al. 1987; Fantini 1990; Balasubramanian and Yau 1994). Typically, these studies find that convection tends to increase growth rates of the most unstable waves and shift the wavelength of maximum instability toward shorter waves. A common theme in most of these analytic studies is an assumption that the low-level convergence organizes the location and horizontal extent of convection. The degree of low-level convergence in these studies is measured by the large-scale, low-level vertical motion generated by the wave, either by itself or in conjunction with Ekman pumping. In the work of Emanuel et al. (1987) and Fantini (1990), this prescription is

modified slightly to a requirement that at each level in the atmosphere, the location of the wave's upward motion determines where moist convective effects modify the large-scale flow.

The results of the study here will suggest that an additional factor for theoretical study to consider is how the wave and associated surface heat fluxes condition the planetary boundary layer as the wave transports warm air and cold air meridionally. An initial indication of this can be seen by comparing the distribution of convection as the wave nears maximum amplitude in two of the life-cycle simulations (Fig. 1.1), described more completely in later sections. The only difference in the configurations of these two runs is that one includes interaction with the underlying surface (i.e., surface fluxes of heat, moisture and momentum) and the other does not. Both simulations resemble cases of observed behavior. When surface fluxes are included, convection occurs near the warm front and in the cool air between the warm and cold fronts, similar to behavior observed in case studies by Kuo and Low-Nam (1990) and Kuo et al. (1991). When surface fluxes are not included, much (though not all) of the convection occurs near and ahead of the cold front, similar to behavior observed in case studies by Yau and Jean (1989) and Chang et al. (1996), which also observed substantial convection in the vicinity of the cold front. This difference in behavior provides a further motivation for the life-cycle studies reported here.

We have performed several numerical experiments that are an extension of GBS, focusing on initial states that are conditionally unstable in midlatitudes. A brief description of the model is given in Section 2, including upgrades and additions to the version used in GBS. General characteristics of the initial conditions for the life cycle computations are also described in this section. To aid later discussion, Section 3 reviews the vertical temperature structure of growing waves with and without surface heat fluxes present. We then present an analysis of convection during the early (Section 4) and mature (Section 5) stages of the eddy life cycle. Section 6 gives a discussion and summary of the results.

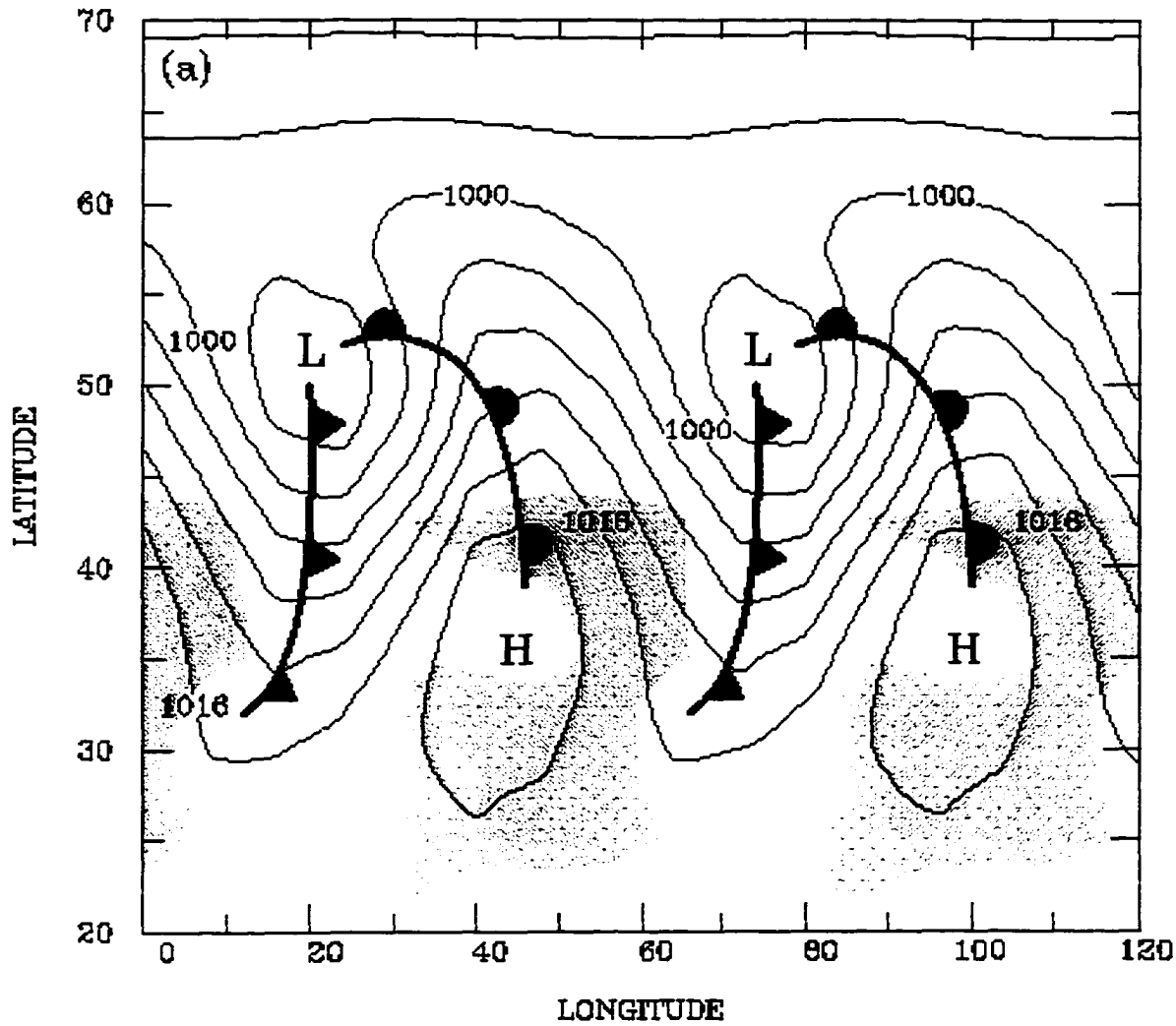

Figure 1.1(a) Distribution of convective heating (shaded area), surface pressure [hPa] and location of fronts as the primary wave in its life-cycle simulation nears maximum amplitude at the end of simulation day 10. The simulation includes surface fluxes.

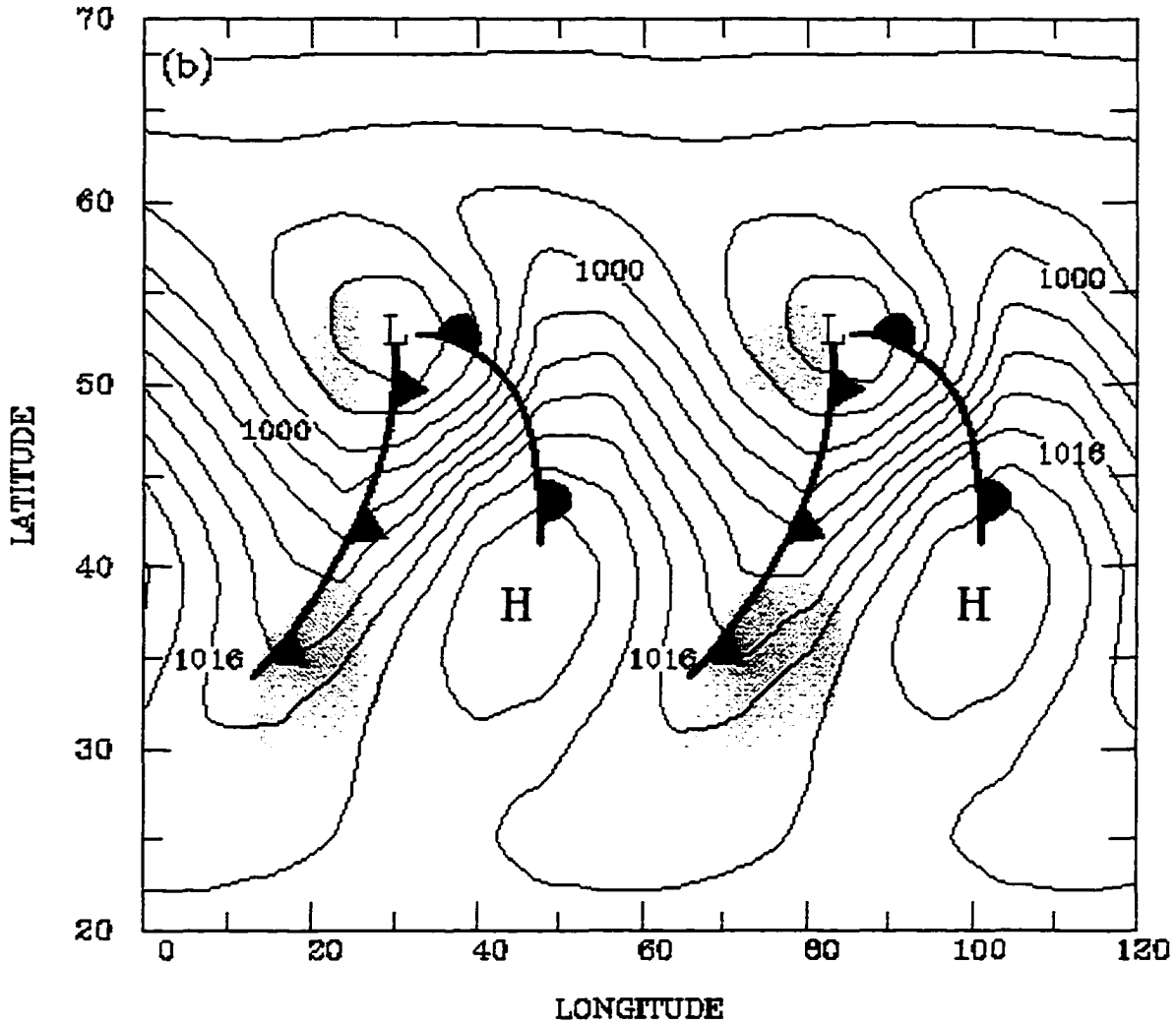

Figure 1.1(b) Same as Fig. 1.1(a) except the simulation does not includes surface fluxes.

Model and initial conditions

The model is a primitive equation, global spectral model (GSM) adapted from the National Center for Environmental Prediction's GSM, the essence of which is described in Branscome et al. (1989) and GBS. Most features of the model simulations performed by GBS are the same here. Thus, model runs include only the zonal average state, a fundamental zonal wave number P and the fundamental wave's next two harmonics (e.g. wave numbers 0, 7, 14, and 21 for P=7). We assume symmetry about the equator and resolve latitudinal structure with a spectral truncation in the meridional direction equivalent to rhomboidal 30. The lower boundary is an ocean-covered surface. In this sense the model is more representative of the Southern Hemisphere than the Northern Hemisphere. The surface temperature is equal to the air temperature of the lowest layer of the initial state and does not change throughout the experiment. The latter property is implied by the oceanic lower boundary.

There are two principal differences between the version of the model used by GBS and that used here. First, effects of the planetary boundary layer (PBL) are simulated using parameterizations developed by Troen and Mahrt (1986) in which surface fluxes are represented by similarity theory and turbulent diffusivities above the surface layer are expressed by bulk similarity and matching conditions at the top of the surface layer. To accommodate the upgraded PBL scheme, the model resolves vertical structure using 18 sigma layers, with highest resolution near the surface. Test computations using more and fewer layers show that this resolution is sufficient for our purposes (Jiang, 1994). Several layers are also included in the model stratosphere to ensure that an unrealistic wave structure will not develop there that might contaminate tropospheric dynamics.

The other principal difference is the addition of a convection parameterization developed by Emanuel (1991), used for most of the simulations reported here. (More specifically, we use

version 1.25 of the scheme.) For comparison, we have also performed a few simulations using the scheme developed by Grell (1993), that is an upgrade of the Grell et al. (1991) scheme used in GBS, and the model's original Kuo (1974) scheme. A comparison of results using each of the schemes helps to determine the sensitivity of the behavior observed here to the convection parameterization used.

The Emanuel scheme is based on ensembles of convective updrafts and downdrafts. A key factor in the Emanuel scheme is that it requires positive buoyancy for air parcels lifted from the surface to cloud base, which is defined as the first model level above the parcels' lifting condensation level (LCL). Closely associated with this requirement is a stipulation that parcel uplift leading to convection must occur in a non-stable, or well-mixed, PBL. The PBL turbulence implied in this situation can be viewed as providing the mechanism lifting a parcel to its level of free convection. The scheme also requires the atmosphere to contain convective available potential energy (CAPE) for the initiation of convection.

When using the Grell scheme here, we have made one modification to allow the growing, small-amplitude wave to induce midlatitude convection. The Grell scheme evaluates the potential for convection in part by searching between the surface and upper troposphere for the maximum in the environment's moist static energy

$$H = C_p T + Lq + gz \quad , \qquad (1)$$

where C_p is the heat capacity of air at constant pressure, T is temperature, L is the latent heat of vaporization, q is specific humidity, g is gravitational acceleration and z is distance from the surface. Designating the pressure level of max(H) as p_{max}, the potential for convection exists in the Grell scheme if

$$\max(H) > H_{sat} \qquad \text{for some } p \in [p_{max} - 250 \text{ hPa}, p_{max}] \quad , \qquad (2)$$

where H_{sat} is computed using the environmental profiles in (1) but with q replaced by its saturation value. For the initial midlatitude environment, max(H) occurs in the upper troposphere and (2) is not satisfied. As the wave grows, it produces a secondary maximum near the surface, but the standard Grell scheme does not apply condition (2) to this maximum, so no midlatitude convection occurs before the wave reaches its maximum amplitude. We modified the Grell scheme to apply the test (2) using the secondary max(H) produced by the wave in the lower troposphere. With this modification, the growing wave induces midlatitude convection.

We also modified the Kuo scheme in order to allow the growing, but small-amplitude wave to provoke midlatitude convection. In this case. we reduced the critical moisture convergence the scheme requires to initiate convection to just 2% of its standard value. Also, although the Kuo scheme does not explicitly require an unstable PBL, it does check for positive parcel buoyancy at cloud base, which is again the first model layer above the LCL. Positive buoyancy at cloud base can occur more readily if the PBL is isentropic rather than dry-convectively stable, so that like the Emanuel scheme, the Kuo scheme favors a well-mixed boundary layer.

The initial states used in our experiments correspond roughly to the climatological, Southern Hemisphere winter and summer zonal average states for temperature and zonal wind. Specific humidity was modified from climatology to allow midlatitude conditional instability. Figure 1.2 shows distributions of zonal wind, temperature, specific humidity and saturation equivalent potential temperature for the model's standard winter case. Compared to the winter case, the summer case (not shown) has a weaker westerly jet and near-surface meridional temperature gradient and, accordingly, weaker north-south moisture gradient. The region of potential convective instability extends farther into midlatitudes in the winter conditions state,

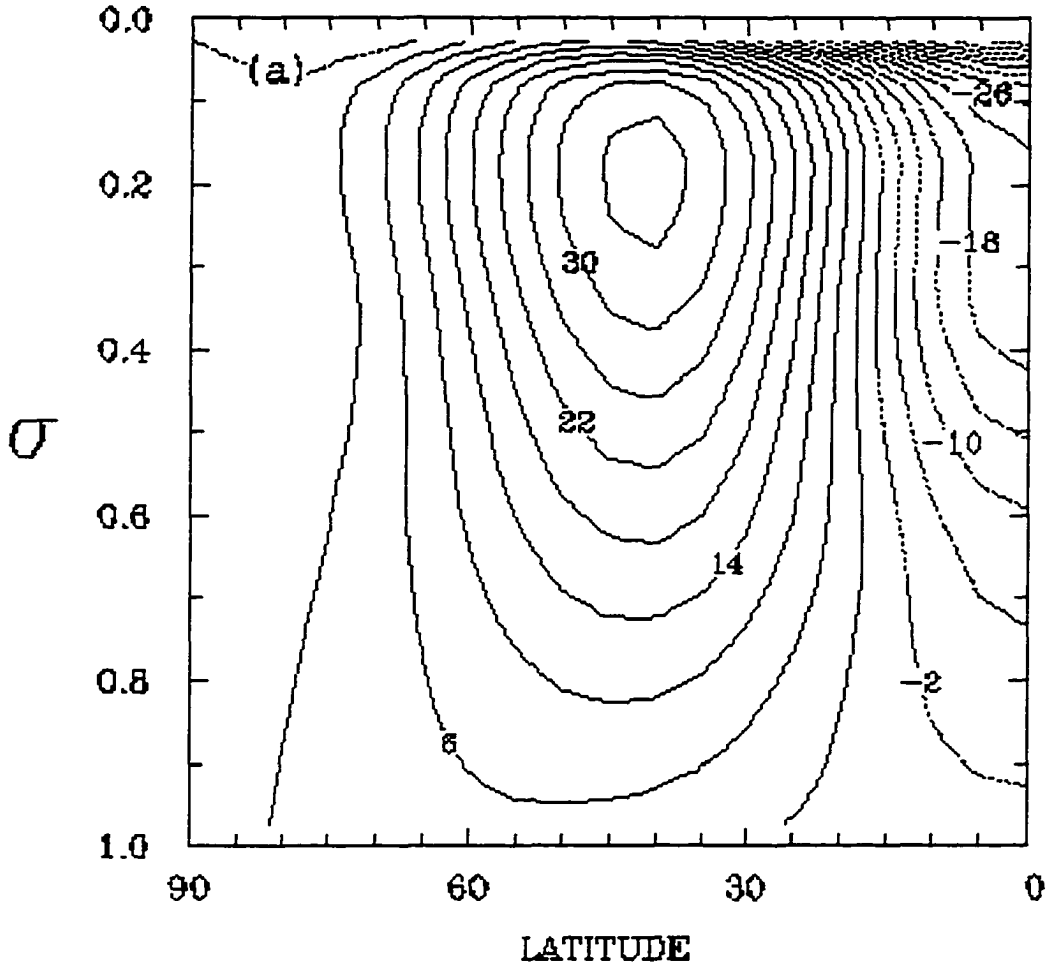

Figure 1.2(a) Standard, winter-condition's zonal-average state for zonal wind [m s^{-1}].

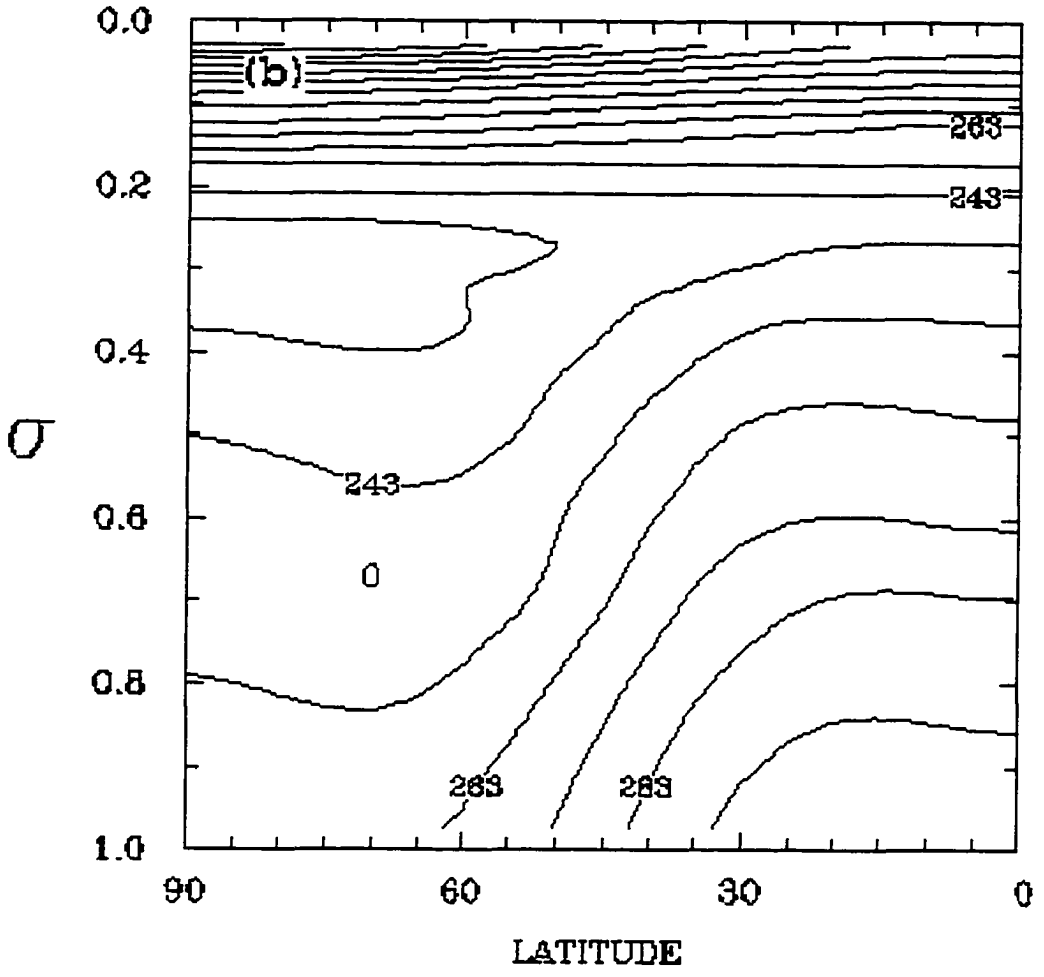

Figure 1.2(b) Standard, winter-condition's zonal-average state for temperature [K].

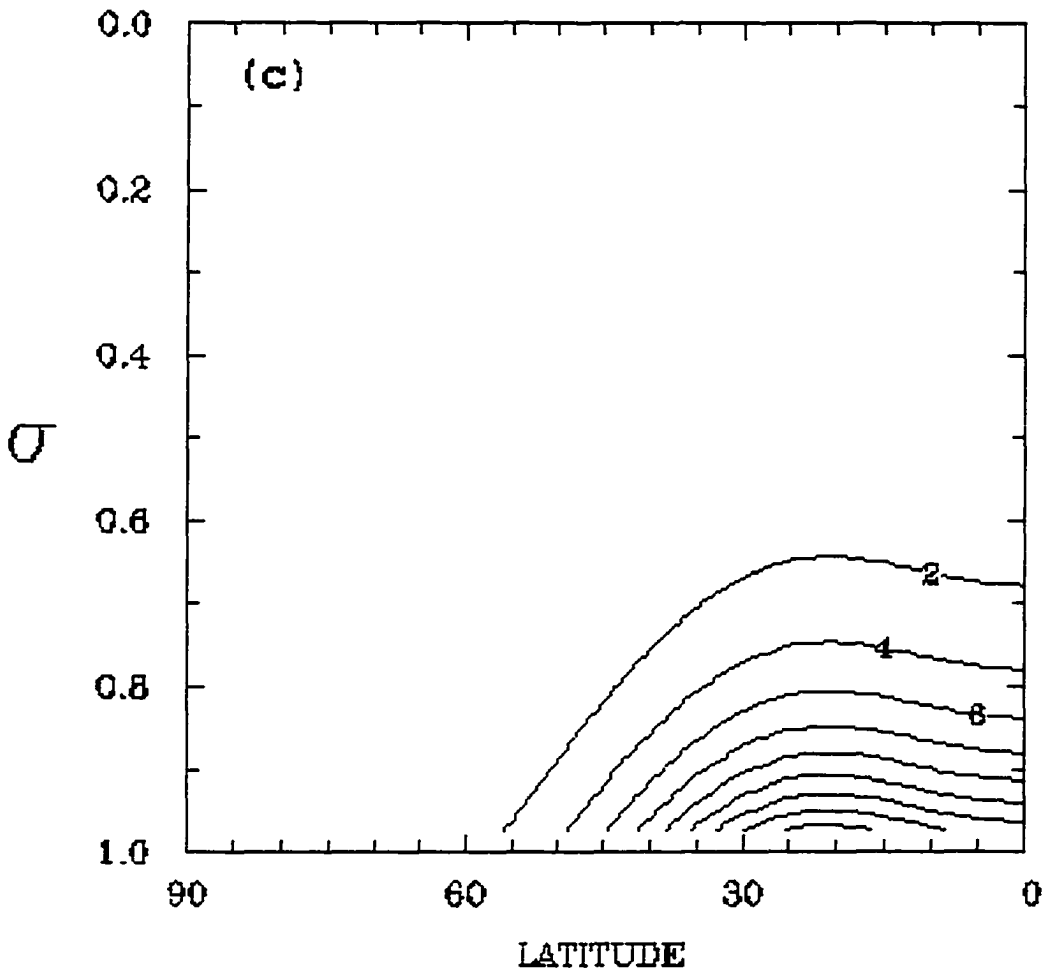

Figure 1.2(c) Standard, winter-condition's zonal-average state for specific humidity. The contour unit is [g kg^{-1}].

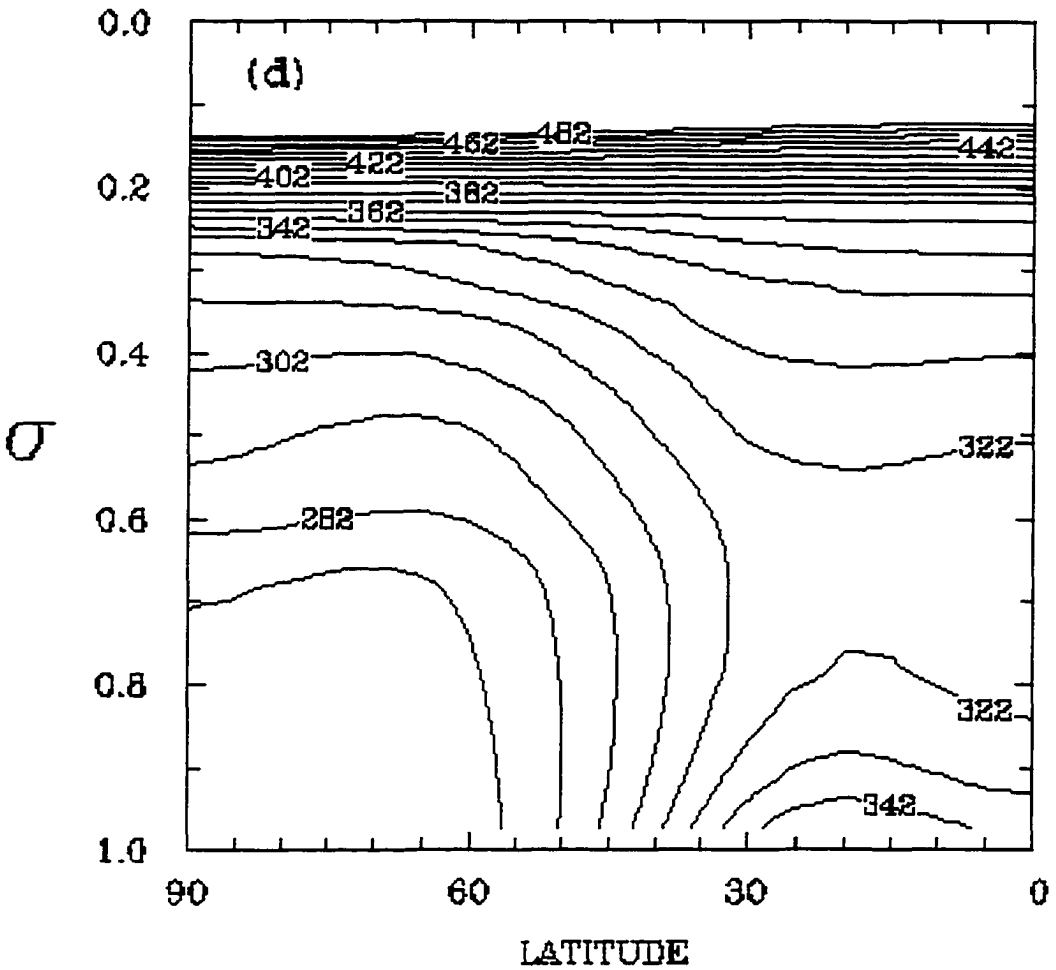

Figure 1.2(d) Standard, winter-condition's zonal-average state for saturation equivalent potential temperature [K].

so we give more attention here to simulations using that initial condition. The method used to ensure that our initial states are balanced is given by Branscome et al. (1989).

The waves in our experiments are initiated with a temperature perturbation superimposed on the balanced zonal mean state. The temperature perturbation has a maximum amplitude in the lowest layer and decreases exponentially with height. The wave draws available potential energy (APE) from the zonal mean flow. In several days, a nearly exponentially growing wave emerges. Eventually nonlinear effects diminish the growth rate, and the eddy ultimately reaches a maximum amplitude (e.g., GBS). From that point, eddy kinetic energy decreases, completing the life cycle. A second life cycle may ensue. During the eddy life cycle, the energy transfer shows the usual path for baroclinically unstable waves: energy flows from zonal APE to eddy APE and then eddy kinetic energy.

We ran simulations for several different fundamental waves. Typically zonal wavenumber 7 was the most rapidly growing and energetic, and it produced the strongest convective heating, so our discussion focuses on experiments in which zonal wavenumber 7 is perturbed. We also performed the experiments in which we perturbed wavenumber 6, wavenumber 12, or wavenumber 15 in order to obtain a more complete picture of wave-convection interactions.

In the following sections, we examine the interaction of convection and eddy dynamics at different stages. The early stage is defined as the time period from the beginning to the day on which eddy kinetic energy reaches 10% of its eventual maximum. For example, the early stage of wavenumber 7 is the period from day 0 to through day 7. The mature stage is defined as the rest life cycle after the early stage.

Temperature structure of growing waves

Analysis of the simulation output is aided by considering the vertical temperature structure of growing, baroclinically unstable waves. Figure 1.3 shows schematically profiles of potential temperature θ versus height in the growing wave's warm and cold sectors. The background, zonal-average potential temperature $[\theta]$ in each case is the average of the warm and cold profiles. In the lower panel, we assume that there are no fluxes of heat between the surface and the atmosphere. The magnitude of the eddy temperature field, $\theta - [\theta]$, increases toward the surface, consistent with typical linear instability computations for an external mode (e.g., Green 1960; Card and Barcilon 1982). As suggested by the figure, if the magnitude of the eddy temperature field is large enough, then an unstable boundary layer ($d\theta/dz < 0$) will develop at the surface in the warm sector. The boundary layer in the cold sector will be stable.

When surface fluxes are included, there will be an exchange of heat between the surface and the atmosphere. The surface in our simulations is the ocean, which we assume has unchanging temperature over the course of the life cycle simulation. Surface heat fluxes tend to reduce the difference between surface and air temperatures, so that the eddy temperature field is strongly damped near the surface (e.g., Branscome et al, 1989). As a consequence, an unstable boundary layer can develop in the wave's cold sector, while the warm sector remains stable (Fig. 1.3(a)). This effect of surface fluxes on the wave's near-surface temperature structure affects the distribution of convection using the Emanuel parameterization, which requires a non-stable boundary layer.

The difference in the wave's temperature structure between Figs. 1.3(a) and (b) also affects where an air parcel rising from the surface will be warmer than its surrounding environment, thus giving it positive buoyancy. Dashed lines in Fig. 1.3 are for a non-

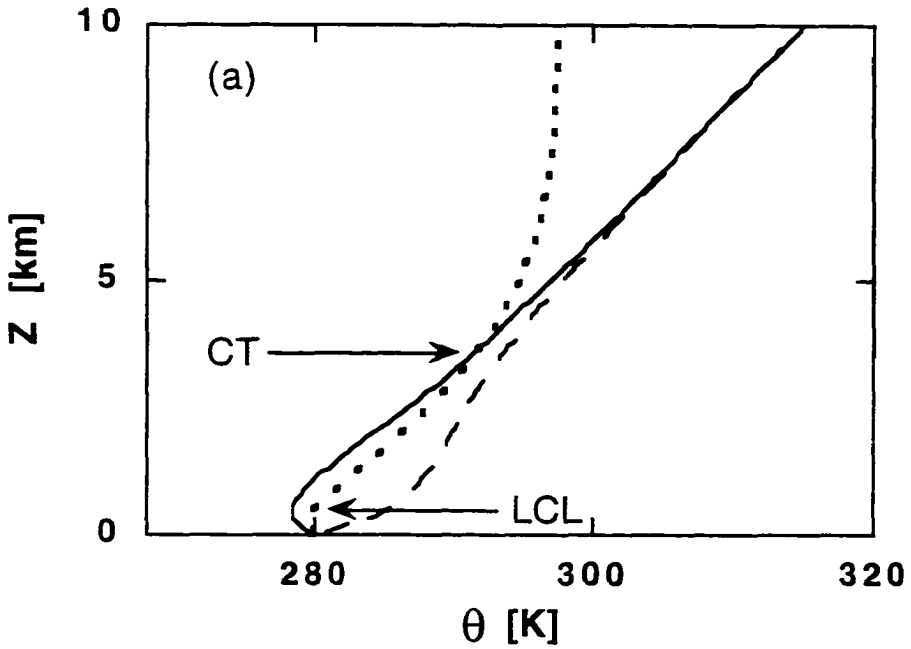

Figure 1.3(a) Schematic diagram of potential temperature vs. height in the warm (dashed line) and cold (solid line) sector of growing waves when surface fluxes are included in the simulation. Dotted lines are paths followed by non-entraining air parcels lifted from the surface through their lifting condensation level (LCL) and cloud top (CT).

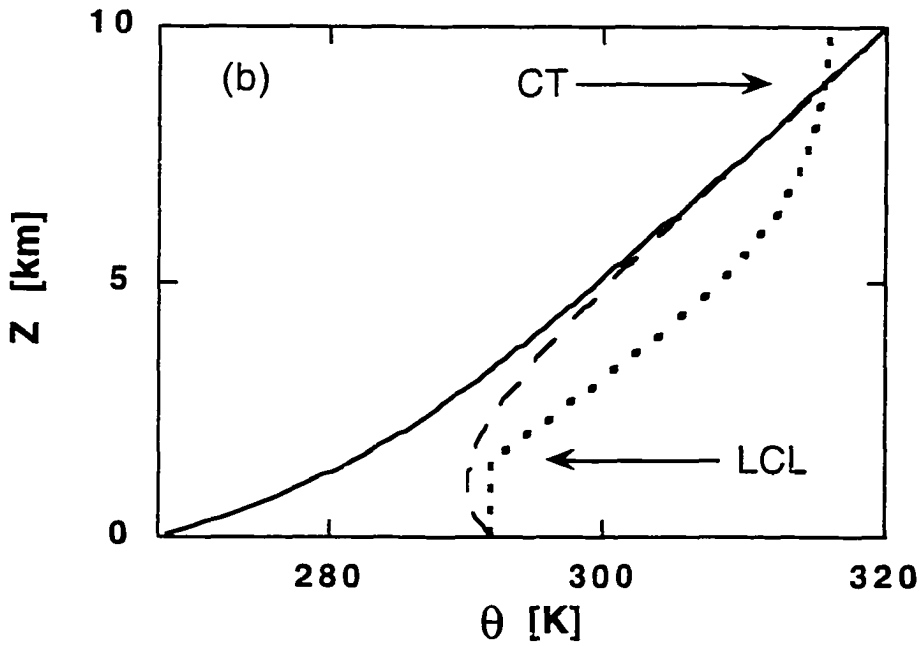

Figure 1.3(b) Same as Fig. 1.3(a) except surface fluxes are not included in the simulation.

entraining parcel that rises from near-surface along a dry adiabat until it reaches saturation, at which point further rising occurs along a moist adiabat. When surface heat fluxes are included, non-entraining air parcels rising from the surface in either the warm or the cold sector will follow approximately the same path since near-surface air departs little from the zonal mean. Assuming that an unstable planetary boundary layer produces an isentropic environmental temperature profile near the surface, a rising parcel in Fig. 1.3(a)'s cold sector will have positive buoyancy between its LCL and its cloud top (CT), defined here as the level where the

non-entraining parcel becomes cooler than the environment. Positive buoyancy in this case is less likely to occur in the warm sector. In contrast, when there are no surface fluxes, only parcels rising in the warm sector are likely to attain positive buoyancy. Note also that convective available potential energy is proportional to the vertically integrated positive buoyancy (e.g., Holton 1992). Thus, in Fig. 1.3, the locations where the growing wave is increasing CAPE and thus causing convective destabilization depends on whether or not surface heat fluxes are present.

Early stage

The results shown in Figure 1.1 are from the mature phase of two life-cycle simulations. An understanding of why these differences occur can be found by examining the early stage of these and similar simulations, bearing in mind the discussion of the previous section. Using the Emanuel scheme with or without surface fluxes, the strongest convective heating in midlatitudes during the early stage occurs in the lower atmosphere (Fig. 1.4) and has a wave-like longitudinal structure (Figs. 1.5 and 1.6) as a consequence of the growing wave's influence on the distribution of convection.

Figure 1.5 shows the relationship between convective heating and features of the growing wave at the end of day 7 in the wavenumber 7 simulation with surface fluxes included. Consistent with the discussion in Section 3, the moist convection occurs in the cold sector of the wave, where in the presence of surface heat flux, the boundary layer has become dry convectively unstable. Figure 1.6 shows the same relationships for a simulation identical to that producing Fig. 1.5, but with no surface fluxes included. Again consistent with Section 3, the moist convection in this simulation occurs in the warm sector, which now has the unstable boundary layer. It also occurs primarily in the region of positive low-level vertical motion, consistent with the assumption coupling convection to low-level upward motion that

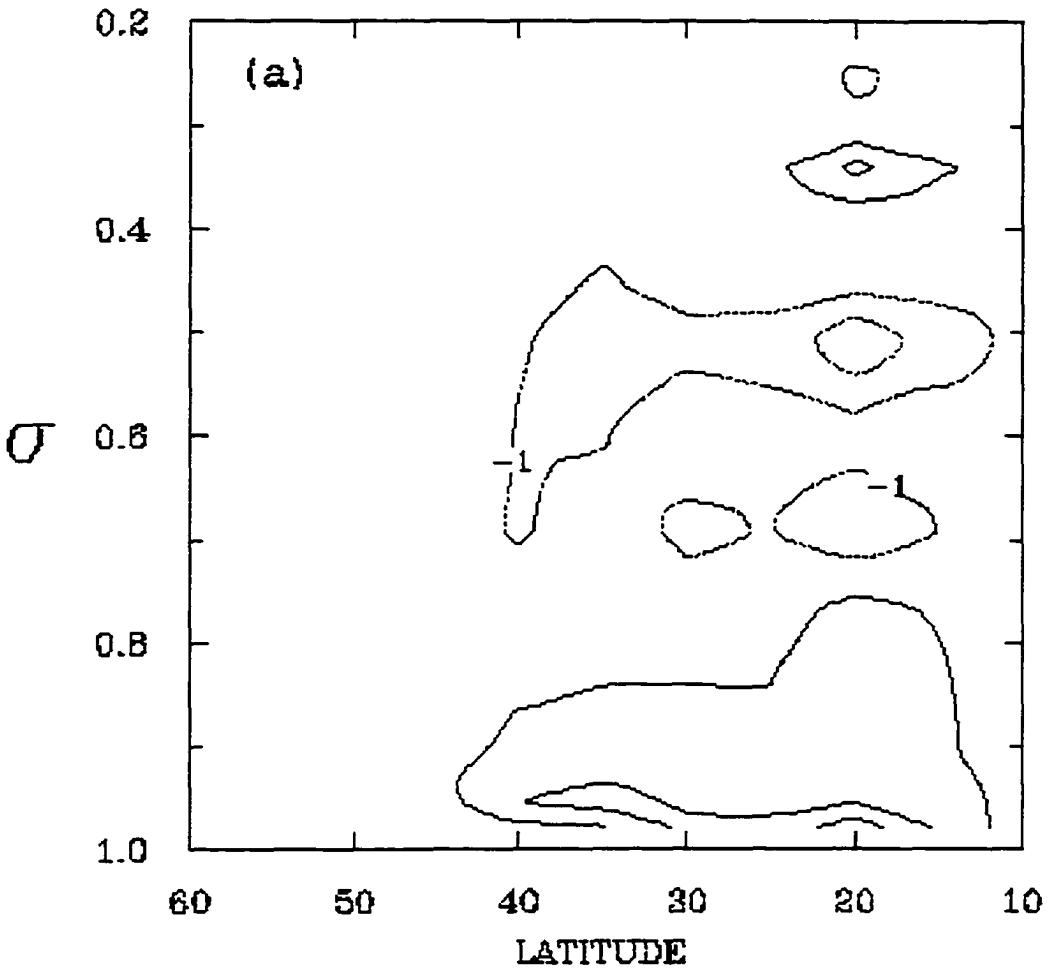

Figure 1.4(a) Latitude-height cross-section of convective heating produced by the Emanuel scheme during the last hour of day 7 for the wavenumber 7 run that includes surface fluxes. The unit is 10^{-1} K day^{-1} and the contour interval is 2 units, with solid contours denoting positive values.

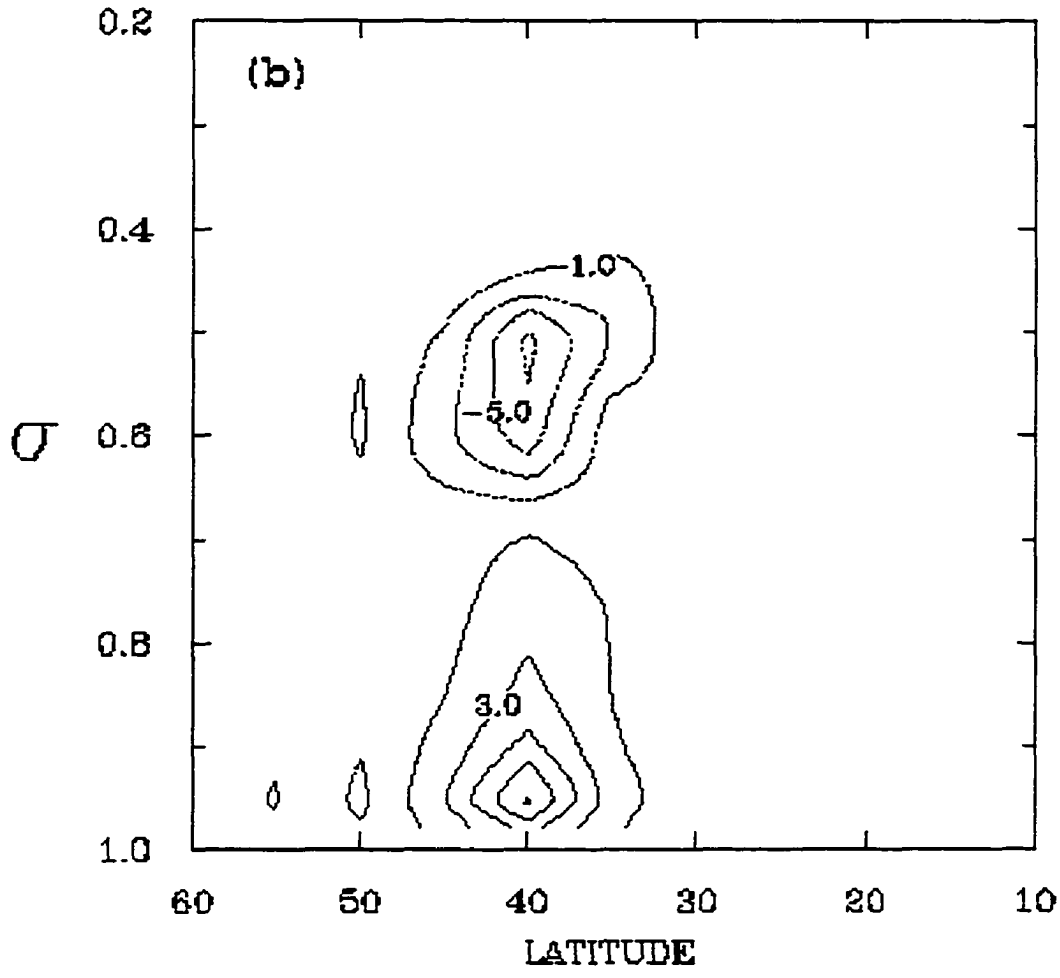

Figure 1.4(b) Like Fig. 4(a) except the run does not include surface fluxes, and the contour unit is 10^{-2} K day^{-1}.

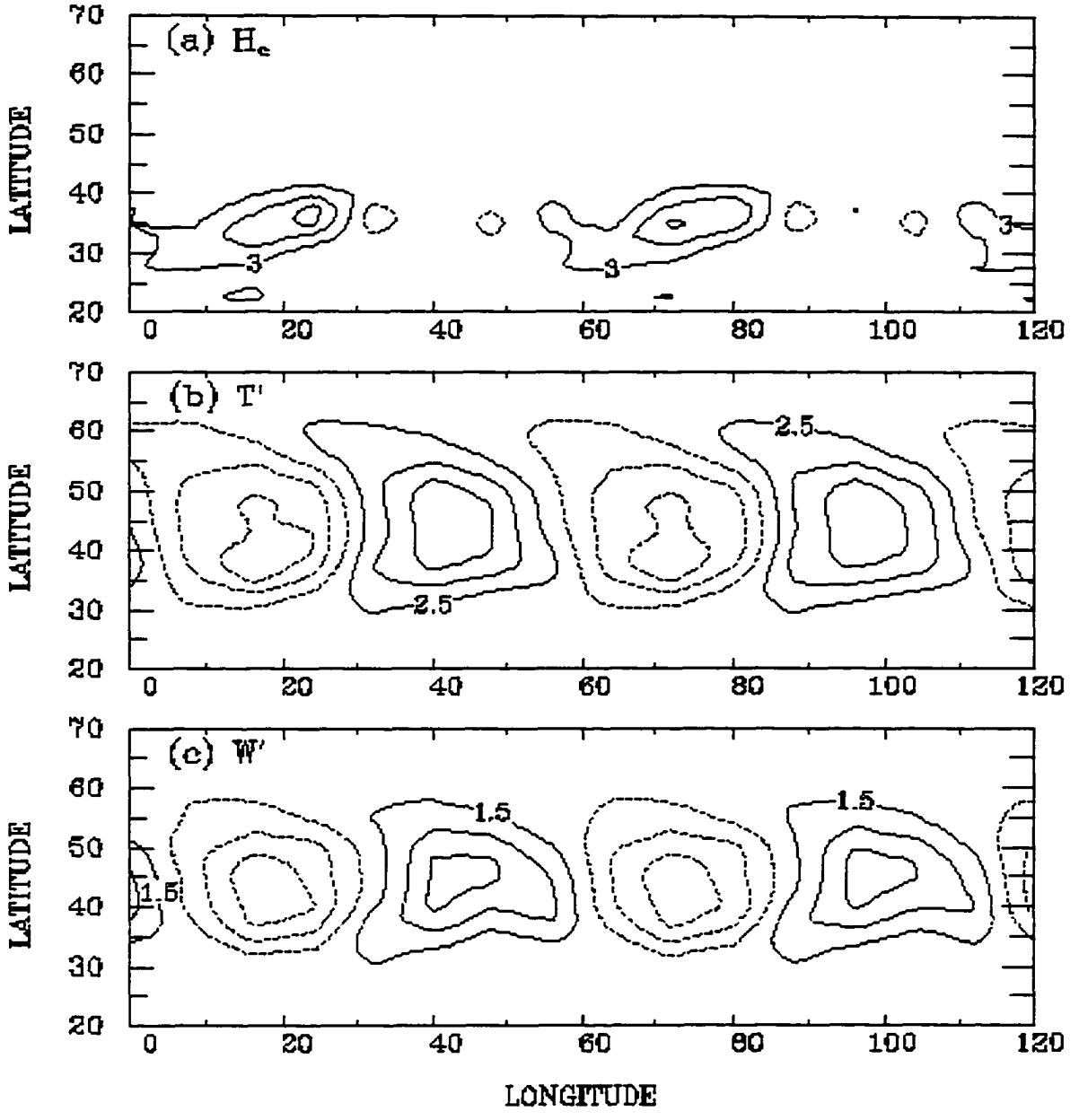

Figure 1.5 Latitude-longitude contours of (a) convective heating [10^{-1} K day^{-1}], (b) eddy temperature [10^{-1} K] and (c) eddy vertical velocity [10^{-4} m s^{-1}] for 960 hPa at the end of day 7, from a wavenumber 7 run including Emanuel convection and surface fluxes. Contour intervals are (a) 0.6 K day^{-1}, (b) 0.5 K, and (c) $3 \bullet 10^{-4}$ m s^{-1}, with dashed contours denoting negative values.

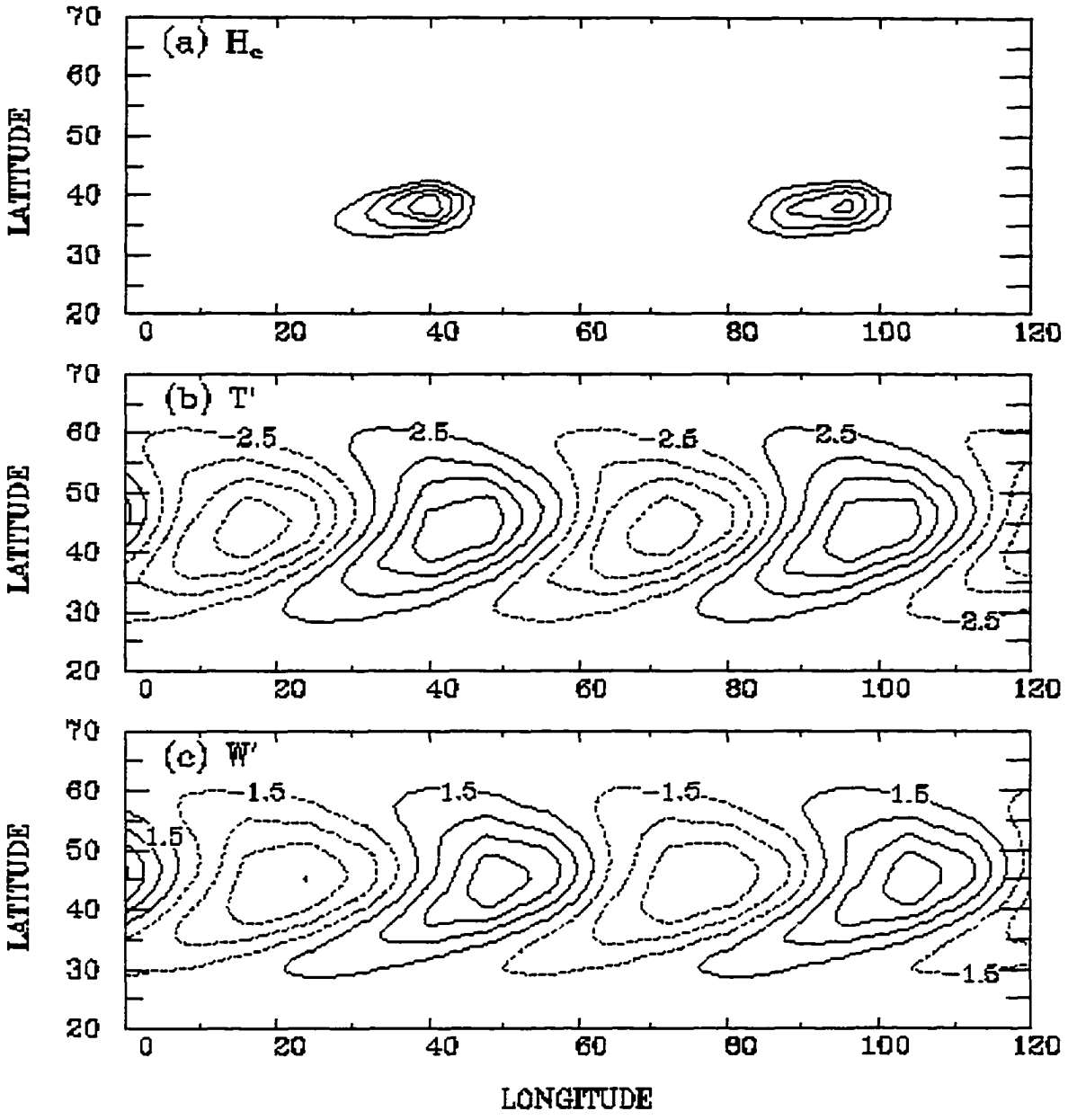

Figure 1.6 Like Fig. 1.5, but with no surface fluxes included. Contour intervals are (a) 0.1 K day^{-1}, (b) 0.5 K and (c) $3 \bullet 10^{-4}$m s^{-1}, with dashed contours denoting negative values.

was used in the previously cited analytical studies. Note that while some of the analytical studies included surface momentum flux (friction), none included surface sensible heat flux, which produces the differences in temperature structure between Figs. 1.3(a) and (b).

The Emanuel scheme requires that there be CAPE present for convection to initiate. In a model with discrete vertical layers, the Emanuel scheme's CAPE for a parcel rising from cloud-base layer (NCB) to the cloud-top layer (NCT) is

$$\text{CAPE} = \sum_{n=NCB}^{NCT} R_d \left(T_{vp}^n - T_v^n \right) \Delta_n \ln p \quad , \qquad (3)$$

where R_d is the gas constant for dry air, T_{vp}^n is the cloud virtual temperature for an air parcel lifted from the lowest model layer to layer n, T_v^n is the environment's virtual temperature in layer n, and $\Delta_n \ln p$ is the change in log(pressure) across layer n. The CAPE thus depends on the difference between the environmental virtual temperature profile and the cloud virtual temperature profile. Figure 1.7 shows time-height contour plots of positive values of $T_{vp}^n - T_v^n$ for one point at latitude 42°N in two wavenumber 7 runs, one with and one without surface fluxes. Consistent with the discussion in Section 3, the location of CAPE development is strongly dependent on whether or not surface fluxes are included in the simulation, with the production of CAPE favored in the cold sector when surface fluxes are present. Also consistent with Fig. 3(a), when surface fluxes are present, the warm sector's layer of positive $T_{vp}^n - T_v^n$ occurs well above the surface. Finally, the figure shows that the cloud-top level tends to be higher when no surface fluxes are present, a feature that one might also infer from Fig. 1.3. We shall see when examining the mature stage of wave development that this difference in cloud-top height is important for how the Emanuel scheme's convection enhances wave growth when surface fluxes are present.

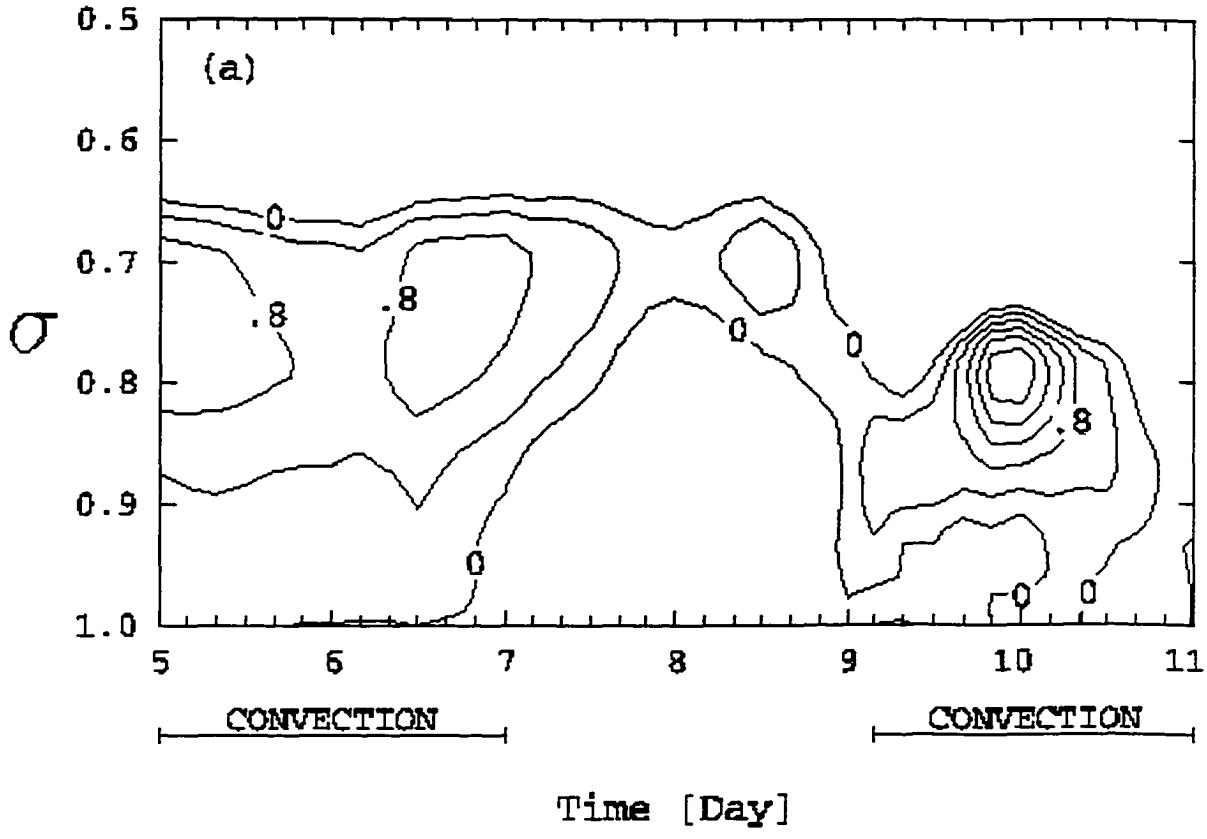

Figure 1.7(a) Time-height contours of positive (T_{vp}-T_v) [K] for a point at 42°N latitude in the wavenumber 7 run that includes surface fluxes. The contour interval is 0.4 K. Horizontal I-bars mark when convection is occurring at this point. Shading marks when the point is in the wave's warm sector.

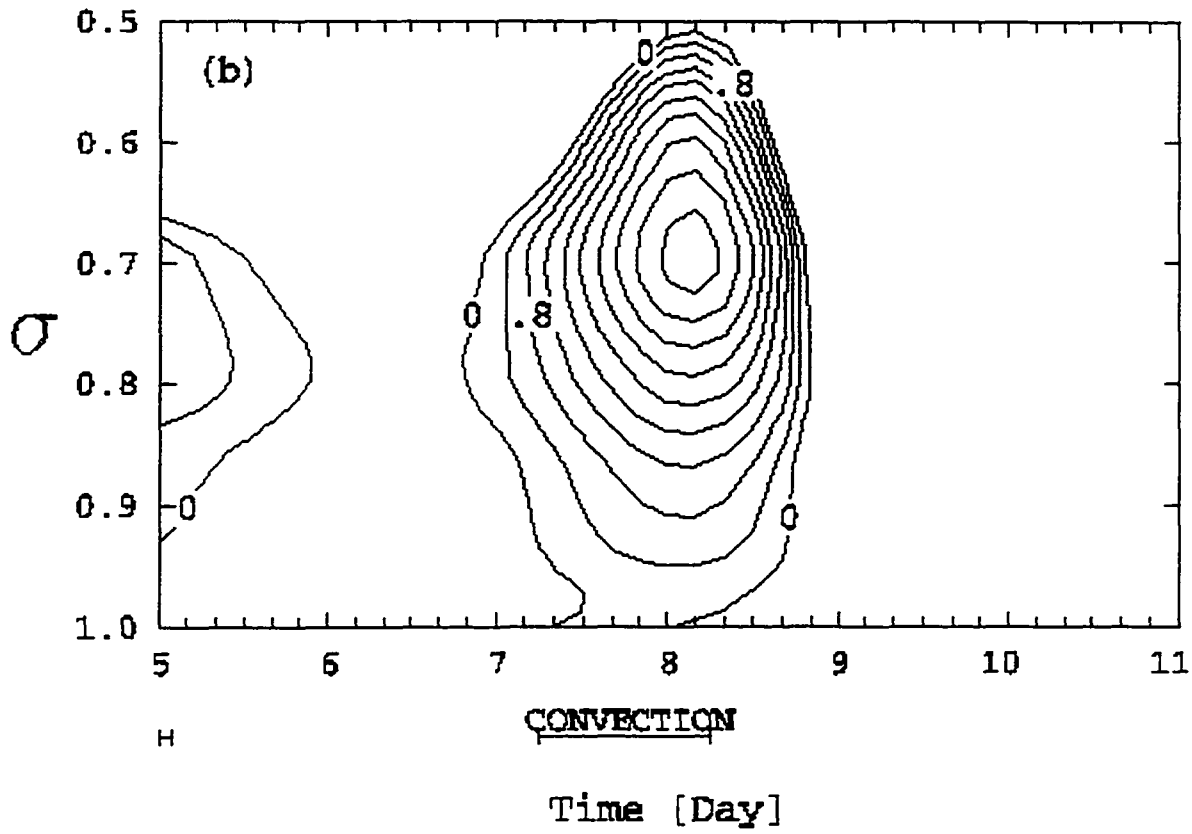

Figure 1.7(b) Same as Fig. 7(a) except the run does not include surface fluxes.

For simulations using either the modified Grell or modified Kuo schemes, the location of convection is also governed by whether or not the simulation includes surface fluxes. As with the Emanuel scheme, when no surface fluxes are present, midlatitude convection using either scheme occurs in the warm sector, whereas when surface fluxes are included convection occurs in the cold sector. For the Grell scheme, the critical factor is the shift of atmospheric destabilization by non-convective processes from the warm sector to the cold sector. The measure of destabilization in the Grell scheme is based on the time change of max(H) - H_{sat} and so is not precisely the same as destabilization determined from the time change of T^n_{vp} -

T_v^n. However, the two differences are similar enough that Fig. 1.7 gives an approximate indication of where the Grell scheme would find atmospheric destabilization, which would tend to occur where $T_{vp}^n - T_v^n$ is increasing with time. (The reader is reminded that Fig. 1.7 includes the effects of convective heating on the temperature profile, and so includes convective stabilization as well as non-convective destabilization.) The shift in the location of destabilization is also important for the Kuo scheme, as is the shift of the unstable boundary layer from the warm to cold sector when surface fluxes are added. Finally, for all three schemes, convection is shallower when surface fluxes are included.

Mature stage

a. Enhanced wave growth

During the mature stage, the wave attains its maximum amplitude before decaying. Figure 1.8 shows the evolution of eddy kinetic energy K_e for the two wave number 7 simulations using the Emanuel scheme with and without surface fluxes. Also shown in Figure 1.8 are the evolution of K_e for two additional runs with and without surface fluxes that used no convection scheme. For the latter two simulations, adding surface fluxes reduces the maximum K_e attained by the wave, which might be expected since surface momentum and sensible heat fluxes suppress the wave's amplitude near the surface (e.g., Branscome et al. 1989). However, for the two runs with convection included, adding surface fluxes increases the maximum K_e by 28%, so convection is somehow enhancing wave growth.

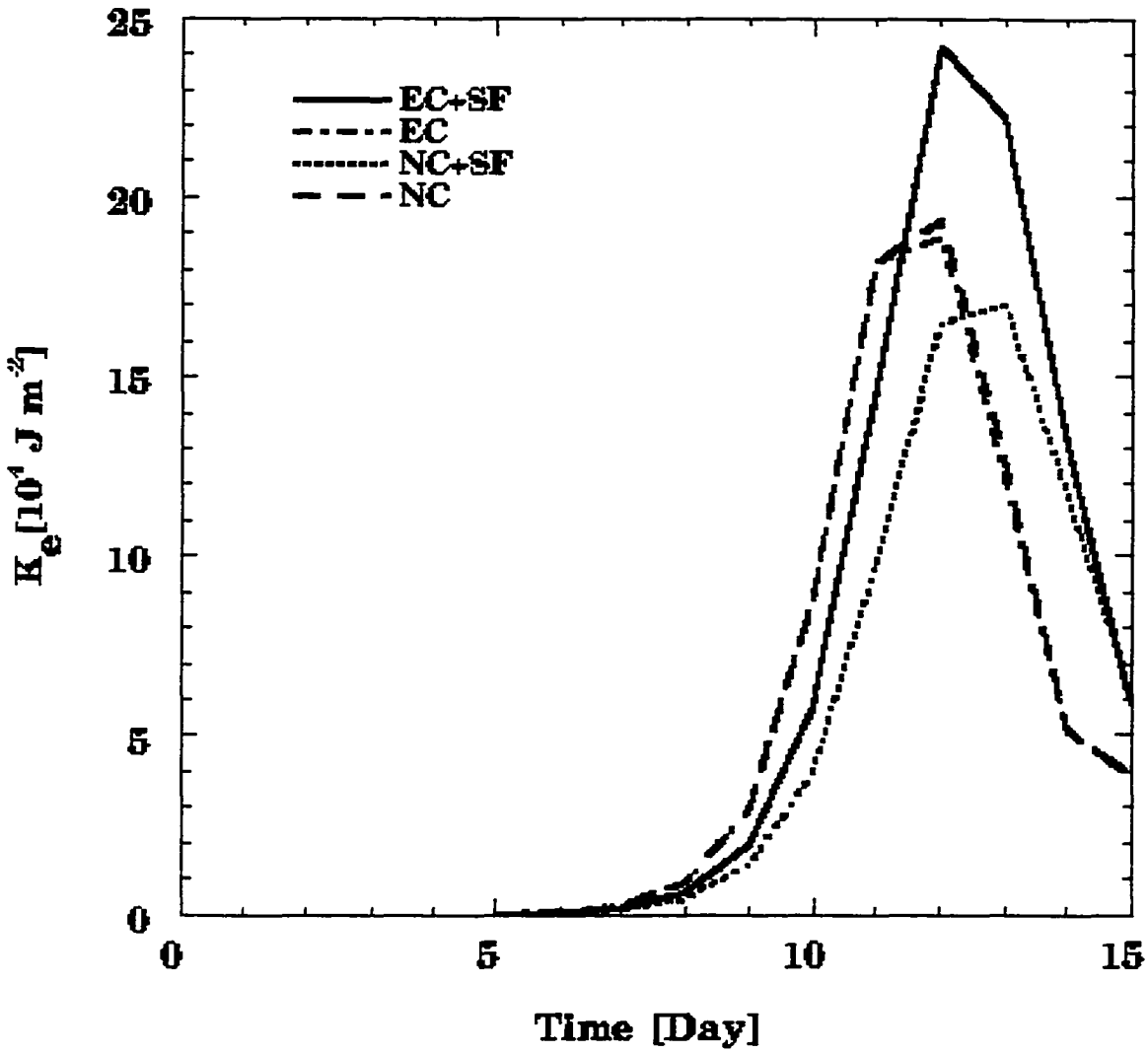

Figure 1.8 K_e vs. time for runs that include Emanuel convection and surface fluxes (EC+SF), Emanuel convection and no surface fluxes (EC), surface fluxes and no convection (NC+SF), and no convection or surface fluxes (NC).

One possibility is that convective heating supplies energy directly to the wave. However, for the two simulations without surface fluxes, maximum K_e hardly depends on whether or not convection is included. In the runs that include convection, the generation of available potential energy by convection, whether in the warm or the cold sector, has an absolute value less than 0.03 W m^{-2} when averaged over days 8 to 14 whereas the conversion of zonal to eddy available potential energy averages more than 0.9 W m^{-2} during the same period. Thus, the direct effect of convective heating on wave development is negligible.

Figure 1.4 shows mid-troposphere cooling by convection, which is occurring in the cold sector. This cooling is caused by downdrafts in the Emanuel scheme and partially balances the mid-tropospheric heating caused by the eddy vertical heat flux. In the warm sector of the wave, heating by large-scale condensation promotes wave growth by catalyzing stronger upward motion and thus a stronger conversion of APE (GBS). Conceivably, the convective cooling in the cold sector could accomplish similar results. We performed additional computations in which this cooling was not applied to the resolved temperature field. The absence of the cooling had negligible effect on the wave's development.

Figure 1.4 shows that the lower tropospheric heating occurs primarily within and just above the model's planetary boundary layer. This location suggests that the cold-sector convection could modify the PBL in a way that enhances wave growth, for example by reducing temperature-wave damping by surface heat fluxes. We examine this possibility by reconsidering the early stage, when the eddy fields have relatively small magnitude, so that we can assume approximately linear dynamics. Then, the eddy potential-temperature field θ' is the sum of two fields

$$\theta' = \theta'_w + \theta'_c \quad , \qquad (4)$$

where θ'_w is the eddy potential temperature due to the growing baroclinic wave and θ'_c is the eddy potential temperature due to accumulated convective heating. We assume that the effect of moisture condensation is to modify the dry instability during the early stage, but not produce a

dramatically different behavior (e.g., GBS), so that θ_c' represents a small addition to θ_w' and the wave speeds during the early stage are not substantially changed by the condensation. The eddy potential temperature tendency during the early stage is then, in Cartesian geometry,

$$\frac{\partial \theta'}{\partial t} = \left\{ -[u]\frac{\partial \theta_w'}{\partial x} - v_w'\frac{\partial [\theta]}{\partial y} - w_w'\frac{\partial [\theta]}{\partial z} \right\} - [u]\frac{\partial \theta_c'}{\partial x} + \frac{[\theta]}{[T]}\dot{H}_c' \qquad (5)$$

where the square braces refer to the zonal-average field, the subscript w refers to baroclinic-wave variables, and $\dot{H}_c'$ is the eddy part of the convective heating. Other new symbols in (5) have their standard meteorological definitions. The term in braces in (5) represents the evolution of the temperature field due to the growing wave. In addition to temperature-wave growth, it also produces a propagation of the θ' wave downstream (toward the east) with a phase speed of roughly 10 m s^{-1} in midlatitudes.

The convective terms distort the temperature wave, with the advection of θ_c' in particular inducing a phase lag that varies with height within the PBL. The distortion is sufficient to further stabilize the PBL over part of the already stable warm sector, where PBL structure is not governed by dry convection. As a consequence, damping of the temperature wave by surface sensible heat flux F_{sh} is reduced. The damping affects wave energetics through the generation of eddy available potential energy, for which F_{sh} alone gives a contribution

$$G_e \propto (F_{sh})'T_s' \ , \qquad (6)$$

where T_s' is the eddy temperature field in the model's lowest layer. The magnitude of this product is substantially reduced in the wave's warm sector when Emanuel convection is included (Fig. 1.9). Integrated across the wave, the sink of eddy available potential energy is 20 - 30% smaller as the wave grows. The quantitative response of G_e to the convective heating and surface flux is likely sensitive to details of the PBL parameterization used here, so

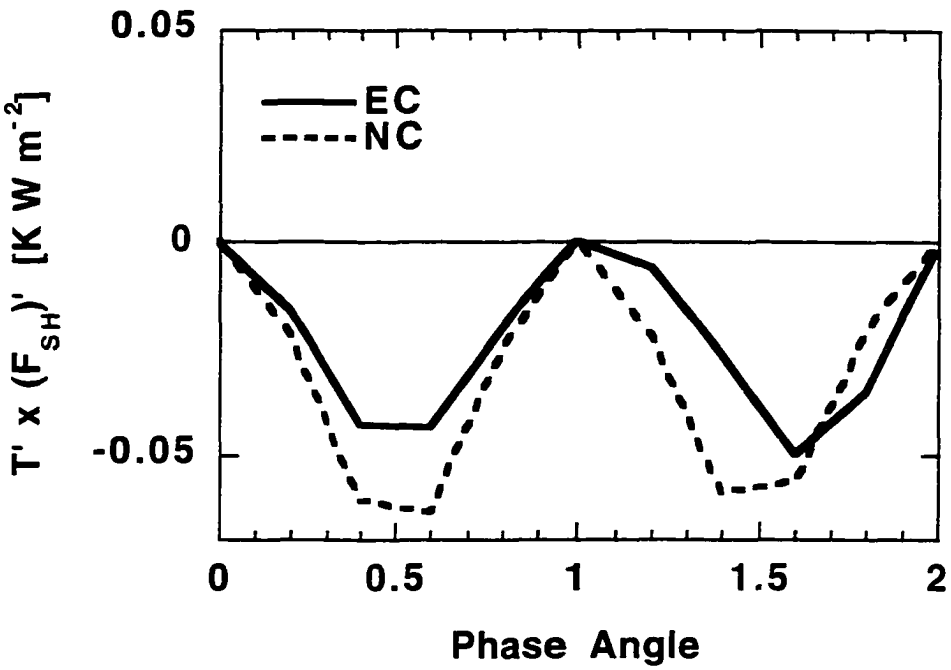

Figure 1.9 The product $(F_{sh})'T'$ in the model's lowest layer as a function of wave phase angle. Results are at 42°N latitude on day 5 for wavenumber 7 runs with surface fluxes that include Emanuel convection (EC) or have no convection (NC). The phase angle is in units of π, and the warm sector occurs for phase angle $\in$ [0, 1].

further examination of this issue is beyond the scope of this study. This process, however, only removes a sink of wave energy due to surface heat flux, and by itself it could at best increase the maximum K_e from $1.7 \cdot 10^5$ J m^{-2} (the no convection case with surface fluxes) to $1.9 \cdot 10^5$ J m^{-2} (the no convection case without this or other surface sinks). An additional source of energy is needed.

A source of additional energy can result from surface evaporation, if the water vapor given to the atmosphere condenses appropriately. All three convective schemes condense some of this water into surface precipitation, even when the convection is relatively shallow, but we have seen that such direct condensational heating by the Emanuel scheme is of negligible importance to wave energetics. However, the Emanuel scheme also transports water vertically from the boundary layer into the lower troposphere (Fig. 1.10). The moistening shown in Fig. 1.10 occurs in the cold sector. If this added water condensed there, it would produce a loss rather than gain of eddy available potential energy.

To determine if and where the water added to the cold sector does condense, we have performed tracer computations using the resolved, three-dimensional wind fields of the simulation. The tracers track the paths of particles released at extratropical gridpoints experiencing convection at the end of days 5, 6, ... 10 in the run using Emanuel convection and surface fluxes. For each gridpoint so chosen, the particle was released at the level with the largest convective moistening rate. We computed particle paths following the method of Kida (1983), except that we used the model-computed winds from every time step (15 min.) of the simulation (see Appendix A for details).

Figure 1.11(a) shows the latitude-longitude paths for particles released at the end of day 7. Recall that Fig. 1.5 shows horizontal distributions of convective heating and eddy temperature on day 7, thus indicating the atmospheric state at release time. Note however that Fig. 1.5 shows fields at 960 hPa, whereas maximum convective moistening, and thus particle

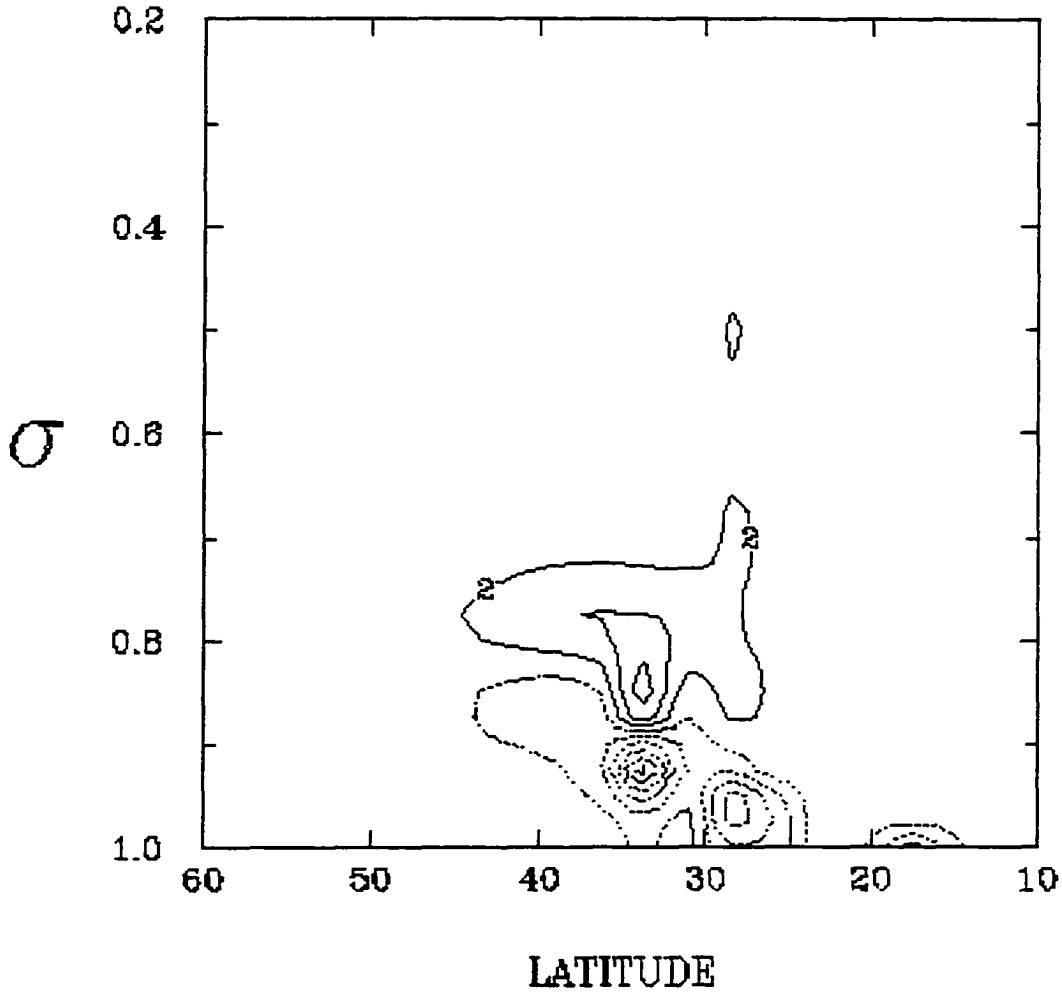

Figure 1.10 Latitude-height cross-section of moistening rate by Emanuel convection during the last hour of day 7 for the wavenumber 7 run that includes surface fluxes. Contour interval is $6 \cdot 10^{-2}$ g kg^{-1} day^{-1}, with dashed contours denoting negative values. Contours less than $-45 \cdot 10^{-2}$ g kg^{-1} day^{-1} are not drawn.

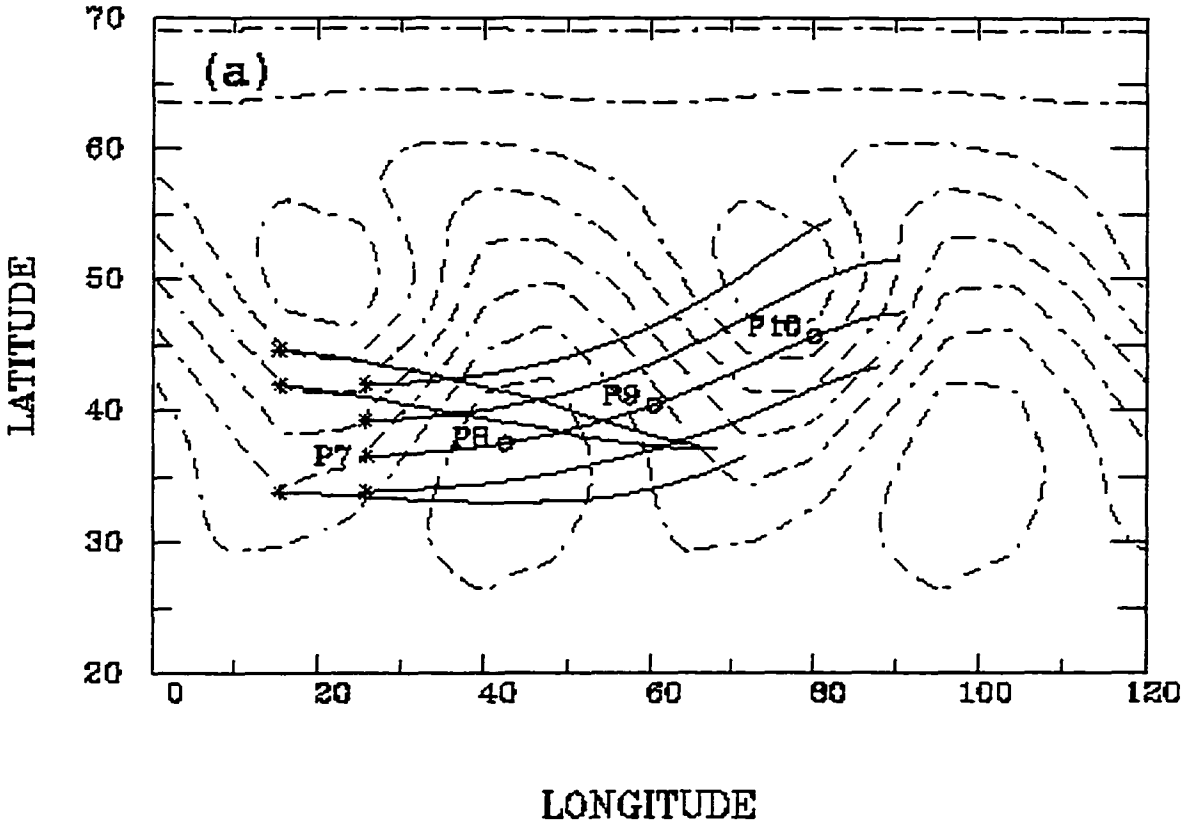

Figure 1.11(a) Latitude-longitude paths of all particles released where the largest convective moistening was occurring at the end of day 7 in the run using Emanuel convection and surface fluxes. The particle location at the end of days 7 - 10 is marked P7,...,P10. Dash-dot lines show contours of surface pressure at the end of day 10 (cf. Fig. 1.1(a) for contour values).

release, occurs near 700 hPa. Figure 1.11(a) also shows contours of surface pressure at the end of day 10 to indicate the synoptic state near the ending time of the trajectories. (Fig. 1.1(a) gives further detail of the synoptic state at this time.) Figure 1.11(b) shows the height-longitude path for a particle originating at a point with one of the largest convective moistening rates. The vertical axis is the model's sigma coordinate. The vertical motion of this particle is representative of its neighbors in Fig. 1.11(a) that also follow a northeastward path. Figure 1.11(b) also shows the LCL for air at the particle's origin, as well as the location of the cold front in the lower atmosphere at the particle's latitude for the times marked. We have defined the cold front here as the boundary between positive and negative eddy temperature at levels where the temperature contrast between the centers of the warm and cold sectors exceeds 5 °C. This boundary is the location of strongest temperature gradient. By this definition, temperature contrasts on day 7 are not strong enough to produce a front, but we have drawn on the figure the boundary dividing warm and cold sectors in the lower atmosphere. The fronts weaken and eventually disappear with height because the amplitude of the eddy temperature field decreases with height [cf. Fig. 7 of Branscome et al. (1989)].

The horizontal trajectories in Fig. 1.11(a) are qualitatively similar to those computed by others for particles released in the lower troposphere upstream from an extratropical cyclone (cf. Kuo et al. 1985; Merrill et al. 1986; Reed et al. 1992). We assume that these trajectories correspond to the paths that water vapor follows from the same starting points. To verify this, we have diagnosed potential and equivalent potential temperatures along the trajectories. Table 1-1 shows these quantities for the trajectory appearing in both Figs. 1.11(a) and (b). The potential and the equivalent potential temperatures are fairly constant (cf. Reed et al. 1992) and exhibit changes much smaller than the spatial variation of these fields across the midlatitudes. The results in Table 1-1 are representative for all the trajectories shown, so we conclude that they do represent paths followed by water vapor from the point where convection injects it into the lower troposphere to where it condenses.

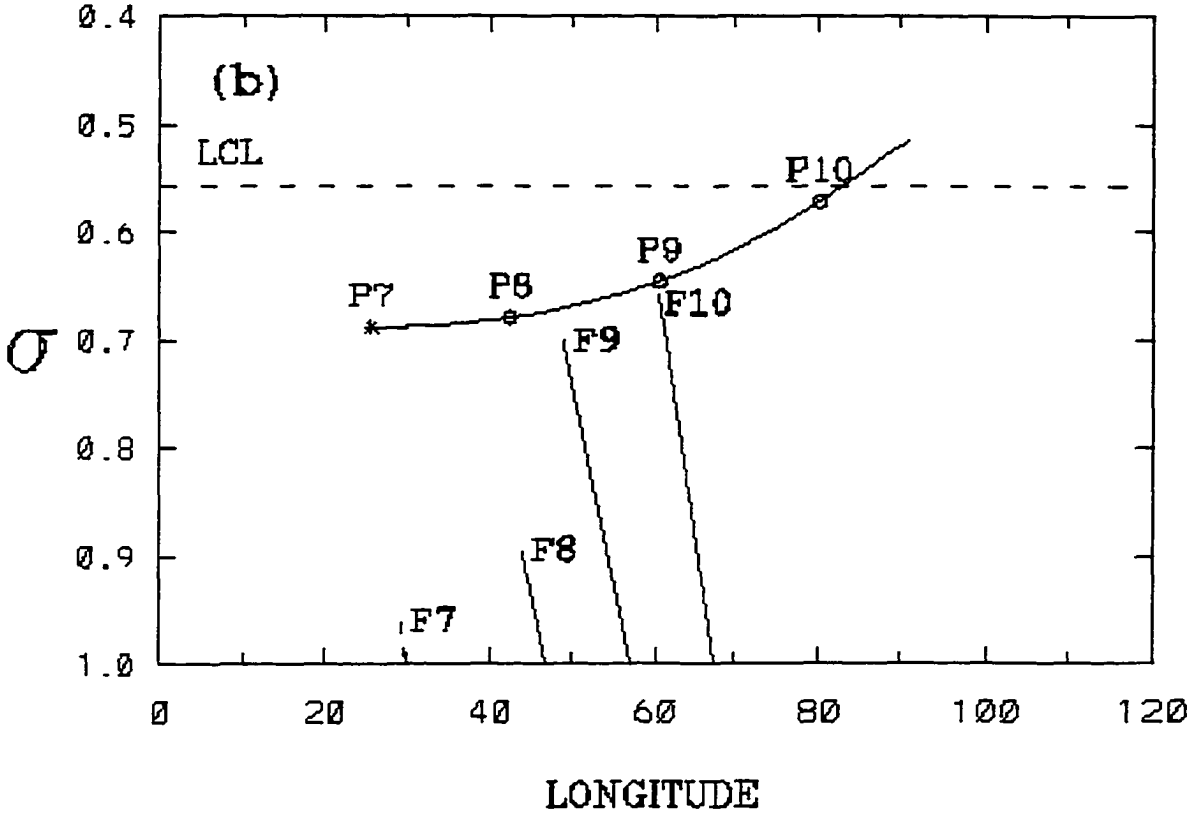

Figure 1.11(b) Latitude-height path for one of the particles shown in Fig. 1.11(a). The dashed line shows the lifting condensation level (LCL) for air parcels at the path's origin and vertical lines mark the location and vertical extent of the cold front at the particle's latitude on days 8, 9 and 10, denoted by F8, F9, F10, and the boundary between the warm and cold sectors on day 7 (dashed line F7).

Table 1-1 Atmospheric properties at the end of days 7 - 10 along the trajectory appearing in both Figs. 1.11(a) and (b). Properties shown are potential temperature (θ), equivalent potential temperature (θ_e), temperature (T), relative humidity (RH) and lifting condensation level (LCL).

Day	θ [K]	θ_e [K]	T [K]	RH [%]	LCL [hPa]
7	296.7	307.1	267.7	34	584
8	296.7	306.5	266.6	37	583
9	297.0	304.7	262.7	47	574
10	297.7	302.1	253.9	75	547

Table 1-1 and Fig. 1.11(b) also show that air moving along this trajectory rises, cools and approaches saturation as it progresses; its water vapor starts condensing during day 11. In addition, its path takes it from the cold sector, over the front and into the warm sector (Fig. 1.11(b)). The overall behavior is representative of moist air parcels following the trajectories parallel to this one in Fig. 1.11(a). Similar trajectories appear in some observational studies of extratropical storms (e.g., Browning and Harrold 1969; Browning et al. 1973; Harrold 1973). Model parcels following trajectories like that in Fig. 1.11(b) experience condensation in the warm sector by large-scale uplift. Parcels following paths originating in layers convectively moistened at the end of days 6 and 8 may also reach their LCL and tend to do so between days 10 and 12, whereas air parcels following paths starting at the end of days 5, 9 and 10 do not reach their LCL while the wave is still growing. Water vapor pumped by the Emanuel scheme into the cold sector's lower troposphere during days 7 through 8 thus condenses later in the

warm sector during the period when the wave is growing toward the largest K_e of the cases depicted in Fig. 1.8. The additional heating increases the generation of available potential energy by large-scale condensation.

The net change in generation, however, is an order of magnitude smaller than changes experienced by the conversion terms in the wave's energy cycle when Emanuel convection is added. A more important effect of the added moisture thus appears to be its impact on the conversion of eddy available to eddy kinetic energy. The added moisture enters the warm sector in a layer roughly coincident with the levels of strongest eddy vertical motion (approximately 500 - 700 hPa, not shown). The importance of the additional moisture at these levels can be seen by considering the conversion of eddy available (A_e) to eddy kinetic energy:

$$C\{A_e,K_e\} = -\int \frac{R_d}{p}[\omega'T']dm \quad , \tag{7}$$

where $[\omega'T']$ is the zonal average, eddy vertical heat flux, dm is the differential mass element for the atmosphere, and the integration occurs over the entire model atmosphere. In GBS, it was shown that the condensational heating caused by large-scale uplift catalyzes a stronger $C\{A_e,K_e\}$ by enhancing the buoyancy of the air and, hence, the vertical eddy heat flux, $[\omega'T']$, appearing in (7). As a consequence, the additional moisture provided by shallow convection amplifies the tendency found in GBS for large-scale supersaturation to catalyze a more energetic life cycle and yield a larger maximum in eddy kinetic energy. The conversion $C\{A_e,K_e\}$ is 30% larger in the run with convection and surface fluxes than in the run with surface fluxes only.

The ability of the Emanuel scheme's convection to amplify the wave's energy cycle rests on the fact that the convection is relatively shallow in simulations with surface fluxes included. The warm-sector convection that occurs when surface fluxes are absent also

moistens part of the atmosphere, but as the wave matures, the moistening in the region 30° - 60°, where the vertical eddy heat flux in (7) is strongest, is two orders of magnitude smaller than the moistening in Fig. 1.10, so the warm-sector convective moistening has little influence on $C\{A_e,K_e\}$. The occurrence of surface evaporation directly below the convection is also important. In a wavenumber 7 run that excluded surface evaporation while retaining convection, surface drag and surface sensible heat flux, the large-scale supersaturation was reduced and $C\{A_e,K_e\}$ was 32% smaller than in the simulation that included surface evaporation.

The modified Grell and Kuo schemes also give relatively shallow convection in the cold sector when surface fluxes are included, but neither scheme prompts the increase in K_e observed when using the Emanuel scheme. The critical difference appears to be the degree of lower-troposphere moistening each scheme produces. Table 1-2 shows the moistening rate by convection for the layer 800 hPa - 500 hPa in midlatitudes from runs using each scheme. The

Table 1-2 Moistening rate by convection averaged over the region 30° - 60° (lat) and 800 - 500 hPa for runs including surface fluxes and using different convection schemes. Rates shown are averages over the last hour of the day indicated.

Convection Scheme	Moistening Rate (10^{-2} g kg^{-1} day^{-1})		
	Day 6	Day 7	Day 8
Emanuel	2.3	2.5	1.2
Grell	0.0	0.1	0.0
Kuo	1.4	- 1.0	- 1.0

moistening rate is given for days 6 - 8, when the Emanuel scheme moistens the lower troposphere with water vapor that later condenses in the warm sector. The reasons for the differences in moistening rate by each convective scheme lie within the details of each convective parameterization and are beyond the scope of this study. However, Table 1-2 and the trajectory discussion above indicate that the key difference between schemes in their ability to enhance eddy kinetic energy is their amount of tropospheric moistening in the cold sector above the PBL.

b. Convection lagging wave development

Net convective heating averaged over latitudes 20°- 70° typically reaches its maximum in the mature stage one or two days after the eddy kinetic energy has passed its maximum. This behavior was also noted in GBS. To understand this lag, we analyze how the potential for instability in the atmosphere evolves over the life cycle, focusing on the Emanuel scheme's convection. To diagnose the potential for convective instability, we have calculated the saturation equivalent potential temperature θ_e, computed as

$$\theta_e = \theta \exp\left\{\frac{Lq_s}{c_p T}\right\} \quad , \qquad (8)$$

where L is the latent heat of vaporization, q_s is the saturation specific humidity, and c_p is the heat capacity of air at constant pressure. An atmospheric column is potentially unstable to convection when θ_e decreases with height somewhere in a statically stable atmospheric column (Emanuel, 1994). This behavior is most likely to occur in the lower atmosphere where the decrease with height of relatively warm temperatures allows θ_s to decrease rapidly enough to override the general increase of θ with height.

We diagnose potential convective instability here by the difference

$$\Delta\theta_e = [\theta_e](850\ \text{hPa}) - [\theta_e](1000\ \text{hPa}) \quad . \quad (9)$$

Figure 1.12 shows $\Delta\theta_e$ as a function of latitude for selected times during the wavenumber 7 run using the Emanuel scheme. During the mature stage, static stability in midlatitudes increases, a behavior occurring as part of the baroclinic adjustment process (Stone, 1978; Gutowski et al. 1989). Midlatitude convection is thus suppressed simply because the overall stability of the atmosphere increases at these latitudes. More important, however, is the decrease in convective stability that is induced by the wave dynamics in the neighborhood of 30° latitude, especially between days 11 and 13. Despite the strong destabilization being produced by the eddy dynamics, the convective maximum does not occur during this period but later, as the eddy dynamics weaken.

Convection requires sufficient moisture to occur in addition to potential instability. We can investigate moisture change during the life cycle through the distribution of vertically integrated specific humidity. Figure 1.13 gives the change in atmospheric humidity from day 0 to selected days in the wavenumber 7 simulation. The eddy moisture flux (e.g. Fig. 12 of GBS) draws moisture from the subtropics and transports it poleward as the wave grows. As a result, atmospheric moisture increases in the region 40° - 60° but decreases between roughly 30° - 40° as the wave grows. Latitudinal moisture transport to support subtropical convection is thus lacking as the wave grows to maximum amplitude. Moisture is deposited where the atmosphere is stabilized in midlatitudes and is depleted or increases very little where destabilization occurs. Lowered moisture in the subtropics produces a higher LCL, making convection less likely (cf. Fig. 1.3). Thus, the net effect of the wave dynamics in both the subtropics and midlatitudes during the period of wave growth is a suppression of convection relative to its strength as the wave weakens.

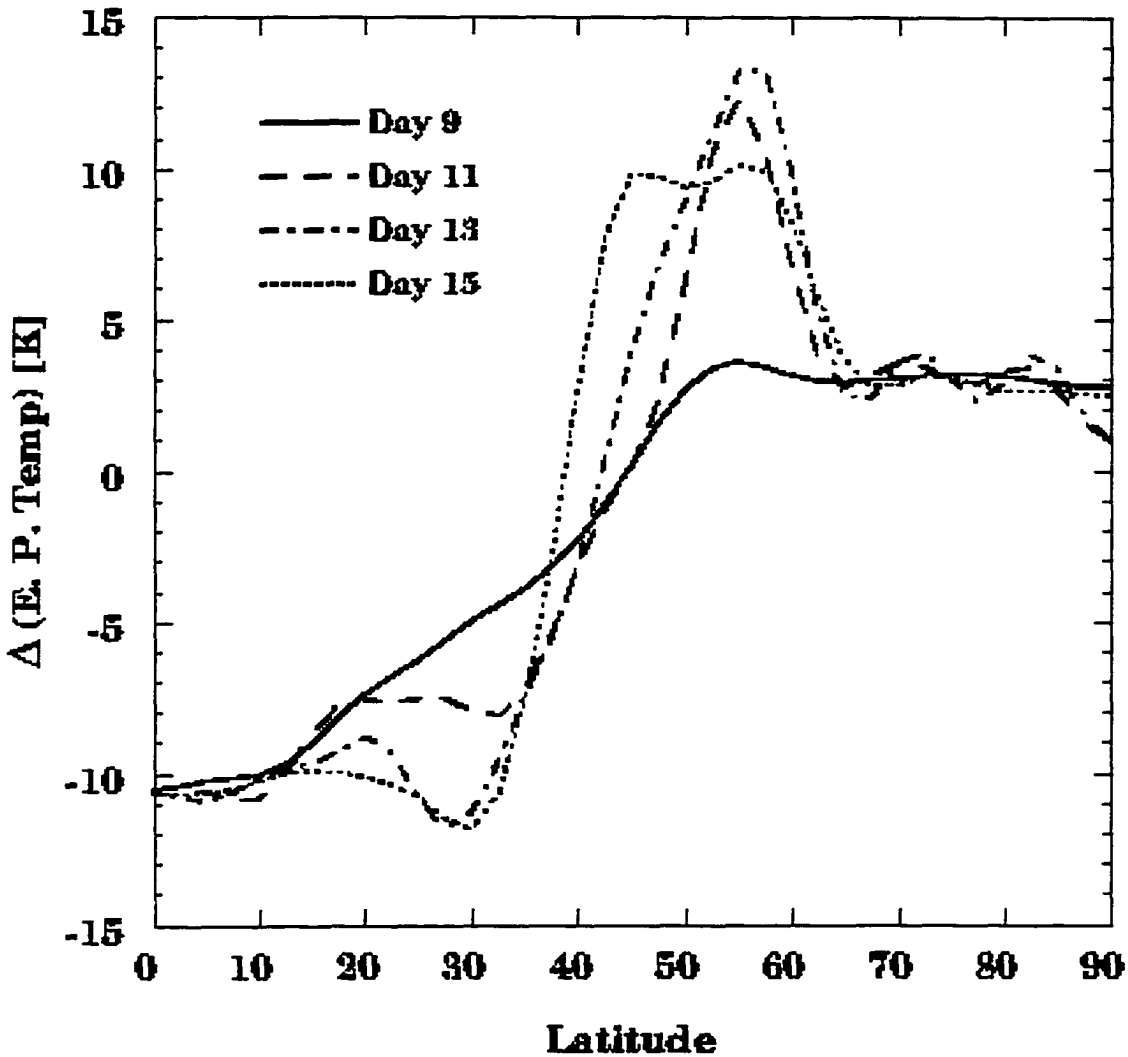

Figure 1.12 $\Delta\theta_e$ vs. latitude for selected times in the wavenumber 7 run using Emanuel convection.

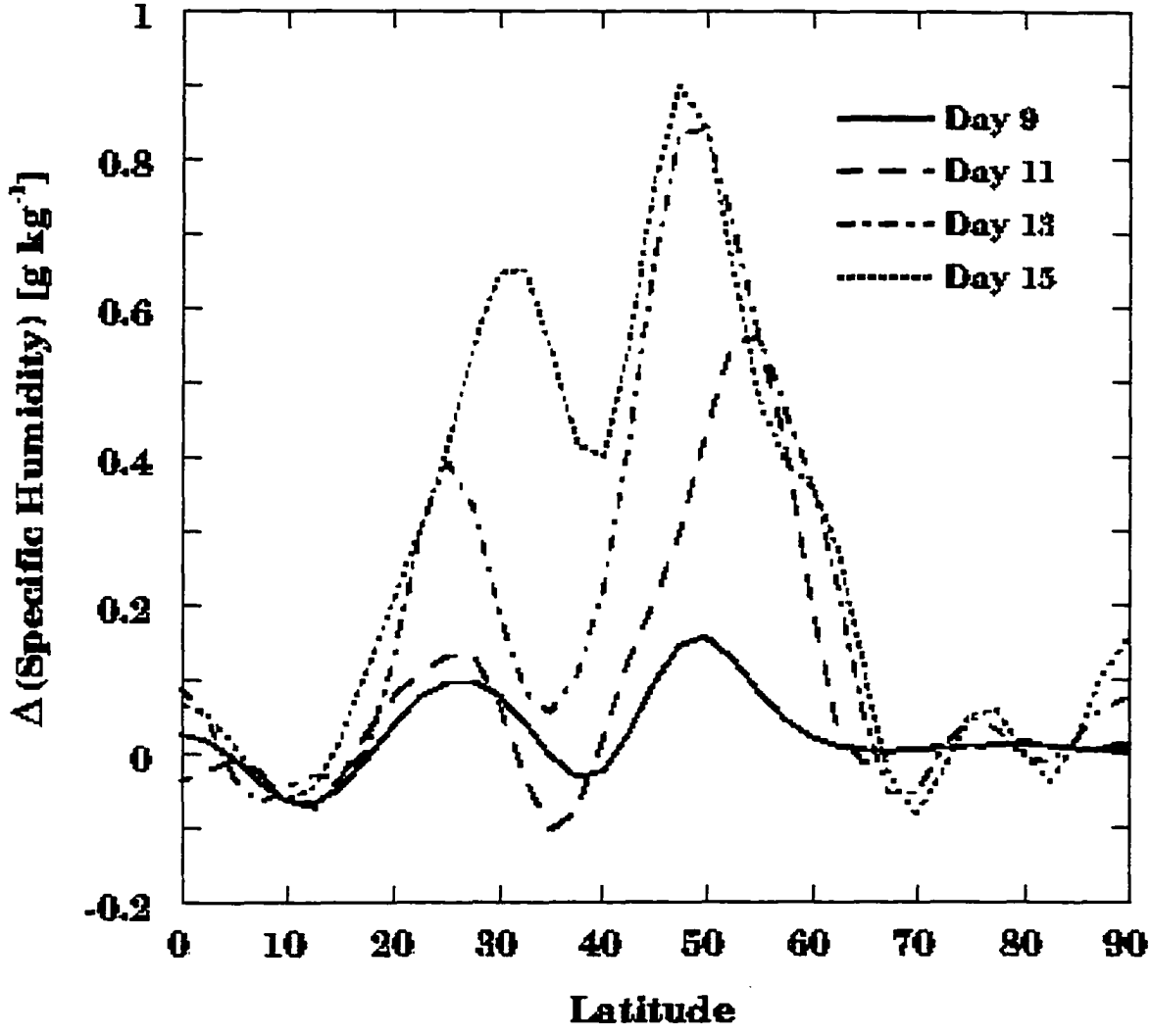

Figure 1.13 Like Fig. 1.12, but for the change from the initial state in zonal and vertical average specific humidity.

Surface evaporation in the subtropics can counteract the depletion by eddy dynamics, but up through day 11 it is insufficient to prevent a reduction in atmospheric humidity near 30°. As the wave decays, however, its horizontal moisture flux decreases rapidly and surface evaporation near 30° not only restores lost humidity but also helps increase it well beyond its initial amount. The increased humidity lowers the lifting condensation level and allows convection to reach its largest total magnitude while the wave decays.

Summary and discussion

We have examined the role of convection in the dynamics of the eddy life cycle through numerical experiments using an ocean-covered lower boundary with zonally symmetric temperature distribution. The initial and boundary conditions are based on Southern Hemisphere climatology, except that initial specific humidity was modified from climatology to allow midlatitude conditional instability. As in GBS, we focus on transient eddy processes contributing to global-scale circulation and climate. The behavior of life cycles for wavenumber 7 has been emphasized in our work because it is the most unstable wave and it attains the largest amplitude, thus producing the strongest eddy fluxes of heat, moisture, and momentum in the extratropical atmosphere. Other wave scales may contribute to transient eddy transports and modification of the zonal mean state, so we also performed experiments using wavenumber 6, 12, or 15 as the fundamental wave in order to cover a range of wavenumbers. Our results obtained here apply qualitatively to both winter and summer simulations and to all wavenumbers studied except that the amplification of K_e that occurs when using the Emanuel scheme is much stronger for wavenumber 7 than for other wavenumbers.

The growth of the unstable wave prompts the appearance of midlatitude convection. However, there are substantial differences in the character of convection between simulations with and without surface fluxes included. These differences are tied to how the wave's near-

surface temperatures evolve under the influence of the growing wave and, when included, surface sensible heat flux, with the location of moist-convective destabilization being strongly dependent on the influence of both processes as outlined schematically in Fig. 1.3. As a consequence, for all three convective schemes used here (Emanuel, modified Grell, modified Kuo), convection is favored in the warm sector when there are no surface fluxes included in the simulation and in the cold sector when there are. Each scheme's convection is also shallower (though still precipitating) when it occurs in the cold sector rather than the warm sector, with convective heating and moistening confined to the lower troposphere.

The shallowness of the cold-sector convection, however, is important for enhanced wave growth induced by the Emanuel scheme when surface fluxes are present. The relatively shallow convection plays a central role in a water cycle wherein (1) evaporation gives moisture to the cold sector's boundary layer, (2) convection pumps some of the moisture into the lower troposphere above the boundary layer, (3) the large-scale circulation transports the moisture eastward and upward into the wave's warm sector, and (4) stable condensation precipitates the moisture out of the atmosphere. The added moisture enhances a process described in GBS wherein heating by supersaturation in the lower to middle troposphere catalyzes a more energetic life cycle by inducing greater conversion of available potential energy to kinetic energy. The enhancement observed here is parameterization-dependent, and the key factor appears to be how much lower tropospheric moistening each scheme produces. The modified Grell and Kuo schemes give much less lower-tropospheric moistening, so they do not promote greater wave growth like the Emanuel scheme does. These simulations are of course for an idealized environment, as indicated by the two-day episodes of continuous convection experience by the midlatitude point in Fig. 1.7. We are examining more complex environments using a variety of convection schemes to discern whether or not this water cycle does indeed contribute to the development of observed, marine storms.

These simulations have also been performed at relatively low resolution, especially in the zonal direction. However, as noted, the behavior of particle paths traced here appear to be realistic in comparison with observations. Additional paths (not shown) that originate lower in the cold sector's troposphere also show realistic behavior, moving southeastward and toward the surface and then veering to the southwest near the surface cold front. For the spectral truncation used, the model may not resolve well the vertical extent of the cold front (Fig. 1.11(b)), so the model's flow may allow more air to reach the warm sector than is typical. In addition, the model's truncated spectral representation potentially could smear fields such as convective moistening, producing an effective moisture transport across the cold front that has no physical basis. However, an examination of transformed convective moistening (not shown) shows that any such non-physical transport across the front is very small.

The location of convection in our computations is consistent with the assumed location in the analytic studies listed in the Introduction. In those studies, convection is assumed to occur where the vertical velocity in the lower atmosphere is upward. This behavior also occurs for each of the convection schemes used here when there are no surface fluxes included in the simulation (Fig. 1.6). The common factor among all the analytic and numerical computations is that none include surface sensible heat flux. When surface fluxes are included, their influence on convective destabilization leads to convection occurring where the wave's vertical velocity in the lower atmosphere is downward (Fig. 1.5). Thus, surface-atmosphere coupling by sensible heat flux may be more important for inducing convection than the wave's large-scale vertical motion field when there is a strong heat-flux coupling between the surface and the atmosphere. This suggests an alternative linear instability analysis in which large-scale destabilization for convection is tied to the coupled influence of the wave and surface fluxes on near-surface temperature. Exploring this approach for linking convection to baroclinic wave instability will be the topic of the second paper of this study.

Acknowledgments

Many thanks go to the Air Force Phillips Laboratory and Atmospheric and Environmental Research, Inc., for providing the PL/GD-AER global spectral model with PBL updates that was used for these computations. Thanks also go to K. Emanuel for making available his convection code and L. Branscome, D. Stewart, T.-C. Chen, J. Stanford, C. Snyder and anonymous reviewers for helpful comments in the course of completing this work. This research was supported by NSF grants ATM-913522 and ATM-9616811 to Iowa State University and by an Iowa State Office of the Provost Global-Change Assistantship.

References

Balasubramanian, G., and M. K. Yau, 1994: Baroclinic instability in a two-layer model with parameterized slantwise convection. *J. Atmos. Sci.*, **51,** 971-990.

Bannon, P. R., 1986: Linear development of quasi-geostrophic baroclinic disturbances with condensational heating. *J. Atmos. Sci.*, **43,** 2261-2274.

Branscome, L. E., W. J. Gutowski and D. A. Stewart, 1989: Effect of surface fluxes on the nonlinear development of baroclinic waves. *J. Atmos. Sci.*, **46,** 460-475.

Browning, K. A., M. E. Hardman, T. W. Harrold and C. W. Pardoe, 1973: The structure of rainbands within a mid-latitude depression. *Quart. J. Roy. Meteor. Soc.*, **99,** 215-231.

Browning, K. A., and T. W. Harrold, 1969: Air motion and precipitation growth in a wave depression. *Quart. J. Roy. Meteor. Soc.*, **95,** 288-309.

Card, P. A., and A. Barcilon, 1982: The Charney stability problem with a lower Ekman layer. *J. Atmos. Sci.*, **39,** 2128-2137.

Chang, S. W., T. R. Holt and K. D. Sashegyi, 1996: A numerical study of the ERICA IOP4 marine cyclone. *Mon. Wea. Rev.*, **124,** 27-46.

Charney, J. G., and A. Eliassen, 1964: On the growth of the hurricane depression. *J. Atmos. Sci.*, **21,** 68-75.

Emanuel, K. A., M. Fantini and A. J. Thorpe, 1987: Baroclinic instability in an environment of small stability to slantwise moist convection. Part I: Two-dimensional models. *J. Atmos. Sci.*, **44,** 1559-1573.

Emanuel, K. A., 1991: A scheme for representing cumulus convection in large-scale models. *J. Atmos. Sci.*, **48,** 2313-2335.

Emanuel, K. A., 1994: *Atmospheric Convection.* Oxford University Press, 580 pp.

Green, J. S. A., 1960: A problem in baroclinic instability. *Quart. J. Roy. Meteor. Soc.*, **86,** 237-251.

Fantini, M., 1990: Nongeostrophic corrections to the eigensolutions of a moist baroclinic instability problem. *J. Atmos. Sci.*, **47,** 1277-1287.

Grell, G. A., Y.-H. Kuo and R. J. Pasch, 1991: Semiprognostic tests of cumulus parameterization schemes in the middle latitudes. *Mon. Wea. Rev.*, **119,** 5-31.

Grell, G. A., 1993: Prognostic evaluation of assumptions used by cumulus parameterizations. *Mon. Wea. Rev.*, **121,** 764-787.

Gutowski, W. J., L. E. Branscome and D. A. Stewart, 1989: Mean flow adjustment during life cycles of baroclinic waves. *J. Atmos. Sci.*, **46,** 1724-1737.

Gutowski, W. J., L. E. Branscome and D. A. Stewart, 1992: Life cycles of moist baroclinic eddies. *J. Atmos. Sci.*, **49,** 306-319.

Gyakum, J. R., 1983a: On the evolution of the QE II storm, I: Synoptic aspects. *Mon. Wea. Rev.*, **111,** 1137-1155.

Gyakum, J. R., 1983b: On the evolution of the QE II storm, II: Dynamic and thermodynamic structure. *Mon. Wea. Rev.*, **111,** 1156-1173.

Harrold, T. W., 1973: Mechanisms influencing the distribution of precipitation within baroclinic disturbances. *Quart. J. Roy. Meteor. Soc.*, **99,** 232-251.

Holton, J. R., 1992: *An Introduction to Dynamic Meteorology.* Academic Press, 511 pp.

Jiang, W., 1994: The role of convection in eddy life cycles. M.S. Thesis, Iowa State University, 86 pp.

Kida, H., 1983: General circulation of air parcels and transport characteristics derived from a hemispheric GCM. Part 1. A determination of advective mass flow in the lower stratosphere. *J. Meteor. Soc. Japan,* **61,** 171-187.

Kuo, H. L., 1974: Further studies of the parameterization of the influence of cumulus convection on large-scale flow. *J. Atmos. Sci.*, **31,** 1232-1240.

Kuo, Y.-H., M. Skumanich, P. L. Haagenson and J. Chang, 1985: The accuracy of trajectory models as revealed by observing system simulation experiments. *Mon. Wea. Rev.*, **113,** 1852-1867.

Kuo, Y.-H., and S. Low-Nam, 1990: Prediction of nine explosive cyclones over the Western Atlantic Ocean with a regional model. *Mon. Wea. Rev.*, **118,** 3-25.

Kuo, Y.-H., M. A. Shapiro and E. G. Donall, 1991: The interaction between baroclinic and diabatic processes in a numerical simulations of a rapidly intensifying extratropical marine cyclone. *Mon. Wea. Rev.*, **119,** 368-284.

Mak, M., 1982: On moist quasi-geostrophic baroclinic instability. *J. Atmos. Sci.*, **39,** 2028-2037.

Mak, M., 1983: On moist quasi-geostrophic baroclinic instability in a general model. *Sci. Sin.*, **B26,** 850-864.

Mak, M., 1994: Cyclogenesis in a conditionally unstable moist baroclinic atmosphere. *Tellus,* **46A,** 14-33.

Merrill, J. T., R. Bleck and D. Boudra, 1986: Techniques of Lagrangian trajectory analysis in isentropic coordinates. *Mon. Wea. Rev.*, **114,** 571-581.

Moorthi, S., and A. Arakawa, 1985: Baroclinic instability with cumulus heating. *J. Atmos. Sci.*, **42,** 2007-2031.

Ooyama, K., 1964: A dynamical model for the study of tropical cyclone development. *Geofis. Intern.*, **4,** 187-198.

Reed, R. J., M. T. Stoelinga and Y.-H. Kuo, 1992: A model-aided study of the origin and evolution of the anomalously high potential vorticity in the inner region of a rapidly deepening marine cyclone. *Mon. Wea. Rev.*, **120,** 893-913.

Smith, P. J., P. M. Dare and S. Lin, 1984: The impact of latent heat release on synoptic-scale vertical motions and the development of an extratropical cyclone system. *Mon. Wea. Rev.*, **112,** 2421-2430.

Stone, P. H., 1978: Baroclinic adjustment. *J. Atmos. Sci.*, **35,** 561-571.

Tokioka, T., 1973: A stability study of medium-scale disturbances with inclusion of convective effects. *J. Meteor. Soc. Jpn.*, **51,** 1-10.

Tracton, M. S., 1973: The role of cumulus convection in the development of extratropical cyclones. *Mon. Wea. Rev.*, **101,** 573-593.

Troen, I., and L. Mahrt, 1986: A simple model of the atmospheric boundary layer: Sensitivity to surface evaporation. *Boundary-Layer Meteor.*, **37,** 129-148.

Wang, B., and A. Barcilon, 1986: Moist stability of a baroclinic zonal flow with conditionally unstable stratification. *J. Atmos. Sci.*, **43,** 705-719.

Yau, M. K., and M. Jean, 1989: Synoptic aspects and physical processes in the rapidly intensifying cyclone of 6-8 March 1986. *Atmos.-Ocean,* **27,** 59-86.

THE COUPLING BETWEEN CUMULUS CONVECTION AND BAROCLINIC WAVES: INSTABILITY STUDY

A paper in preparation for publication in the Journal of the Atmospheric Sciences

Weidong Jiang and William J. Gutowski, Jr.

Introduction

Large-scale atmospheric eddies can be satisfactorily explained by baroclinic instability theory which was elegantly presented in analytical studies by Charney (1947) and Eady (1949). Since observational and numerical studies showed the importance of latent heat released by condensation, many studies have been done to incorporate convective heating into dry baroclinic instability theory by relating the convective heating to the low-level vertical motion, since wave-CISK mechanism may also be important for extratropical eddies (e.g., Rasmussen, 1979).

In Tokioka (1973), which coupled cumulus activity with disturbances through low-level convergence, a simple dry baroclinic model on an f-plane with Boussinesq approximation was used to examine the behavior of convective heating during the evolution of disturbances. The heating rate and the vertical flux divergence of momentum due to convective motions were parameterized as the functions of height and the vertical velocity at the top of the Ekman boundary layer. A vertical profile was assumed as such that convective heating occurred between 900m to 5,000m, with maximum heating between 3,000m and 4,500m. The study indicated that convective heating has more impact on wave development than momentum exchange due to convective motions in the wavelength range

studied (1,000-2,000 km). Convective effects shifted the preferred scale for maximum growth to smaller scales and the growth rate increased.

Because of its mathematical simplicity, many researchers have chosen the Eady model to study moist baroclinic instability with cumulus heating. Instead of directly relating the convective heating to the low-level vertical velocity driven by the latent heat release, Mak (1982) expressed convective heating in terms of the low-level vertical velocity of large-scale quasi-geostrophic motions. More or less similar to Tokioka (1973), the vertical heating profile was assumed to have a simple top-hat shape, which makes it possible to get the four analytical solutions. The solutions showed some similar instability characteristics as Tokioka (1973), that is, the most unstable wave's growth rate and its phase speed increase as a specified heating intensity parameter is increased, while the wavelength of the most unstable wave decreases significantly. In contrast to Tokioka's results, both the increase of growth rate and the decrease of the wavelength of the most unstable wave were bounded, which was considered to be a consequence of the heating parameterization different from the wave-CISK scheme. Mak (1994) explained the four discrete eigenmodes from the potential vorticity (PV) point of view. The formulation using a general heating profile was also presented in Mak (1994).

The Eady model was also used by Wang and Barcilon (1986) in which a simplified Kuo convection scheme of parameterization was incorporated in the presence of Ekman pumping. The Kuo scheme was simplified by empirically specifying the vertical heating profile, and the heating coefficient was directly related to the specific humidity in a lower moist layer. They found that convective heating appreciably destabilizes relatively short waves but waves longer than the Rossby radius of deformation are not significantly affected. Their results showed that the growth rate and wavelength of the most unstable wave are nonlinear functions of averaged specific humidity in the moist layer. In the absence of Ekman pumping, they found that, using the traditional wave-CISK treatment,

the growth rate and wavelength of the most unstable wave were still bounded. This was supported by Bannon (1986) in which condensational heating was incorporated into the Eady model as an initial value problem. Using a wave-CISK formulation with a uniform heating profile in the vertical, Bannon found similarly that the growth rate and wavenumbers were bounded. Also, the growth rate and wavenumber of the most unstable mode and the wavenumber of the short-wave cutoff all increased as the heating became larger.

More complicated than the Eady model, the Charney model includes the β–effect, i.e., the variation of the Coriolis effect with latitude. Using the Charney model, Mak (1983) studied baroclinic instability in the presence of condensational heating as well as the β–effect. His results were consistent with the earlier studies, thus showing that the fundamental characteristics of the baroclinic waves on the β–plane were the same as those on the f-plane.

There are some other analytical studies exploring the potential effect of convection on baroclinic instability, e.g., Moorthi and Arakawa (1985), Emanuel et al. (1987), Fantini (1990), and Balasubramanian and Yau (1994). Although there exist some differences among these studies, (for example, Moorthi and Arakawa (1985) examined moist baroclinic instability in the easterly flow), these studies confirm the result that convection tends to increase growth rates of the most unstable waves and shift the wavelength of maximum instability toward shorter waves. It is commonly assumed in most of these analytical studies that the low-level convergence organizes the location and horizontal extent of convection, and the degree of low-level convergence in these studies is measured by the large-scale, low-level vertical motion generated by the wave, either by itself or in conjunction with Ekman pumping. In the studies on slantwise convection by Emanuel et al. (1987) and Fantini (1990), this assumption was modified slightly to a requirement that

at each level in the atmosphere, the location of the wave's upward motion determines where moist convective effects modify the large-scale flow.

From the numerical experiment presented in the first paper, wave-induced cumulus convection is more likely to occur where the unstable boundary layer induced by the wave creates favorable conditions. Based on the numerical result, in this study, the convective heating rate is assumed to be proportional to either (1) eddy meridional velocity or (2) eddy temperature approximately at the top of the wave-induced unstable boundary layer. The assumption is based on the following consideration. When there is interaction between the atmosphere and an ocean-like surface (with high heat capacity), strong surface sensible heat flux is induced due to air flowing over relatively warm surface so that the wave-induced unstable boundary layer usually occurs in the wave's cold sector (with southward wind and negative eddy temperature), which is often observed in cyclones over the ocean. For simplicity the Eady model instead of the Charney model is used since the absence of beta effect does not change the fundamental features of instability (Mak, 1983).

Model formulation

1. Basic equations

Wang and Barcilon (1986) and Mak (1994) studied the simplest meaningful model for moist cyclogenesis, which was a two-dimensional Eady model with a surface layer of moisture allowing for self-induced condensational heating by the disturbance itself. For a linear, y-independent, quasi-geostrophic perturbation about a zonally averaged basic state $U = u(p)$, the governing equations are the vorticity equation and the thermodynamic equation incorporating the geostrophic and hydrostatic balances, which in pressure coordinates are

$$\left(\frac{\partial}{\partial t}+U\frac{\partial}{\partial x}\right)\frac{\partial^2\psi}{\partial x^2}=f_0\frac{\partial\omega}{\partial p} \tag{1}$$

$$\left(\frac{\partial}{\partial t}+U\frac{\partial}{\partial x}\right)\frac{\partial\psi}{\partial p}+\lambda\frac{\partial\psi}{\partial x}+\frac{\sigma}{f_0}\omega=-\frac{RQ}{f_0 p} \tag{2}$$

where

$$\sigma\equiv-\alpha\frac{\partial\ln\theta}{\partial p}=-\frac{R}{P}\left(\frac{\partial T_0}{\partial p}-\frac{RT_0}{C_p p}\right)=\sigma(p)$$

is basic static stability ($m^2s^{-2}mb^{-2}$), α is the specific volume and θ is potential temperature. The term λ represents the vertical wind shear, R is the gas constant, C_p specific heat at constant pressure, and T_0 is horizontal domain average background temperature. The last term on the right-hand side of (2) represents diabatic heating and Q is the diabatic heating rate (Ks^{-1}). In the Eady model, static stability σ and vertical wind shear λ are constant, so,

$$U=\lambda(P_0-p) \tag{3}$$

where P_0 is a reference pressure and

$$dU/dp=-\lambda.$$

The model domain is

$$0\le x<\infty,\qquad p_U\le p\le p_L$$

where p_U and p_L represent the pressure values at the top and bottom boundaries of the model atmosphere.

Assume that the horizontal distance, velocity, time, and pressure respectively have characteristic scales L, V, LV^{-1}, P_0. The following nondimensional quantities will be used in the nondimensional equations and later analysis:

$$x' = \frac{x}{L}, \qquad t' = \frac{Vt}{L}, \qquad p' = \frac{p}{P_0},$$

$$\psi' = \frac{\psi}{LV} \qquad \omega' = \frac{\omega L^2 f_0}{V^2 P_0}, \qquad U' = \frac{U}{V},$$

$$\sigma' = \sigma\left(\frac{P_0}{f_0 L}\right)^2 \qquad \lambda' = \frac{\lambda P_0}{V} \qquad Q' = \frac{QR}{f_0 V^2},$$

where the prime denotes nondimensional.

In the following text, we will drop the prime from all nondimensional quantities for the sake of brevity and reserve the prime to denote derivatives. Now, the nondimensional form of equations (1) and (2) may be written as :

$$\left(\frac{\partial}{\partial t} + U\frac{\partial}{\partial x}\right)\frac{\partial^2 \psi}{\partial x^2} = \frac{\partial \omega}{\partial p}, \tag{4}$$

$$\left(\frac{\partial}{\partial t} + U\frac{\partial}{\partial x}\right)\frac{\partial \psi}{\partial p} + \lambda\frac{\partial \psi}{\partial x} + \sigma\omega = -\frac{Q}{p}, \tag{5}$$

with $U = \lambda(1 - p)$. The domain now is expressed in the nondimensional form, $0 \le x < \infty$, $p_U \le p \le p_L$.

The vertical boundary conditions are

$$\omega = 0 \qquad \text{at} \qquad p = p_U \ , \ p_L. \tag{6}$$

This is a boundary value problem with 2 equations and 3 unknowns: ψ is perturbation streamfunction, ω is perturbation vertical velocity, and Q is diabatic heating rate (K s^{-1}). To solve the problem, we need to parameterize Q in terms of the wave's variables.

2. Treatment of the diabatic heating

When the atmosphere coupling with an ocean-like surface (with high heat capacity), as shown in the first paper, wave induces strong surface sensible heat flux where air flows over relatively warm surface so that the unstable boundary layer forms in the wave's cold sector. We therefore see the scenario that the wave-induced cumulus convection occurs in the wave's cold sector where descending motion prevails but the PBL is unstable, which presents different wave-convection coupling from the concept of CISK. In partial accordance with the scenario described in the first paper, here we assume that the PBL damps the wave mainly by surface sensible heat flux and convection takes place where the PBL is unstable. Also assume that surface sensible heat flux is upward where the PBL is unstable so that convection occurs where surface sensible heat flux is up. Following previous linear studies (Mak, 1982; Bannon, 1986; Wang and Barcilon, 1986; Mak, 1994), the convective heating is assumed to be distributed vertically according to a specified heating profile. In contrast to prior studies, we do not link convective heating to eddy vertical velocity. Rather, in this study, the convective heating rate is assumed to be proportional to either (1) eddy meridional velocity or (2) eddy temperature at a certain level p_m which approximately is the top of the unstable PBL. Hereafter, we refer to them as the v-parameterization and T-parameteriztion scheme. The two assumptions are based on the consideration that the unstable PBL induced by the wave in our scenario usually occurs in

the wave's cold sector (with southward wind and negative eddy temperature), which is often observed in cyclones over the ocean.

The diabatic heating rate due to convection then can be expressed as

$$Q_1 = -\varepsilon_v \eta(p) v(p_m), \quad \text{(v-parameteriztion)} \tag{7a}$$

or

$$Q_1 = -\varepsilon_T \eta(p) T(p_m), \quad \text{(T-parameteriztion)} \tag{7b}$$

where T denotes eddy temperature, and the vertical heating profile is represented by $\eta(p)$. The convective heating intensity parameters ε_v and ε_T have dimension appropriate to their use: $\varepsilon_v = \frac{\varepsilon_v R}{f_0 V}$, $\varepsilon_T = \frac{\varepsilon_T L}{V}$. For positive heating intensity parameter, a wave induces heating where wind is southward or where eddy temperature is negative (the cold sector of a wave). At the same time, convective cooling exists where wind has a northward component or in the warm sector of a wave. This unconditional convective heating and cooling existing across the wave gives mathematical convenience and may be viewed simply as the contribution to the heating from the fundamental harmonic component (Mak, 1982; Bannon, 1986; Mak, 1994). Use of a convective parameterization without the cooling is not practical in such linear studies since it leads to a Fourier series expansion in space which couples modes of different spatial scales (Lindzen, 1974).

We consider the diabatic heating due to surface sensible heat flux only when the T-parameteriztion is used because using the T-parameteriztion in the presence of surface sensible heat flux is physically closer to the scenario presented in the first paper which is the result with surface fluxes. The diabatic heating rate due to surface sensible heat flux is assumed to be a damping term proportional to eddy temperature at the level p_m .

$$Q_2 = -\gamma\xi(p)T(p_m), \tag{8}$$

where the damping intensity parameter γ like ε_T has dimension s^{-1}, and the vertical damping profile is specified by $\xi(p)$. If $\gamma \geq 0$, surface sensible heat flux heats wave's cold sector and cools wave's warm sector, so it directly damps temperature wave. Therefore, the diabatic heating rate Q can be written as

$$Q = Q_1 + Q_2, \tag{9}$$

Using the hydrostatic relation, we have

$$Q_1 = -\varepsilon_v \eta(p)\frac{\partial\psi(p_m)}{\partial x},$$

or

$$Q_1 = \varepsilon_T \eta(p)\frac{f_0 p_m}{R}\frac{\partial\psi(p_m)}{\partial p},$$

and

$$Q_2 = \gamma\xi(p)\frac{f_0 p_m}{R}\frac{\partial\psi(p_m)}{\partial p},$$

from which the nondimensional forms (ignoring the prime) are:

$$Q_1 = -\varepsilon_v \eta(p)\frac{\partial\psi(p_m)}{\partial x}, \tag{10a}$$

$$Q_1 = \varepsilon_T \eta(p)\frac{\partial\psi(p_m)}{\partial p}, \tag{10b}$$

and

$$Q_2 = \gamma\xi(p)\frac{\partial\psi(p_m)}{\partial p}. \qquad (11)$$

Using the above parameterizations, the unknowns in the system are reduced to only perturbation streamfunction ψ and perturbation vertical velocity ω. We express a wave mode of the solution as the normal mode,

$$(\omega, \psi) = (\Omega(p), \Psi(p))e^{ik(x-ct)}$$

where $i = \sqrt{-1}$, k is wavenumber, and c is the complex phase speed. The amplitude functions $\Omega(p)$ and $\Psi(p)$ are also complex. Substituting the normal mode into equations (4), (5), (7a) and eliminating Ψ in favor of Ω, we obtain the equation using the v-parameterization that governs the amplitude function $\Omega(p)$,

$$\frac{d^2\Omega}{dp^2} + \frac{2\lambda}{U(p)-c}\frac{d\Omega}{dp} - k^2\sigma\Omega = \frac{\varepsilon_v}{U(p_m)-c}\frac{d\Omega(p_m)}{dp}\frac{\eta(p)}{p}. \qquad (12a)$$

Using equations (4), (5), (7b) and (8) for the T-parameterization, we have

$$\begin{aligned}\frac{d^2\Omega}{dp^2} + \frac{2\lambda}{U(p)-c}\frac{d\Omega}{dp} - k^2\sigma\Omega = \\ \frac{i\varepsilon_T p_m \eta(p)}{kp(U(p_m)-c)^2}\left[(U(p_m)-c)\frac{d^2\Omega(p_m)}{dp^2} + \lambda\frac{d\Omega(p_m)}{dp}\right] \\ + \frac{i\gamma p_m \xi(p)}{kp(U(p_m)-c)^2}\left[(U(p_m)-c)\frac{d^2\Omega(p_m)}{dp^2} + \lambda\frac{d\Omega(p_m)}{dp}\right] \qquad (12b)\end{aligned}$$

The boundary conditions,

Upper: $\omega = 0$ at $p = p_U$ and Lower: $\omega = 0$ at $p = p_L$,

now become

$$\text{Upper: } \Omega = 0 \text{ at } p = p_U \tag{13}$$

and

$$\text{Lower: } \Omega = 0 \text{ at } p = p_L . \tag{14}$$

We require that perturbation vertical velocity ω and perturbation streamfunction ψ are continuous at the cloud base and top, which imposes interfacial conditions at the cloud boundaries:

$$\Omega \text{ and } \frac{d\Omega}{dp} \text{ are continuous at cloud base } p_B \text{ and cloud top } p_T \tag{15}$$

The system consisting of equations (12a) or (12b), (13), (14), and (15) formulates an eigenvalue problem for the complex phase speed c.

3. General eigenvalue problem and its solution

Assume that $\Omega_1(p)$ and $\Omega_2(p)$ are two fundamental solutions of the homogeneous equation

$$\frac{d^2\Omega}{dp^2} + \frac{2\lambda}{U(p)-c}\frac{d\Omega}{dp} - \sigma k^2 \Omega = 0, \tag{16}$$

which actually is the Eady problem. Then, in terms of $\Omega_1(p)$ and $\Omega_2(p)$, we construct one solution,

$$f_1(p) = \Omega_2(p_L)\Omega_1(p) - \Omega_1(p_L)\Omega_2(p), \tag{17A}$$

which satisfies the lower boundary condition, and another solution,

$$f_2(p) = \Omega_2(p_U)\Omega_1(p) - \Omega_1(p_U)\Omega_2(p) \qquad (17B)$$

which satisfies the upper boundary condition. Appendix B details the construction of $f_1(p)$ and $f_2(p)$ and also proves that the Wronskian for f_1 and $f_2$is

$$W_R(f_1, f_2; p) \equiv f_1(p)\dot{f}_2(p) - \dot{f}_1(p)f_2(p) = -f_1(p_U)W(p) \neq 0, \qquad (18)$$

where

$$W(p) \equiv \Omega_1(p)\dot{\Omega}_2(p) - \dot{\Omega}_1(p)\Omega_2(p). \qquad (19)$$

It is straightforward to show that $f_1(p_U) = 0$ or $f_2(p_L) = 0$ gives the Eady solution.

The method of variation of parameters can be used to solve the system consisting of the equations (12a), (13), (14), and (15). Derivation is not presented here but it is similar to that for the T-parameterization which is detailed in appendices. The dispersion equation for v-parameterization is

$$F(p_m)f_1(p_U) + \varepsilon_v\left[N(p_m) + \dot{f}_1(p_m)(N_2(p_B) - N_2(p_T))\right] = 0, \qquad (20)$$

where

$$F(p) = U(p) - c,$$

$$N(p) = \dot{f}_2(p)\left[N_1(p_B) - N_1(p)\right] - \dot{f}_1(p)\left[N_2(p_B) - N_2(p)\right],$$

and

$$N_1(p)=\int^{p}\frac{\eta(t)f_1(t)}{tW(t)}dt, \qquad N_2(p)=\int^{p}\frac{\eta(t)f_2(t)}{tW(t)}dt.$$

The eigenfunction is

$$\Omega(p)=\begin{cases} S_1 f_1(p), & p_L \geq p > p_B \\ E_1(p)f_1(p)+E_2(p)f_2(p), & p_B \geq p \geq p_T \\ S_2 f_2(p), & p_T > p \geq p_U \end{cases} \tag{21}$$

where

$$E_1(p)=\frac{-\varepsilon S_1 f_1(p_m)\left[N_2(p)-N_2(p_T)\right]}{f_1(p_U)F(p_m)+\varepsilon N(p_m)}, \tag{22a}$$

$$E_2(p)=\frac{-\varepsilon_v S_1 f_1(p_m)\left[N_1(p_B)-N_1(p)\right]}{f_1(p_U)F(p_m)+\varepsilon_v N(p_m)}, \tag{22b}$$

$$S_2=\frac{-\varepsilon_v S_1 f_1(p_m)\left[N_1(p_B)-N_1(p_T)\right]}{f_1(p_U)F(p_m)+\varepsilon_v N(p_m)}. \tag{22c}$$

In the above equations, S_1 is an arbitrary constant and is set to 1 in the computations. Equation (20) recovers the Eady case $f_1(p_U)=0$ when ε_v=0.

If using the T-parameterization, the system consists of the equations (12b), (13), (14), and (15). Because of the two forcing terms that have different vertical profiles, we solve the system by applying the method of variation of parameters twice. By doing so, the solution outside cloud region reduces to the modified Eady solution in the presence of surface-flux damping, and the solution reduces to the Eady solution when convective heating and surface temperature damping are all zero.

First, applying the method of variation of parameters to equation (12) without convective heating (ε=0), we get two linearly independent solutions

$$g_1(p) = (A_1(p) + 1) f_1(p) + B_1(p) f_2(p), \tag{23a}$$

$$g_2(p) = A_1(p) f_1(p) + (B_1(p) + 1) f_2(p), \tag{23b}$$

where

$$A_1(p) = \frac{i\gamma p_m}{k f_1(p_U) F^2(p_m)} \left[F(p_m) \frac{d^2\Omega_s(p_m)}{dp^2} + \lambda \frac{d\Omega_s(p_m)}{dp} \right] \int_{p_U}^{p} \frac{\xi(t) f_2(t)}{tW(t)} dt, \tag{24a}$$

$$B_1(p) = \frac{-i\gamma p_m}{k f_1(p_U) F^2(p_m)} \left[F(p_m) \frac{d^2\Omega_s(p_m)}{dp^2} + \lambda \frac{d\Omega_s(p_m)}{dp} \right] \int_{p_L}^{p} \frac{\xi(t) f_1(t)}{tW(t)} dt, \tag{24b}$$

The subscript "s" denotes the solution for surface damping only. Appendix C describes the solving process in detail and shows that the Wronskian for g_1 and g_2 is

$$W_R(g_1, g_2; p) = -f_1(p_U)(A_1(p) + B_1(p) + 1) W(p), \tag{25}$$

which is not equal to zero in the presence of diabatic heating, so $g_1(p)$ and $g_2(p)$ are linearly independent.

Then, in terms of $g_1(p)$ and $g_2(p)$, we apply the method of variation of parameters to (12). The following dispersion equation can be obtained (Appendix D):

$$D_1 f_1(p_U) - \frac{i\varepsilon_T p_m}{kF^2(p_m)} \left[F(p_m) \frac{d^2\Omega(p_m)}{dp^2} + \lambda \frac{d\Omega(p_m)}{dp} \right] \left(I_2(p_B) - I_2(p_T) \right) = 0. \tag{26}$$

The eigenfuntion is given by

$$\Omega(p)=\begin{cases} D_1 g_1(p), & p_L \geq p > p_B \\ A_2(p)g_1(p)+B_2(p)g_2(p), & p_B \geq p \geq p_T \\ D_2 g_2(p), & p_T > p \geq p_U \end{cases} \tag{27}$$

where

$$A_2(p)=\frac{i\varepsilon_T p_m}{kf_1(p_U)F^2(p_m)}\left[F(p_m)\frac{d^2\Omega(p_m)}{dp^2}+\lambda\frac{d\Omega(p_m)}{dp}\right]\left[I_2(p)-I_2(p_T)\right], \tag{28a}$$

$$B_2(p)=\frac{i\varepsilon_T p_m}{kf_1(p_U)F^2(p_m)}\left[F(p_m)\frac{d^2\Omega(p_m)}{dp^2}+\lambda\frac{d\Omega(p_m)}{dp}\right]\left[I_1(p_B)-I_1(p)\right], \tag{28b}$$

$$D_2=\frac{i\varepsilon_T p_m}{kf_1(p_U)F^2(p_m)}\left[F(p_m)\frac{d^2\Omega(p_m)}{dp^2}+\lambda\frac{d\Omega(p_m)}{dp}\right]\left[I_1(p_B)-I_1(p_T)\right]. \tag{28c}$$

And,

$$\frac{d^2\Omega(p_m)}{dp^2}=D_1\frac{H_1(p_m)g_1'(p_m)+i\varepsilon_T\lambda H_2(p_m)g_1(p_m)}{H_1(p_m)-i\varepsilon_T F(p_m)H_2(p_m)}, \tag{29}$$

$$\frac{d\Omega(p_m)}{dp}=\left\{D_1 kf_1(p_U)F^2(p_m)g_1'(p_m)+i\varepsilon_T p_m I(p_m)F(p_m)\frac{d^2\Omega(p_m)}{dp^2}\right\}\Big/H_1(p_m) \tag{30}$$

$$I_1(p)=\int^p\frac{\eta(t)g_1(t)}{tW(t)[A_1(t)+B_1(t)+1]}dt, \tag{31a}$$

$$I_2(p)=\int^p\frac{\eta(t)g_2(t)}{tW(t)[A_1(t)+B_1(t)+1]}dt, \tag{31b}$$

$$I(p) = g_2^{\cdot}(p)\left[I_1(p_B) - I_1(p)\right] - g_1^{\cdot}(p)\left[I_2(p_B) - I_2(p)\right], \tag{32a}$$

$$J(p) = g_2^{\cdot\cdot}(p)\left[I_1(p_B) - I_1(p)\right] - g_1^{\cdot\cdot}(p)\left[I_2(p_B) - I_2(p)\right], \tag{32b}$$

$$H_1(p) = kf_1(p_U)F^2(p) - i\varepsilon_T \lambda p I(p), \tag{33a}$$

$$H_2(p) = pJ(p) - \eta(p)f_1(p_U). \tag{33b}$$

For convenience, the arbitrary constant D_1 is set to 1. It can be seen that when convective heating is absent ($\varepsilon_T = 0$) the dispersion equation (26) reduces to he Eady case $f_1(p_U) = 0$, and outside the cloud the eigenfunction is the same as that with surface damping only.

Model result and analysis

1. Model parameters and vertical profiles

Given the basic state [$U(p)$ and $\sigma(p)$], the intensity parameters (ε_v or ε_T and γ), the vertical profiles [$\eta(p)$ and $\xi(p)$], and the two fundamental solutions of the reduced equation (16), the dispersion equation (23) can be solved iteratively by using the secant method. Once the complex phase speed c is obtained, the eigenfunction (24) can be computed. In the computations, the following values for the parameters are chosen to reasonably represent the atmosphere:

$p_U = 150hPa$, $p_T = 400hPa$, $p_B = 900hPa$,

$p_L = 1000hPa$, $p_m = 900hPa$, $\lambda = 0.035ms^{-1}(hPa)^{-1}$,

$\sigma = 0.04m^2s^{-2}(hPa)^{-2}$, $f = 10^{-4}s^{-1}$.

Using the characteristic values L=10^6 m, P_0=1000 hPa, $V = \lambda P_0$ ms^{-1} the nondimensional values of the above parameters would be:

$$p_U = 0.15, \quad p_T = 0.4, \quad p_B = 0.9, \quad p_L = 1.0,$$
$$p_m = 0.9, \quad \lambda = 1.0, \quad \sigma = 4.0,$$

where the prime has been dropped. The nondimensional zonal flow now is U(p) = 1 - p.

In Jiang (1994), the convective heating rate in wave's cold sector was about 0.2K/day on day 7 and 10K/day on day 13 when the wave reached the maximum amplitude. In this study, the value of the convective heating intensity parameter from 0.0001 to 5.0 is examined to test the sensitivity to this parameter. The range is wide enough since ε_v=1.0 corresponds to 4 K/day for a wind speed of 10 m/sec. and ε_T=0.33 corresponds to 10 K/day for eddy temperature of 10 K (In later sections, ε_T is rescaled so that ε_T = 1.0 corresponds to this heating rate). For each parameter setting, the wavenumber of the normal mode is scanned from 0.001 to 10 with the increment 0.001.

The nondimensional heating profile is specified as in Wang and Barcilon (1986):

$$\eta(p) = \begin{cases} 0, & p_B < p \le p_L \\ \dfrac{12}{(p_B - p_T)^4}[b(p_B - p)(p - p_T)^2 & \\ \quad +(1-b)(p_B - p)^2(p - p_T)], & p_T \le p \le p_B \\ 0, & p_U \le p < p_T \end{cases} \tag{34}$$

where the shape parameter b can be chosen in [0,1] to adjust the location of maximum heating in the cloud (Fig.2.1). In accordance with the result in the first paper, the

maximum heating is located in the lower part of the cloud by setting b = 1 in most of the computations.

Assume the surface damping exponentially decreases with height, and the nondimensional damping profile is specified as

$$\xi(p) = \frac{ae^{-a(1-p/p_L)}}{p_L(1-e^{-a(1-p_U/p_L)})}, \tag{35}$$

where the parameter a controls how fast the surface damping decreases with height, and it is set so that the damping at the level p_m reduces to e^{-3} of the surface value . The damping intensity parameter γ is set to 1.0 which corresponds to sensible heat flux 100 Wm^{-2} at 1 km above the surface when surface eddy temperature is about 10 K. The shapes of the damping profile and the different convective heating profiles are given in Figure 2.1.

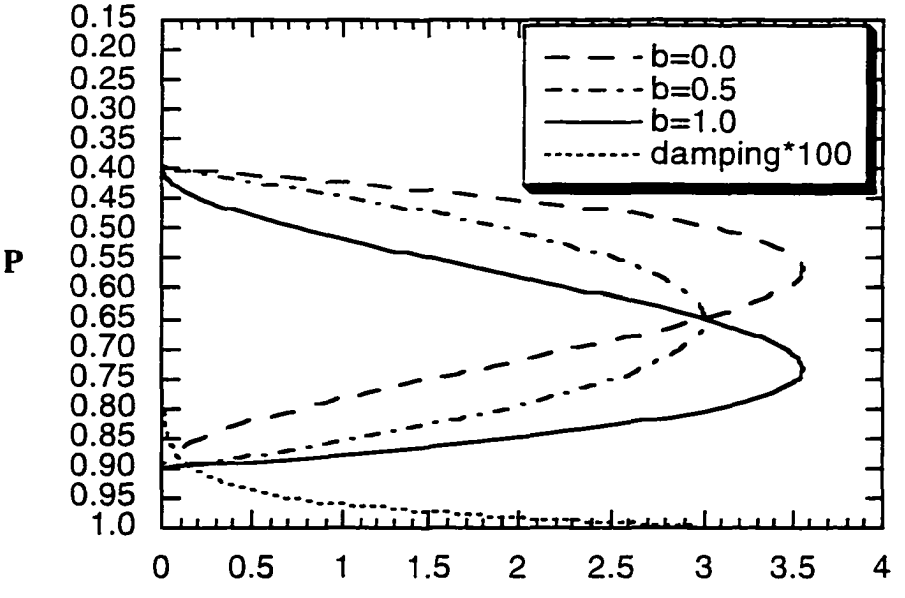

Figure 2.1 The shape of the vertical heating profiles $\eta(p)$ with different b values and vertical damping profile $\xi(p)$ x100.

Two fundamental solutions of (16) are in the following form (see Appendix E for the detail):

$$\Omega_1(p) = \frac{1}{\sqrt{2}} e^{\mu(1-p-c)}\left[\mu(1-p-c)-1\right]$$

$$\Omega_2(p) = \frac{1}{\sqrt{2}} e^{-\mu(1-p-c)}\left[\mu(1-p-c)+1\right]$$

where $\mu = \sigma^{1/2}k$. Then, we know that

$$W(p) = \Omega_1(p)\Omega_2'(p) - \Omega_2(p)\Omega_1'(p) = \mu^3(1-p-c)^2,$$

$$f_1(p) = \mu(p_L - p)\cosh[\mu(p_L - p)] - \left[\mu^2(c-1+p_L)(1-p-c)+1\right]\sinh[\mu(p_L - p)],$$

$$f_2(p) = \mu(p_U - p)\cosh[\mu(p_U - p)] - \left[\mu^2(c-1+p_U)(1-p-c)+1\right]\sinh[\mu(p_U - p)].$$

One can now solve the dispersion equation (20) or (26) by iteration.

2. Comments about the solution to the eigenvalue problem

To consider the effect of convective heating, the domain is divided vertically into three regions and the method of variation of parameters is applied to solve the system. Because it is not practical to get exact analytical solutions from the dispersion equation, we do not know how many solutions exist. We apply the following numerical procedure to search for solutions. The dispersion equation is solved numerically by iteration in complex phase speed space, where initial guess values are scanned through [0, 1] for the real part

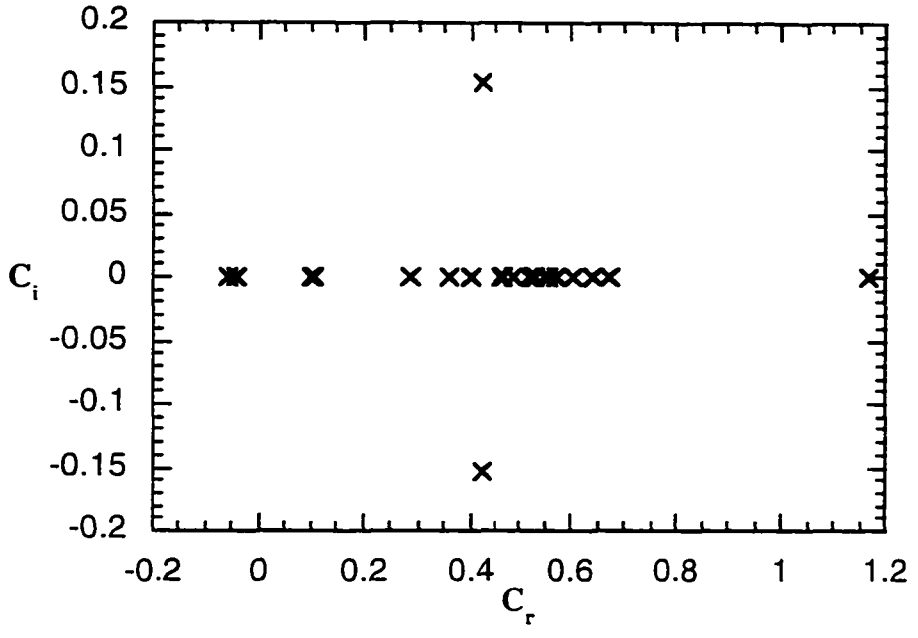

Figure 2.2 Numerical solutions to the v-parameterization system when k=1.0 and ε_v=0.001.

and [-0.15, 0.15] for the imaginary part. Figure 2.2 shows the solutions to the v-parameterization model when k=1.0 and ε_v=0.001. We can clearly see there is a pair of complex conjugates $(0.425, \pm 0.154)$, the Eady solution recovered in the moist system. Compared to the Eady model, the system has some other mathematical solutions which are stable with the weak convective heating. These stable solutions are presumably due to the numerical computation of the integrals N(p), I(p), and J(p). In the iterative computation, these integrals are numerically computed using the trapezoidal rule by discretizing the continuous domain into 100 levels. The continuous problem has a continuous spectrum of neutral waves, but the discretizing approximation could generate a discretized spectrum of

neutral waves(Farrell, 1982). Because our focus is the effect of convective heating on baroclinically growing waves, we only examine the variation of the Eady-type modes with convective heating.

3. The v-parameterization model

3-1. Eigenvalue analysis: instability properties of the waves

Figure 2.3 gives growth rate as a function of wavenumber for different heating intensities. We can see first that Eady's results are recovered when heating is very small. As the heating intensity parameter ε_v increases, the growth rate of the unstable waves decreases. When ε_v>0.1, the growth rate starts to increase and the wavenumber of the most unstable wave shifts towards 1.5, the wavenumber of short wave cutoff. Meanwhile, the real part of the wave's phase speed decreases as ε_v increases to 0.01, then it increases with further heating increases (not shown).

The variation of phase speed and growth rate for the whole range of ε_v under consideration can be viewed in part in Figure 2.4 which shows their behavior for wavenumber k=0.9. The phase speed increases rapidly when ε_v increases from 0.01 to 1.0, then it gradually approaches 0.6. Although the growth rate increases as ε_v becomes larger than a certain value, it does not reach the value for Eady's solution even if heating becomes extremely large. The most unstable mode of the Eady solution has the growth rate about 0.154 and wavenumber between 0.9 and 1. In the following analysis, we examine variations of the structure and energetics for the unstable stable wave k=0.9.

3-2. Eigenfunction analysis: structure of the unstable waves

The vertical structure variations of vertical velocity Ω are presented in Figures 2.5(a) and (b). Firstly, we have to keep in mind that the eigenfunctions have been

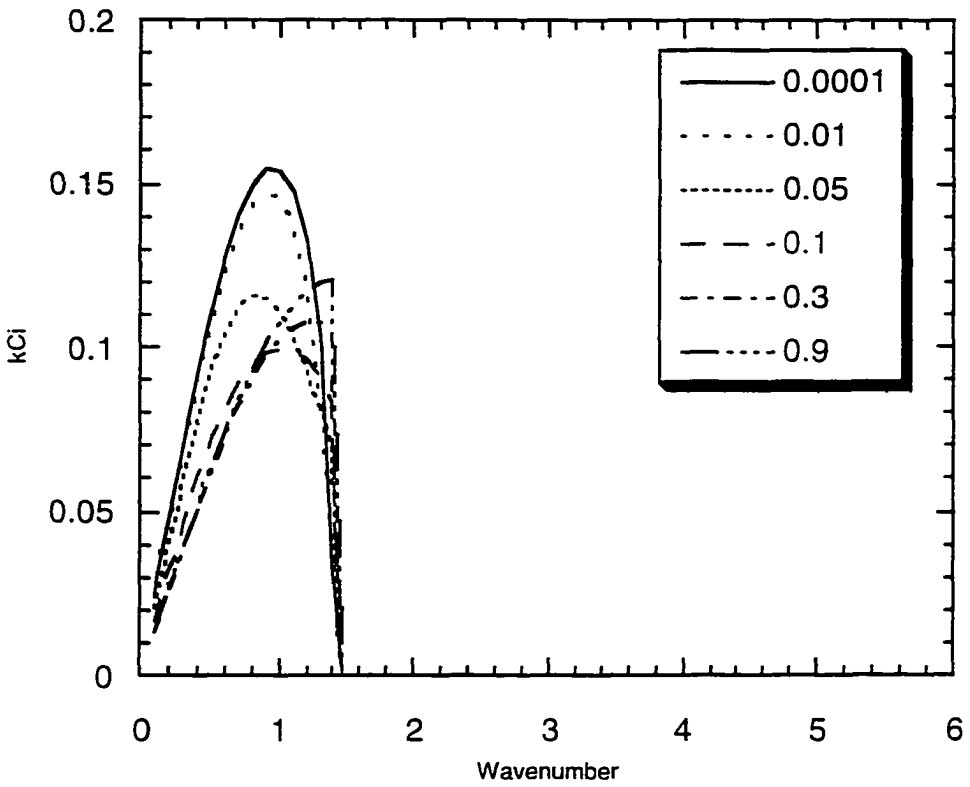

Figure 2.3 Result of the v-parameterization model, variations of the growth rate with the wavenumber for different heating intensities shown in key.

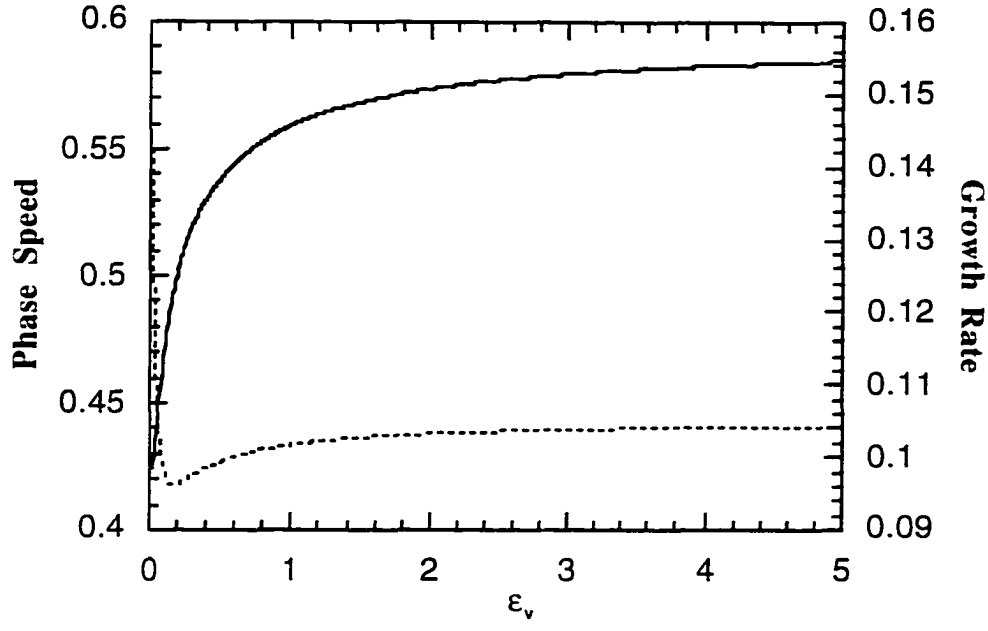

Figure 2.4 Result of the v-parameterization model, variations of the phase speed (solid curve) and growth rate (dotted curve) for wavenumber k=1 as a function of ε_v.

arbitrarily normalized to unity at the lower boundary. Therefore, it is meaningless to compare the absolute value of all eigenfunctions, and only the structures are unique and meaningful (Mak, 1994). We can see that the wave structures have changed in presence of convective heating. As ε_v increases, the maximum amplitude shifts toward the upper atmosphere. The maximum amplitude is about 575 hPa for ε_v=0.0001 and 520 hPa for ε_v=0.1. In the meantime, the phase angle decreases with increasing ε_v as shown in Figure 2.5(b). With increasing convective heating, the wave below 550 hPa tilts less westward than the Eady wave, which is consistent with smaller growth rate than the Eady wave's.

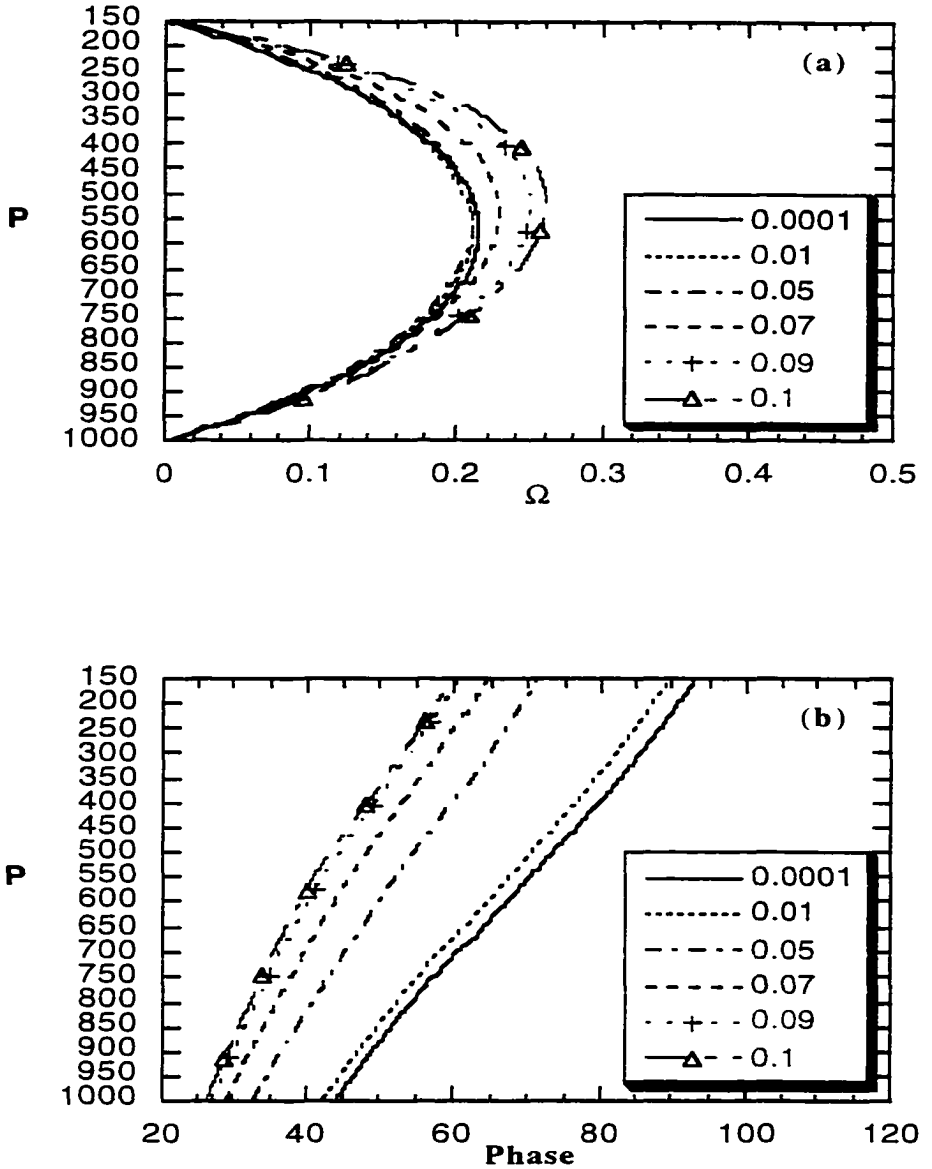

Figure 2.5 Result of the v-parameterization model, the vertical structure of the vertical velocity (a) amplitude Ω and (b) phase angle for wavenumber k=0.9, for different heating intensities ε_v.

The vertical structure of streamfunction Ψ (Figs. 2.6(a) and 2.6(b)) has corresponding variations in presence of convective heating. In Figure 2.6(a), the minimum amplitude of streamfunction Ψ shifts toward the upper atmosphere when heating intensity increases. Similarly, in Figure 2.6(b), the phase angle decreases when heating intensity increases. Below 550 hPa, the wave's westerly tilt reduces as the heating parameter ε_v becomes larger.

The effect of convective heating also is shown in the vertical structure of the wave's temperature T. In Figure 2.7(a), the shape of temperature amplitude above the cloud base (900 hPa) becomes more zigzag as the heating intensity increases. As the heating strengthens, the temperature between the level with maximal heating and the cloud top increases with height. In Figure 2.7(b), the phase angle below the cloud base (900 hPa) hardly changes with convective heating, while the phase angle above the cloud base decreases when heating becomes stronger. With increasing heating parameter ε_v, the temperature wave becomes more eastward tilting between 900 hPa and 600 hPa, but it is more westward tilting between 600 hPa and 400 hPa.

As we can see, the wave structure changes in presence of convective heating so that the perfect phase relationship existing in the Eady wave is not present with convective heating. Recall that for the Eady case, temperature wave lags $\pi/4$ radians behind the geopotential height wave and π radians behind the vertical velocity wave in the p-coordinate so that warm air ascends and cold air descends, giving the optimal structure for converting EPE to EKE. Table 2-1 shows the phase-angle difference for different heating parameters between the vertical velocity wave and the temperature wave at the level where the vertical velocity wave amplitude reaches its maximum. We see that the location of maximum vertical velocity rises as convective heating increases, which is also shown in the eigenfunction analysis. The phase-angle difference decreases from 180.0 to 143.8 as ε_v

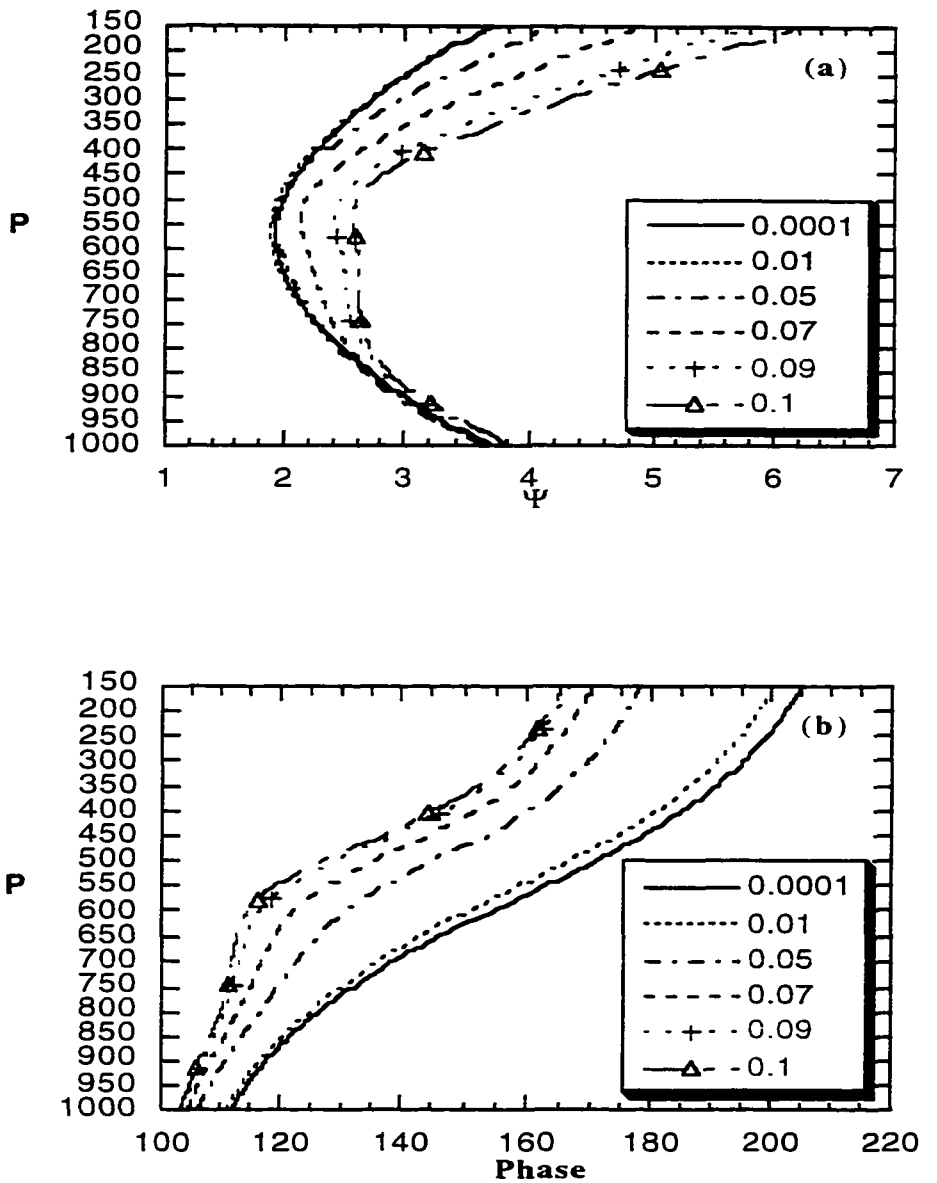

Figure 2.6 Result of the v-parameterization model, the vertical structure of the streamfunction (a) amplitude Ψ and (b) phase angle for wavenumber k=0.9, for different heating intensities ε_v.

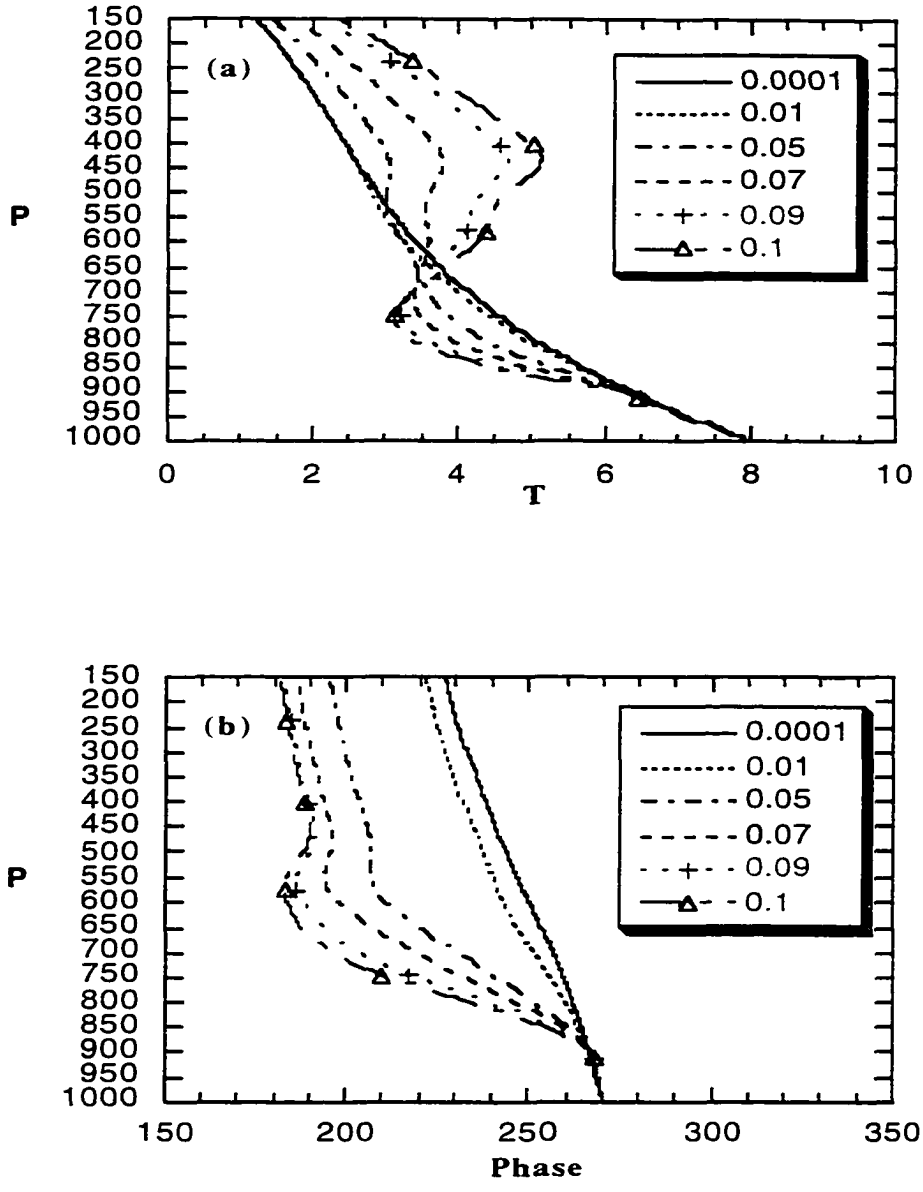

Figure 2.7 Result of the v-parameterization model, the vertical structure of the streamfunction (a) amplitude T and (b) phase angle for wavenumber k=0.9, for different heating intensities ε_v.

TABLE 2-1 Result of the v-parameterization model, Phase-angle difference between vertical velocity wave and temperature wave at the level where vertical velocity wave amplitude is largest

ε_v	p at max(Ω)	Phase difference (T-Ω)
0.0001	575.0 hPa	180.0
0.01	575.0 hPa	175.8
0.1	519.7 hPa	143.8
0.3	460.0 hPa	149.9
0.9	426.2 hPa	159.9

increases to 0.1, then it increases as ε_v further increases. This helps us to understand the wave's instability behavior. When convective heating gets stronger, the wave structure changes and the warm and cold regions do not match with the ascent and descent motion regions as well as in the Eady case, so the wave in presence of convective heating converts EPE to EKE suboptimally and it no longer can grow as fast as the Eady wave does. As convective heating further increases and becomes dominant, it tends to establish a new heating center and flip the wave's cold and warm region.

3-3. Energetic analysis

The energetic analysis is based on the following equations derived from (4) and (5):

$$\frac{\partial}{\partial t}\left\langle \frac{1}{2}\left(\frac{\partial \psi}{\partial x}\right)^2 \right\rangle = -\left\langle \frac{\partial}{\partial p}(\omega\psi) \right\rangle + \left\langle \omega \frac{\partial \psi}{\partial p} \right\rangle, \tag{36a}$$

$$\frac{1}{2\sigma}\left\langle\frac{\partial}{\partial t}\left(\frac{\partial\psi}{\partial p}\right)^2\right\rangle+\frac{\lambda}{\sigma}\left\langle\frac{\partial\psi}{\partial x}\frac{\partial\psi}{\partial p}\right\rangle+\left\langle\omega\frac{\partial\psi}{\partial p}\right\rangle=\frac{1}{\sigma}\left\langle\frac{\partial\psi}{\partial p}\frac{-Q_1}{p}\right\rangle+\frac{1}{\sigma}\left\langle\frac{\partial\psi}{\partial p}\frac{-Q_2}{p}\right\rangle. \qquad (36b)$$

Note that the equations are nondimensional, the angle brace denotes an average over a wavelength, and the diabatic heating due to surface sensible heat flux Q_2 is 0 for the v-parameterization system. The first term on the r.h.s. of the kinetic energy equation (36a) is the divergence of vertical wave-energy flux, DIV[EE]. Vertically integrating through the whole atmosphere, this term goes to zero because divergence balances convergence due to the boundary conditions on ω. The second term on the r.h.s. of (36a) is the conversion rate from eddy available potential energy (EPE) to eddy kinetic energy (EKE), C[EPE,EKE], which also appears with opposite sign in the potential energy equation (36b). The second term on the l.h.s. of (36b) is the conversion rate from zonal available potential energy (ZPE) to EPE, C[ZPE, EPE]. On the r.h.s. of (36b) are the contributions of diabatic heating to the EPE generation.

Using $\Omega(p)$ and $\Psi(p)$, we can evaluate the wave's energy budget. Figure 2.8 shows the vertical structure of the integrands for the energy budget terms in of (36a,b) for wavenumber k=0.9 and ε_v=0.0001. We can see the energy flow path of typical baroclinic waves: meridional motion converts ZPE to EPE, and vertical motion converts EPE to EKE. While C[ZPE, EPE] is vertically uniform, the energy conversion C[EPE, EKE] has a maximum in the middle of the atmosphere where eddy vertical velocity is largest in magnitude. The contribution of convective heating, G[CONV], is negligible in this case.

Convection in the wave's cold sector negatively contributes to the energy cycle because the convective heating decreases the wave's vertical motion and reduces energy conversion from EPE to EKE. When convective heating becomes moderate (ε_v=0.05), its negative contribution to EPE becomes important and the wave structure changes

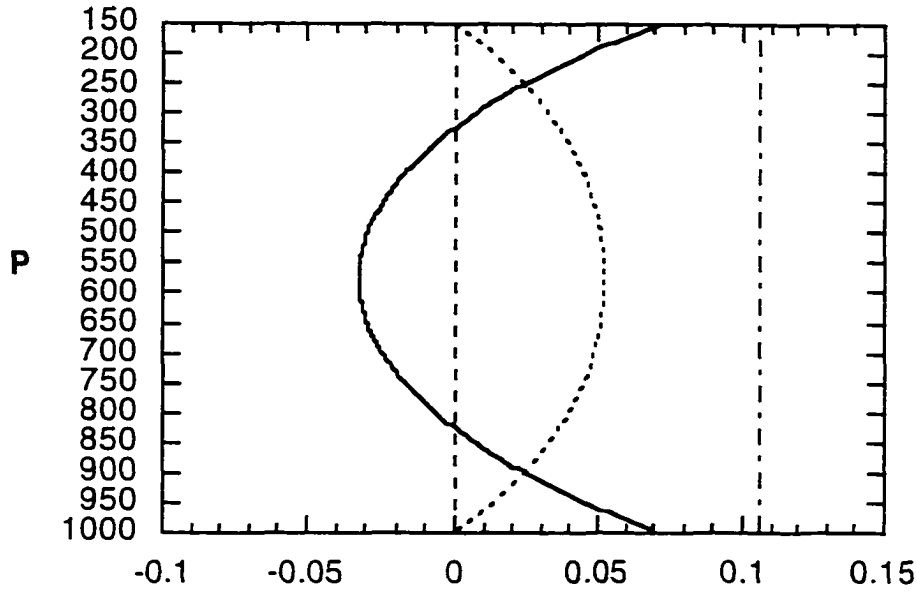

Figure 2.8 Result of the v-parameterization model, vertical distribution of the energy budget terms for wavenumber k=0.9 and ε_v=0.0001. Solid line denotes DIV[EE], dotted line represents C[EPE,EKE], dash-dotted line is for C[ZPE,EPE], and dashed line for contribution of convective heating G[CONV].

accordingly. In Figure 2.9, we see the vertical distributions of DIV[EE], C[EPE,EKE], and C[ZPE,EPE] have changed. The variations between 650 hPa and 400 hPa correspond to eddy temperature variation in the same vertical section (cf. Fig. 2.7). However, the energy flow still follows the path of typical baroclinic waves as in the Eady case.

Because the linear instability problem has arbitrary normalization, it is meaningless to compare the absolute values of the energy terms for different heating intensity.

However, we can compare sizes of C[EPE,EKE] and G[CONV] relative to C[ZPE,EPE]. In other words, we can compare the ratios

$$C^*[EPE,EKE] = \frac{C[EPE,EKE]}{C[ZPE,EPE]}, \text{ and } G^*[CONV] = \frac{G[CONV]}{C[ZPE,EPE]}$$

for different heating parameter ε_v. Table 2-2 gives the values of the two ratios for various ε_v. Note that $C^*[EPE,EKE]$ does not change with heating intensity when ε_v is small. As ε_v grows to 0.05, the negative contribution of convective heating (-0.26) becomes comparable in magnitude to $C^*[EPE,EKE]$, which decreases to 0.33. When convective heating increases further, the absolute value of $G^*[CONV]$ decreases while $C^*[EPE,EKE]$ continues to decrease. This shows that the wave-induced convection decreases when the wave gets weak because of the negative contribution of convective heating decreased. Eventually, the effect of convective heating alters the wave's structure by so much that $G^*[CONV]$ becomes positive. It is pertinent to point out here that the energy conversion C[ZPE,EPE] also changes in the presence of convective heating, but its variation with heating intensity can not be seen in this analysis.

Summarizing the results, we get the wave's behavior in the presence of convection. With weak convection, the wave's structure does not change much while the EPE generation decreases due to negative contribution of convection. In the presence of moderate convective heating, although the EPE generation still decreases, the wave's temperature structure changes accordingly to minimize the negative effect of convection. For strong convective heating, the wave's temperature structure changes so much that the wave adapts itself to draw its energy from the positive contribution of convection, and the growth rate and phase speed increases.

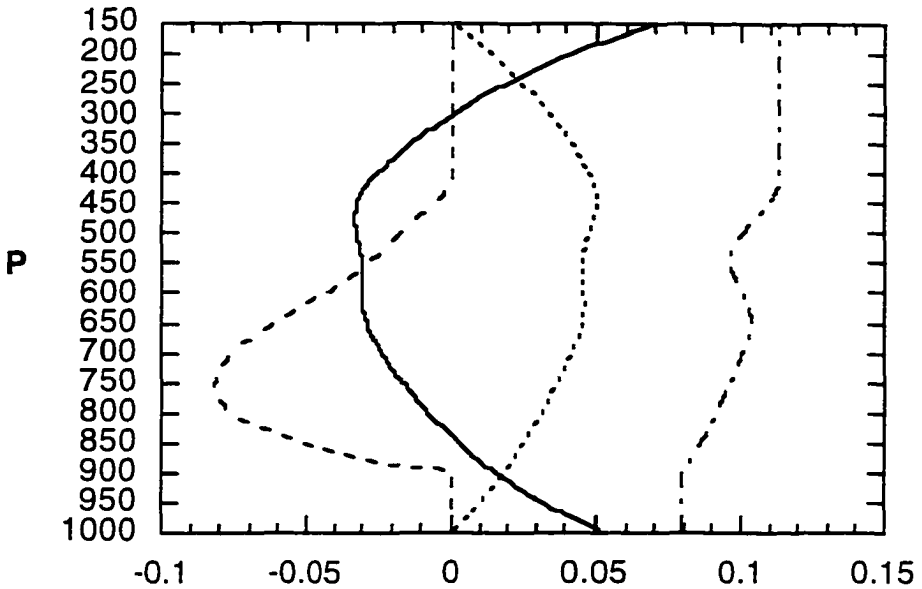

Figure 2.9 Same as Fig. 2.8 excpt for ε_v=0.05.

TABLE 2-2 Result of the v-parameterization model, the vertically-integrated energy budget terms of wavenumber k=0.9 for different heating intensities

ε_v	$C^*[EPE, EKE]$	$G^*[CONV]$
0.0001	0.34	-0.0007
0.01	0.34	-0.0704
0.05	0.33	-0.2617
0.07	0.32	-0.2436
0.09	0.31	-0.1821
0.1	0.30	-0.1474
0.2	0.24	0.1453

4. The T-parameterization model

Is the growing wave's behavior delineated above dependent on the convective parameterization? Since convection occurs in the wave's cold sector where the wave-induced boundary layer is unstable, it is more intuitively physical to relate convective heating with eddy temperature in the boundary layer and include surface damping effect. In the next, we examine the result using the T-parameterization and considering surface temperature damping in the model.

4-1. Eigenvalue analysis: instability properties of the waves

As with the v-parameterization, let us first look at the variations of the growth rate with the wavenumber for different heating intensities. In Figure 2.10, as expected, the Eady solution was recovered when convective heating was negligible. As the heating parameter ε_T increases in Figure 2.10, the growth rate of unstable waves initially

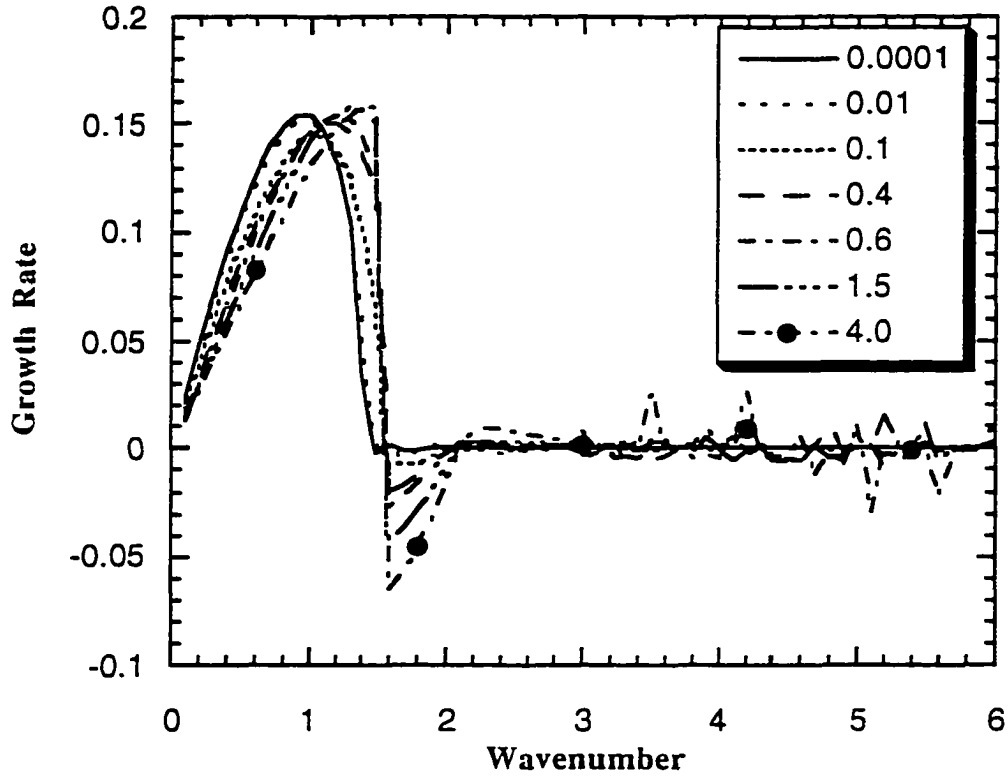

Figure 2.10 Result of the T-parameterization model, variations of the growth rate with the wavenumber for different heating intensities shown in key.

decreases, then increases, and the wavenumber of the most unstable wave shifts toward the short wave cutoff. In comparison to the result of the v-parameterization model, the decrease of growth rate is not as large, and the maximum growth rate does not fall below 0.1. Also, with strong heating, the maximum growth rate increases to a value equal to or larger than the Eady solution's maximum. Moreover, the phase speed (not shown) increases even when the heating is quite weak.

4-2. Eigenfunction analysis: structure of the unstable waves

In parallel to the v-parameterization analysis, in this section we examine the structure of the wave with wavenumber k=0.9, focusing on the shape of the eigenfunctions. Figures 2.11(a) and (b) show the vertical structure variations of vertical velocity Ω when convective heating changes. The structure of the amplitude and phase angle barely change with ε_T for weak heating (ε_T <0.01), but the level of maximum amplitude rises into the upper atmosphere as ε_T increases to 0.1 (Fig. 2.11(a)). The phase angle decreases substantially as $\varepsilon_T \rightarrow 0.1$. The result overall is qualitatively similar to that using the v-parameterization model (cf. Figs. 2.5(a) and (b)).

The vertical structure of streamfunction Ψ varies with convective heating as shown in Figures 2.12(a) and (b), which exhibits some differences from the result using the v-parameterization. When $\varepsilon_T = 0.1$, the level of minimum amplitude shifts toward the lower atmosphere (Fig. 2.12(a)), in contrast to the behavior in Figure 2.6(a). As shown in Figure 2.12(b), the phase angle similarly decreases as the heating parameter ε_T increases, but there is no systematic tilting change as seen in Figure 2.6(b). Consistent with Figures 2.11(a) and (b), though, the structure of amplitude and phase angle changes little with ε_T when heating is small (ε_T <0.01).

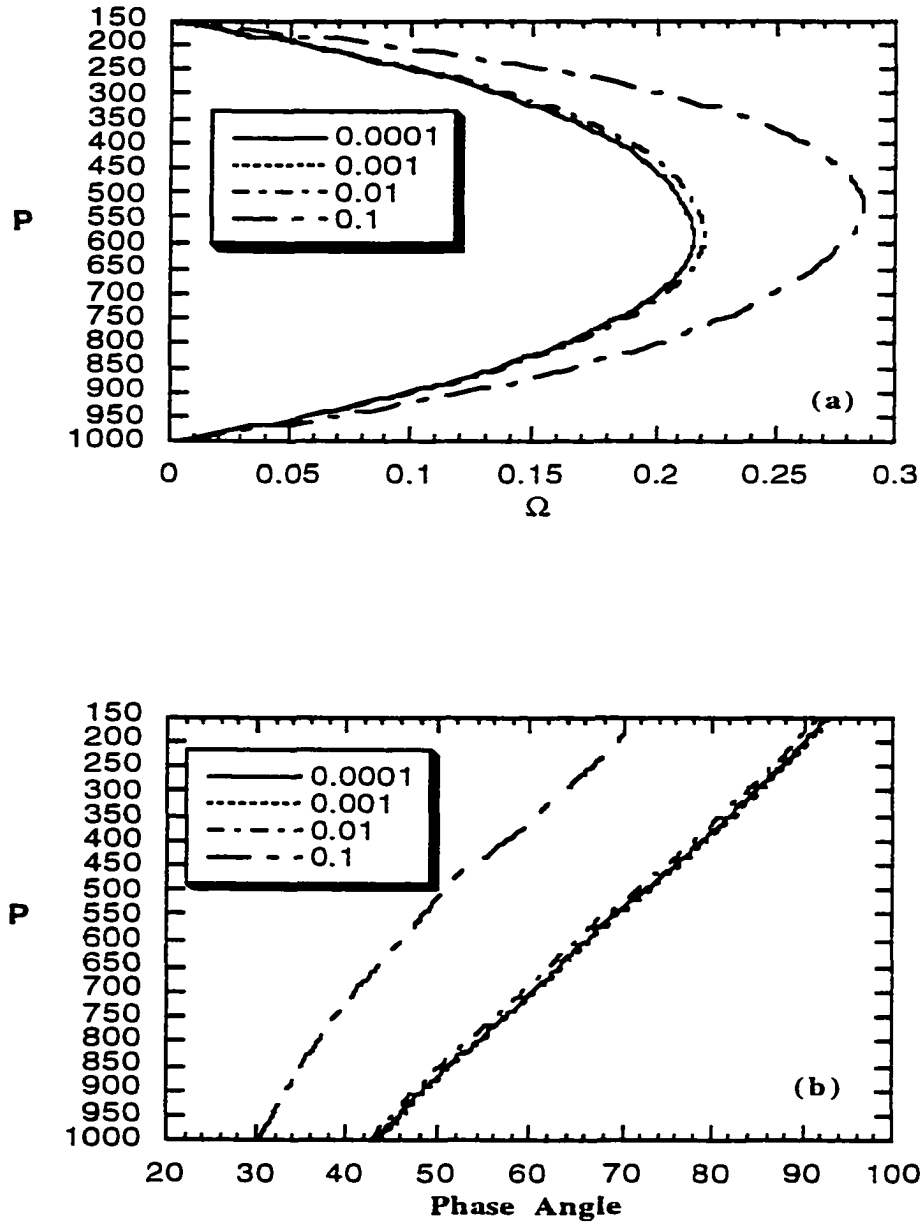

Figure 2.11 Result of the T-parameterization model, the vertical structure of the vertical velocity (a) amplitude Ω and (b) phase angle for wavenumber k=0.9, for different heating intensities ε_T.

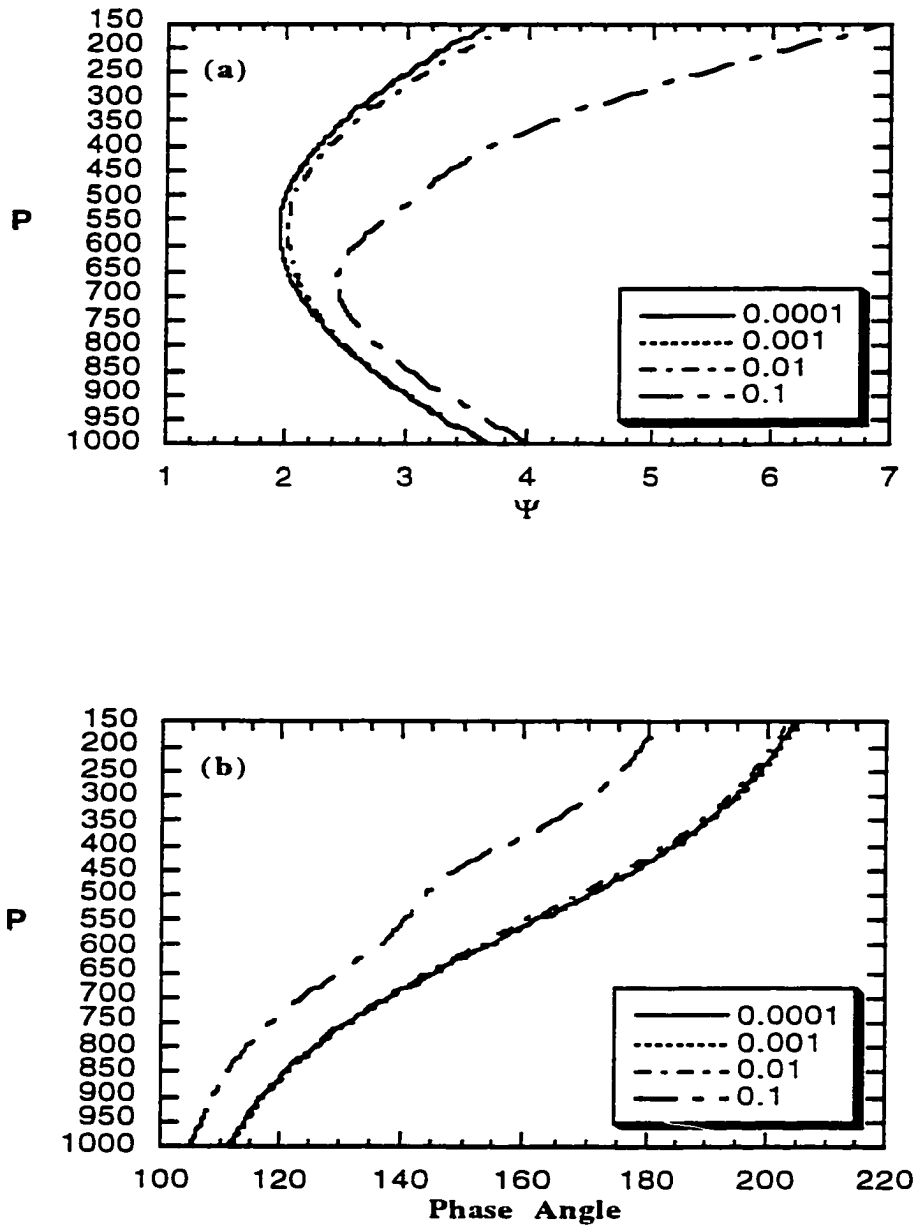

Figure 2.12 Result of the T-parameterization model, the vertical structure of the vertical velocity (a) amplitude Ψ and (b) phase angle for wavenumber k=0.9, for different heating intensities ε_T.

Figures 2.13(a) and (b), respectively, show the variations in the vertical structure of the wave's temperature T when the heating parameter ε_T changes. Both amplitude and phase angle changes are similar to the result of the v-parameterization model. In Figure 2.13(a), the temperature amplitude between the level with maximum heating and the cloud top increase with height when $\varepsilon_T = 0.1$. With the same heating intensity ($\varepsilon_T = 0.1$), the structure of phase angle changes so much that the temperature wave becomes more eastward tilting between 900 hPa and 550 hPa, but more westward tilting between 550 hPa and 400 hPa (Fig. 2.13(b)). In the lower atmosphere, the phase angle change with heating intensity is again negligible. Similarly we can see little change in the structure of amplitude and phase angle with small convective heating.

The wave structure change can be more clearly seen in vertical-horizontal cross-section plots. As a reference state for comparison, Figure2.13 shows the eigenfunction cross-sections of virtical velocity, streamfunction,and temperature for the Eady case. It is shown that the vertical velocity and streamfunction are vertically symmetric and tilt westward with height. The temperature tilts eastward with height, and its amplitude decreases with height. When heating intensity increases to 0.1, the change in the vertical velocity field is not visibly shown in Figure 2.14(a), while the streamfunction field becomes asymmetric and a local center is developing near 700hPa (Fig. 2.14(b)). Figure 2.14(c) clearly showed the structure modification in temperature wave by convective heating. In the vertical region with strong convective heating or cooling, warm sector horizontally nudges into cold sector and cold sector also nudges into warm sector. It can be viewed as the result superimposing convective heating (Fig. 2.14(d)) to the temperature field of the Eady case (Fig. 2.13(c)).

When heating intensity increases to 1.0, the structure change due to convective heating can be seen in vertical velocity, streamfunction, and temperature fields. The

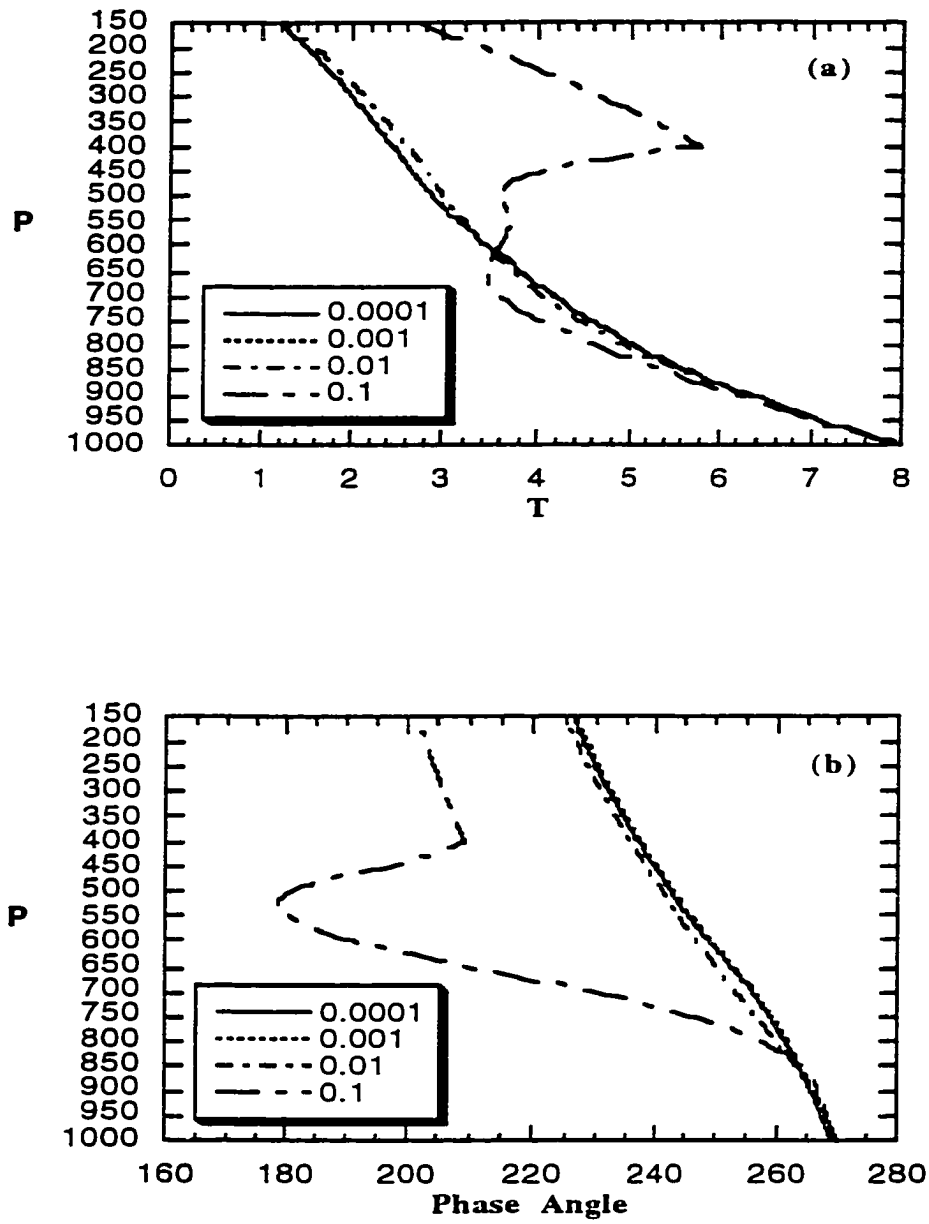

Figure 2.13 Result of the T-parameterization model, the vertical structure of the vertical velocity (a) amplitude T and (b) phase angle for wavenumber k=0.9, for different heating intensities ε_T.

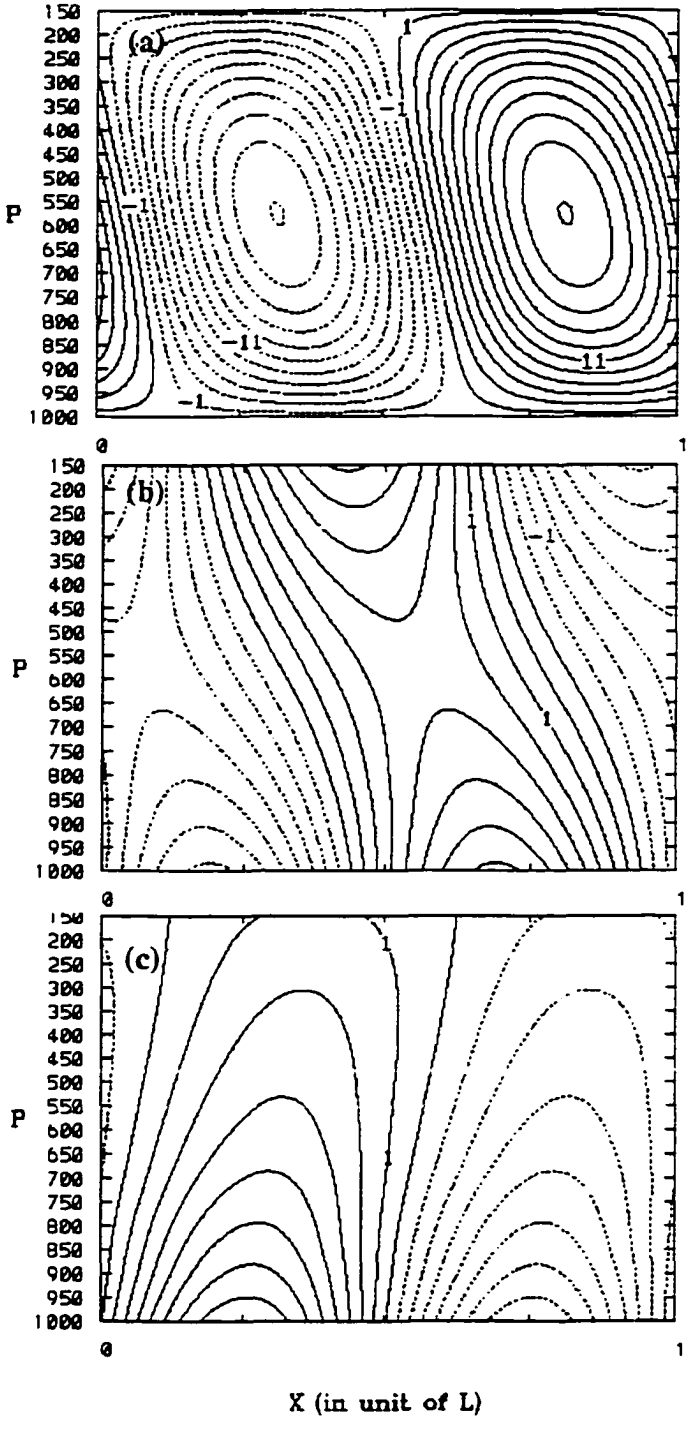

Figure 2.14 Result of the T-parameterization model, the vertical-horizontal cross-section of (a) vertical velocity ω, (b) streamfunction ψ, and (c) temperature T for wavenumber k=0.9, for the Eady case (ε_T=0.0).

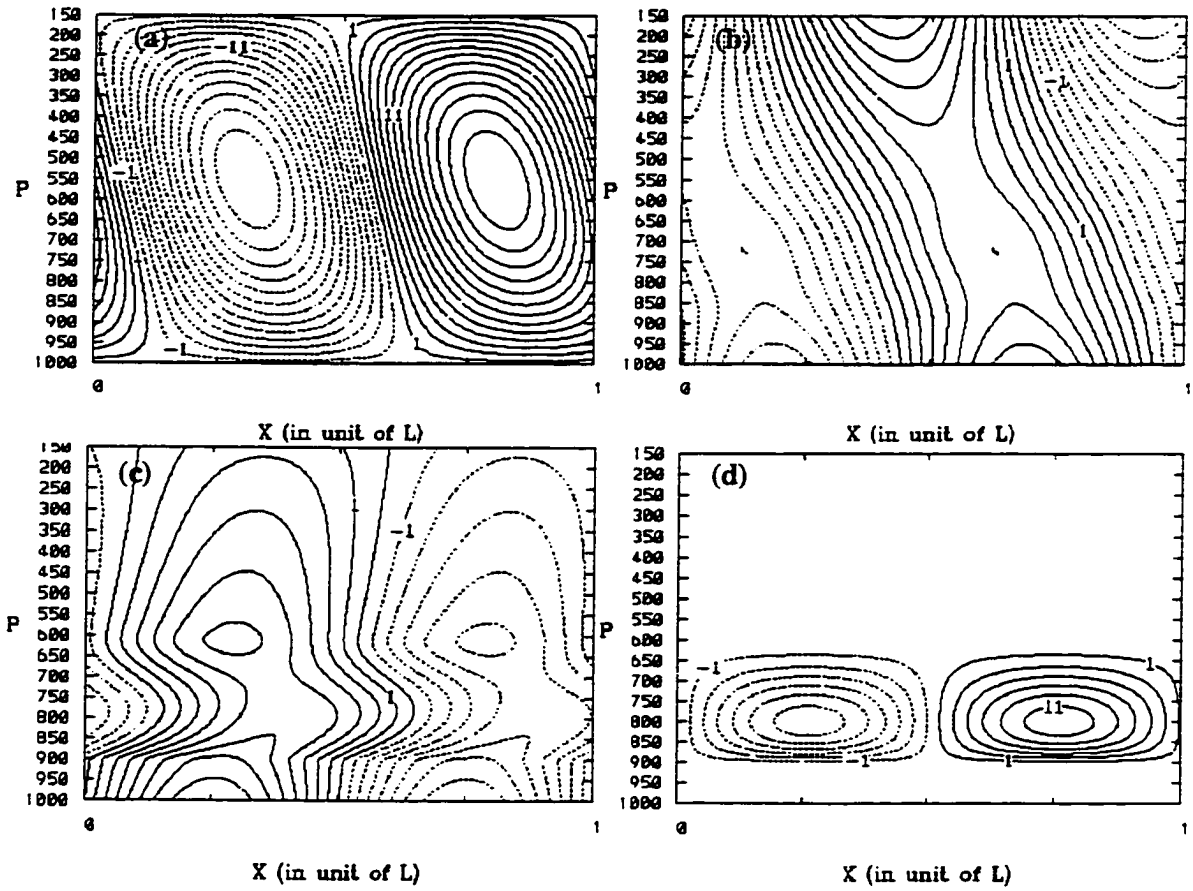

Figure 2.15 Result of the T-parameterization model, the vertical-horizontal cross-section of (a) vertical velocity ω, (b) streamfunction ψ, and (c) temperature T for wavenumber k=0.9, for heating intensity ε_T=0.1.

maximum of vertical velocity rises into the upper atmosphere so the vertical velocity field becomes vertically asymmetic (Fig. 2.15(a)). In streamfunction field (Fig. 2.15(b)), the local center near 700hPa is further developed in the region from 600hPa to 900hPa. Above or below this region, the wave still retains some features of the Eady mode but it is modified because of the new boundary conditon due to strong convective heating. This is also shown in temperature field (Fig. 2.15(c)). We see three temperature wave patterns in three regions. The wave in the middle differs from the Eady mode, and it separates two Eady-mode like waves in the upper and lower atmosphere. Wave's temperature structure is significantly changed by convective heating.

Table 2-3 gives the phase angle difference for different heating parameters between vertical-velocity wave and temperature wave at the level where vertical velocity wave amplitude reaches the maximum. As with the v-parameterization, when the convective heating parameter increases, the wave structure changes and the warm (cold) region shifts away from the ascent (descent) motion region, so that the wave does not convert EPE to EKE as effectively thus cannot grow as fast as the dry case. With further increase in ε_T, the phase angle difference increases. When $\varepsilon_T > 0.8$, the warm and cold regions again align with the ascent and descent motion regions.

4-3. Energetic analysis

Energetic analysis here is also based on the equations (36a) and (36b) but the diabatic heating due to surface sensible heat flux Q_2 is nonzero in this case. The energy budget terms of wavenumber k=0.9 for ε_T=0.0001 are shown in Figure 2.17. It is very similar to Figure 2.8 because the heating is negligible and the damping is confined mostly in the lower atmosphere.

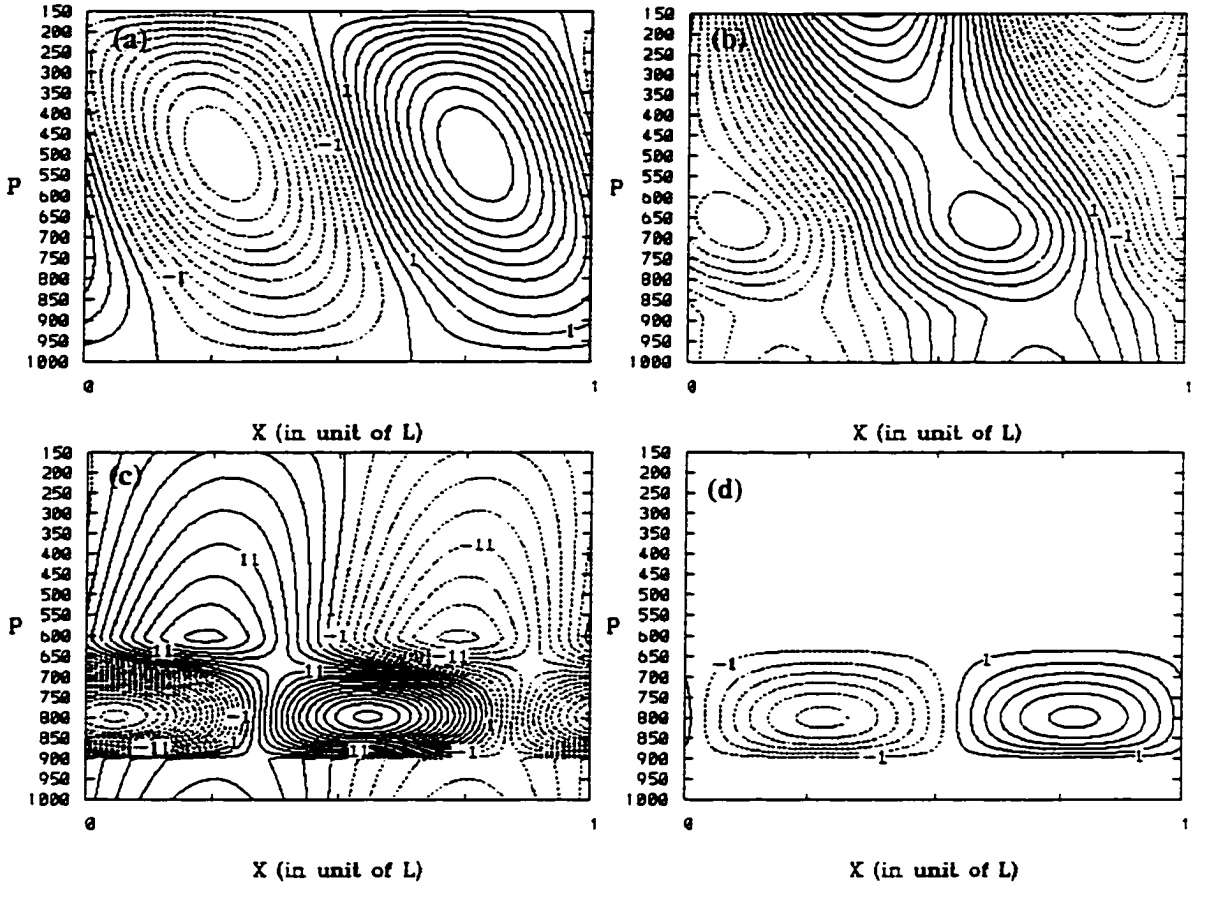

Figure 2.16 Result of the T-parameterization model, the vertical-horizontal cross-section of (a) vertical velocity ω, (b) streamfunction ψ, and (c) temperature T for wavenumber k=0.9, for heating intensity ε_T=1.0.

TABLE 2-3 Result of the T-parameterization model, phase angle difference between vertical velocity wave and temperature wave at the level where vertical velocity wave amplitude is largest

ε_T	p at max(Ω)	Phase difference (T-Ω)
0.0001	587.8 hPa	181.6
0.01	583.5 hPa	180.2
0.1	524.0 hPa	128.8
0.2	528.2 hPa	168.6
0.4	502.8 hPa	172.9
0.6	485.8 hPa	177.0
0.8	473.0 hPa	179.7
1.0	460.2 hPa	181.0

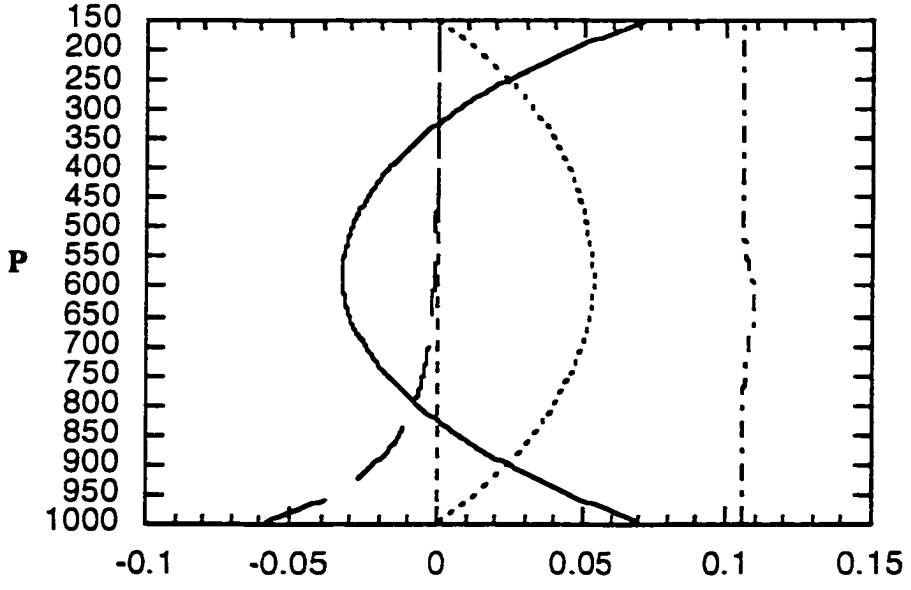

Figure 2.17 Result of the T-parameterization model, energy budget terms of wavenumber k=0.9 for ε_T=0.0001. Solid line denotes DIV[EE], dotted line represents C[EPE,EKE], dash-dotted line is for C[ZPE,EPE], short dashed line for G[CONV], and long dashed line for contribution of surface damping G[DAMP].

Figure 2.18 shows the energy budget terms of wavenumber k=0.9 for ε_T=0.1. Above the cloud base, as we can see, the vertical distributions of DIV[EE], C[EPE,EKE], and C[ZPE,EPE] change relative to the Eady case, however, the eddy still grows baroclinically, drawing energy from both the ZPE reservoir and the EPE reservoir.

The change of energy budget terms with convective heating intensity can be partially understood in Figure 2.19, where

$$G^*[DAMP] = \frac{G[DAMP]}{C[ZPE, EPE]}.$$

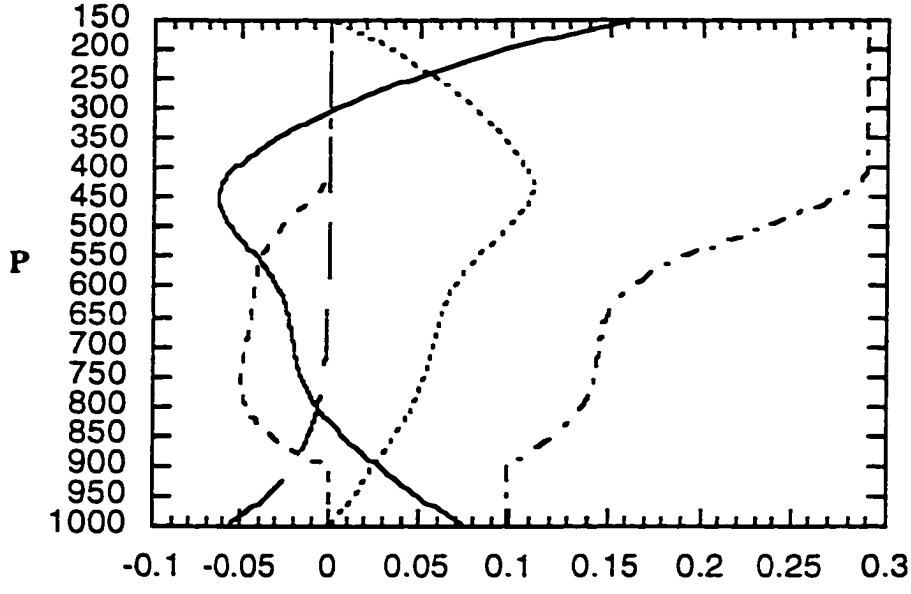

Figure 2.18 Same as Fig. 2.17 except for ε_T=0.1.

As we can see, with moderate heating ($\varepsilon_T < 0.2$), C[EPE,EKE] decreases while the negative contribution of convection becomes larger. Then, the magnitude of G[CONV] decreases when C[EPE,EKE] decreases, and it becomes positive when ε_T is about 2.0 then turns to negative again. With increasing ε_T in Figure 2.16, the magnitude of G[DAMP] becomes comparable to G[CONV].

As we have seen, the result using T-parameterization exhibits qualitatively the same behavior as that using the v-parameterization. With weak convection, the wave's structure does not change much while the EPE generation decreases due to negative contribution of

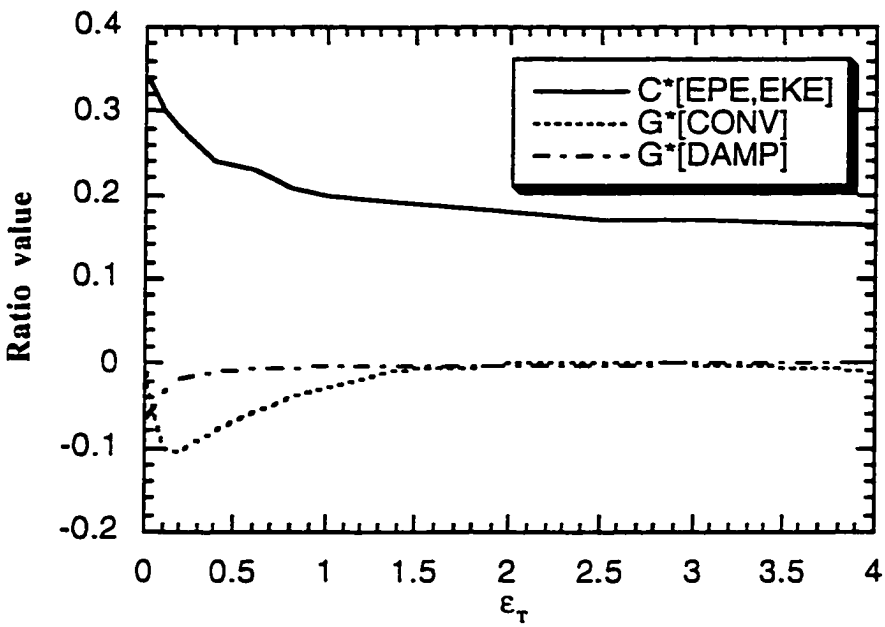

Figure 2.19 Result of the T-parameterization model, the vertically-integrated energy budget terms of wavenumber k=0.9 for different heating intensity

convection. In the presence of moderate convective heating, although the EPE generation still decreases, the wave's structure changes accordingly to minimize the negative effect of convection. Contribution of convection becomes a small positive value when ε_T is about 2.0. In contrast to the result using the v-parameterization, G[CONV] becomes negative with further increasing heating.

4-4. Sensitivity Experiments

Sensitivity experiments were performed to examine the influences of cloud parameters. We first change the value of p_B while keeping $p_m = p_B$ and fixing other parameters to the reference values. It is found that the most unstable wavenumber does not change with the cloud base, and the growth rate of the most unstable wave with ε_T=0.1 increases slightly from 0.145 for p_B=0.9 to 0.148 for p_B=0.96. When only cloud top changes and other parameters are fixed to the reference values , the growth rate of the most unstable wave with lower cloud top is larger (Table 2-4). This is also seen in Wang and Barcilon (1986). In our case, however, the most unstable wavenumber does not change with cloud top height, which is in contrast to the result in Wang and Barcilon (1986). Also similar to Wang and Barcilon (1986), the instability changes slightly with the different heating profile when the cloud top and base are fixed to the reference value (Table 2-5).

Because the top of the unstable PBL is not necessarily the cloud base, we also perform experiments changing p_m while fixing other parameters to the reference value. The result shows small instability change when p_m changes from 0.85 to 0.92. considering the top of the unstable PBL (p_m) as the lifting condensation level and the cloud base as the free convection level, it would be unphysical to change p_m too far from the cloud base.

TABLE 2-4 Wavenumber and growth rate of the most unstable wave for each experiment with different cloud top level and ε_T=0.1

p_T	k_{max}	g_{max}
0.3	1.0	0.133
0.4	1.0	0.145
0.5	1.0	0.155
0.6	1.0	0.160

TABLE 2-5 Wavenumber and growth rate of the most unstable wave for each experiment with different heating profile and ε_T=0.1

b	k_{max}	g_{max}
0.0	1.0	0.121
0.5	1.0	0.131
1.0	1.0	0.145

Summary

We have conducted a theoretical, linear analysis of the moist instability of a baroclinic zonal flow in the presence of surface temperature damping. The effect of surface temperature damping is assumed to exponentially decrease with height. The cumulus convective heating is incorporated into the two-dimensional continuous model in an f-plane in terms of either (1) eddy meridional velocity (v-parameterization) or (2) eddy temperature (T-paramterization) at a certain level p_m which approximately is the top of the unstable boundary layer, with heating in the wave's cold sector. We have analytically derived the general dispersion equation and eigenfunction in terms of the homogeneous fundamental solutions. We have obtained the analytical solutions for a zonal flow with constant vertical shear, static stability, and a representative heating profile.

Both the v-parameterization and T-parameterization give the similar result. The moist unstable waves are modified by the effect of convective latent heating. With weak convection, the wave's structure does not change much while the wave's energy generation is hampered by the negative contribution of convection. In the presence of moderate convective heating, although the wave's energy's generation is decreased by the convection, the wave adjusts its structure accordingly to minimize the negative effect of convection and keep growing.

For strong convective heating, two parameterization schemes give different scenarios. Using the v-parameterization, the wave's structure changes so much that the wave adapts itself to draw its energy from the positive contribution of convection, and the growth rate and phase speed increases. With the T-parameterization scheme, convection contribution to the EPE generation becomes a small positive value when ε_T is about 2.0 and it turns negative with further increasing heating. Strong convective heating invokes a

non-Eady mode in the cloud region which separates and modifies the Eady mode in the upper and lower atmosphere.

References

Balasubramanian, G., and M. K. Yau, 1994: Baroclinic instability in a two-layer model with parameterized slantwise convection. *J. Atmos. Sci.*, **51**, 971-990.

Bannon, P. R., 1986: Linear development of quasi-geostrophic baroclinic disturbances with condensational heating. *J. Atmos. Sci.*, **43**, 2261-2274.

Emanuel, K. A., M. Fantini and A. J. Thorpe, 1987: Baroclinic instability in an environment of small stability to slantwise moist convection. Part I: Two-dimensional models. *J. Atmos. Sci.*, **44**, 1559-1573.

Fantini, M., 1990: Nongeostrophic corrections to the eigensolutions of a moist baroclinic instability problem. *J. Atmos. Sci.*, **47**, 1277-1287.

Farrell, B. F., 1982: The initial growth of disturbances in a baroclinic flow. *J. Atmos. Sci.*, **47**, 1277-1287.

Jiang, W., 1994: The role of convection in eddy life cycles. M.S. Thesis, Iowa State University, 86 pp.

Mak, M., 1982: On moist quasi-geostrophic baroclinic instability. *J. Atmos. Sci.*, **39**, 2028-2037.

Mak, M., 1983: On moist quasi-geostrophic baroclinic instability in a general model. *Sci. Sin.*, **B26**, 850-864.

Mak, M., 1994: Cyclogenesis in a conditionally unstable moist baroclinic atmosphere. *Tellus*, **46A**, 14-33.

Moorthi, S., and A. Arakawa, 1985: Baroclinic instability with cumulus heating. *J. Atmos. Sci.*, **42**, 2007-2031.

Tokioka, T., 1973: A stability study of medium-scale disturbances with inclusion of convective effects. *J. Meteor. Soc. Japan*, **51**, 1-10.

Wang, B., and A. Barcilon, 1986: Moist stability of a baroclinic zonal flow with conditionally unstable stratification. *J. Atmos. Sci.*, **43**, 705-719.

GENERAL CONCLUSION

This study investigates the coupling of baroclinic waves, cumulus convection, and surface processes through numerical experiments and a linear analysis of moist instability. In the first paper, the role of convection in the dynamics of eddy life cycles has been examined through numerical experiments using initial states that are baroclinically and conditionally unstable in midlatitudes. The location of wave-induced convection and its influence on the growing wave depends on how strongly the wave is coupled to the lower boundary through surface fluxes. For simulations using Emanuel convection, the relatively shallow convection plays a central role in a water cycle wherein (1) evaporation gives moisture to the cold sector's boundary layer, (2) convection pumps some of the moisture into the lower troposphere above the boundary layer, (3) the large-scale circulation transports the moisture eastward and upward into the wave's warm sector, and (4) stable precipitation condenses the moisture into precipitation. The additional condensation catalyzes a more energetic life cycle by inducing stronger vertical motion and, hence, a greater conversion of available potential energy to kinetic energy. This enhancement is parameterization-dependent, with the key factor being how much lower-tropospheric moistening a convection scheme produces.

Motivated by the results of the first paper, we then conduct a theoretical, linear analysis of the moist instability of a baroclinic zonal flow with conditionally unstable stratification in the presence of surface temperature damping, which is the second paper of this dissertation. In this theoretical study, the effect of surface temperature damping is assumed to decrease exponentially with height, and cumulus convective heating is incorporated into a two-dimensional, continuous f-plane model in terms of either (1) eddy meridional velocity (v-parameterization) or (2) eddy temperature (T-parameterization) at a

certain level p_m which approximately is the top of the unstable boundary layer with heating in the wave's cold sector. In the v-parameterization, convective heating rate is assumed to be proportional to eddy meridional velocity at the top of the unstable PBL; In the T-parameterization, convective heating is related to eddy temperature at the top of the unstable PBL. The general dispersion equation and eigenfunction were derived analytically, then analytical solutions were obtained for a zonal flow with constant vertical shear and static stability and a representative convective heating profile. Both the v-parameterization and T-parameterization showed that moist unstable waves are modified by the effect of convective latent heating. With weak convection, the wave's structure does not change much while the wave's energy cycle is hampered by the negative contribution of convection. In the presence of moderate convective heating, although the wave's energy is depleted by convection, the wave adjusts its structure to minimize the negative effect of convection and keep growing. Strong convective heating invokes a non-Eady mode in the cloud region which separates and modifies the Eady mode in the upper and lower atmosphere.

The instability study of the second paper could not include the effect of convective moistening, but it confirms the negative coupling between the wave and convective heating in the wave's cold sector. This implies that the enhancement found in the numerical experiment of the first paper is not related to the direct thermodynamic effect of convective heating, but is rather an effect of the wave's hydrological cycle related to convective moistening. To further investigate the hypothesized wave-enhancing mechanism described in this study, a future study has been proposed using a high resolution mesoscale model (MM5 or the Eta model) to simulate some observed cases and diagnose the hydrological cycle. The proposed mesoscale numerical study would include simulating one or more extensively observed cases of oceanic cyclone development. The candidate cases would be drawn from intensive observing periods (IOPs) of recent field campaigns, focusing on episodes of cyclone development that exhibited significant convective activity and surface

heat fluxes. Simulations including both convection and surface heat fluxes would be compared with those that exclude surface heat fluxes, convection or both. The focus of the simulations would be surface evaporation, cumulus convection, and moisture transport to different regions during wave development. The interaction between surface sensible heat flux and lower atmosphere temperatures and the modulation of this interaction by convective heating effect on PBL structure would also be investigated.

APPENDIX A. TRAJECTORY ANALYSIS IN PAPER I

The method of trajectory analysis used in the first paper follows that of Kida (1983). Integrating the kinematical relation of velocity, we have

$$\delta\bar{r}(a,\delta t) = \bar{r}_1 - \bar{r}_0 = \int_{t_0}^{t_1} \bar{v}(a,t)dt,$$

where t denotes time, subscripts 0 and 1 stand for initial and final time points of the integration, and **a** is a "name" of the marked air parcel. $\delta\bar{r}(a,\delta t)$ is the 3-D displacement vector of the air parcel labeled **a** for the period of $\delta t = t_1 - t_0$. $\bar{v}(a,t)$ is the 3-D velocity vector of the air parcel **a** at time t. For a specific time point, $\bar{v}(a,t)$ can be replaced by the Eulerian field $\bar{v}(\bar{r},t)$ using the current position $\bar{r}$ of the air parcel.

For a short time period, the time integral can be approximated by the arithmetic average,

$$\int_{t_0}^{t_1} \bar{v}(\bar{r},t)dt \approx \frac{1}{2}\{\bar{v}(\bar{r}_0,t_0) + \bar{v}(\bar{r}_1,t_1)\}\delta t.$$

Then, we can write

$$\bar{r}_1 = \bar{r}_0 + \frac{1}{2}\{\bar{v}(\bar{r}_0,t_0) + \bar{v}(\bar{r}_1,t_1)\}\delta t, \qquad \text{(A1)}$$

which is an implicit form with respect to $\bar{r}_1$.

Using the above equation, we compute the position of an air parcel at every time step of the model (15 minutes), and the procedure is as follows:

(1) Release an air parcel from $\vec{r}_0$ at time t_0. Estimate the wind vector $\vec{v}(\vec{r}_0, t)$ by linear interpolation in space, if necessary.

(2) Initially assume $\vec{v}(\vec{r}_1, t_1) = \vec{v}(\vec{r}_0, t_1)$ and use (A1) to estimate $\vec{r}_1$.

(3) Obtain the wind vectors at the eight grid points of the grid box that contains the estimated $\vec{r}_1$.

(4) Compute the wind vector $\vec{v}(\vec{r}_1, t_1)$ by linear interpolation in space.

(5) Use (A1) to estimate $\vec{r}_1$.

(6) Repeat steps (3) to (5) until it converges.

The convergence condition used in the computation is

$$\vec{r} = (\lambda, \phi, \sigma),$$
$$\left|\lambda_1^m - \lambda_1^{m-1}\right| / \left|\lambda_1^m - \lambda_1^0\right| < 10^{-2},$$
$$\left|\phi_1^m - \phi_1^{m-1}\right| / \left|\phi_1^m - \phi_1^0\right| < 10^{-2}$$
$$\left|\sigma_1^m - \sigma_1^{m-1}\right| / \left|\sigma_1^m - \sigma_1^0\right| < 10^{-3},$$

where λ, ϕ, σ respectively denote longitude, latitude, and the vertical ordinate; the superscript represents the number of times in iteration.

APPENDIX B. TWO LINEARLY INDEPENDENT SOLUTIONS, f_1 AND f_2

In terms of the two fundamental solutions $\Omega_1(p)$ and $\Omega_2(p)$, the general solution of the homogeneous equation (16) can be expressed as

$$G(p) = S_1\Omega_1(p) + S_2\Omega_2(p) \tag{B1}$$

where S_1 and S_2 are two arbitrary constants.

Apply the upper boundary condition (13):

$$G(p_U) = S_1\Omega_1(p_U) + S_2\Omega_2(p_U) = 0.$$

Then,

$$S_1 = -S_2\Omega_2(p_U) / \Omega_1(p_U).$$

Thus,

$$G(p) = \frac{-S_2}{\Omega_1(p_U)}(\Omega_2(p_U)\Omega_1(p) - \Omega_1(p_U)\Omega_2(p)).$$

For convenience, choose $S_2 = -\Omega_1(p_U)$. we then have the solution

$$f_2(p) = \Omega_2(p_U)\Omega_1(p) - \Omega_1(p_U)\Omega_2(p),$$

which satisfies the upper boundary condition.

In a similar manner, applying the lower boundary condition (14) to (B1), we obtain the solution satisfying the lower boundary condition:

$$f_1(p) = \Omega_2(p_L)\Omega_1(p) - \Omega_1(p_L)\Omega_2(p).$$

The Wronskian

$$\begin{aligned} W_R(f_1, f_2; p) &\equiv f_1(p)f_2'(p) - f_1'(p)f_2(p) \\ &= \Omega_1(p_L)\Omega_2(p_U)\left[\Omega_2(p)\Omega_1'(p) - \Omega_1(p)\Omega_2'(p)\right] \\ &\quad - \Omega_2(p_L)\Omega_1(p_U)\left[\Omega_2(p)\Omega_1'(p) - \Omega_1(p)\Omega_2'(p)\right] \\ &= \left[\Omega_1(p_L)\Omega_2(p_U) - \Omega_2(p_L)\Omega_1(p_U)\right]\left[\Omega_2(p)\Omega_1'(p) - \Omega_1(p)\Omega_2'(p)\right] \\ &= -f_1(p_U)W(p), \end{aligned}$$

where

$$W(p) \equiv \left[\Omega_2(p)\Omega_1'(p) - \Omega_1(p)\Omega_2'(p)\right].$$

Since the two fundamental solutions Ω_1 and Ω_2 are linearly independent, $W(p) \neq 0$. Therefore, for non-Eady solutions [$f_1(p_U) \neq 0$], $W_R(f_1, f_2; p) \neq 0$ and f_1 and f_2 are linearly independent.

APPENDIX C. TWO LINEARLY INDEPENDENT SOLUTIONS OF EQUATION (12) WITHOUT HEATING IN PAPER II

In the absence of convective heating, (12) becomes

$$\frac{d^2\Omega}{dp^2}+\frac{2\lambda}{F(p)}\frac{d\Omega}{dp}-k^2\sigma\Omega=\frac{i\gamma p_m\xi(p)}{kpF^2(p_m)}\left[F(p_m)\frac{d^2\Omega(p_m)}{dp^2}+\lambda\frac{d\Omega(p_m)}{dp}\right]. \tag{C1}$$

Now, the method of variation of parameters can be applied to solve the above equation in terms of $f_1(p)$ and $f_2(p)$(see Appendix B).

Assume the solution has the form $\Omega(p)=A_1(p)f_1(p)+B_1(p)f_2(p)$. Then

$$A_1'(p)=\frac{i\gamma p_m}{kF^2(p_m)}\left[F(p_m)\frac{d^2\Omega(p_m)}{dp^2}+\lambda\frac{d\Omega(p_m)}{dp}\right]\frac{\xi(p)f_2(p)}{pW_R(f_1,f_2;p)},$$

$$B_1'(p)=\frac{-i\gamma p_m}{kF^2(p_m)}\left[F(p_m)\frac{d^2\Omega(p_m)}{dp^2}+\lambda\frac{d\Omega(p_m)}{dp}\right]\frac{\xi(p)f_1(p)}{pW_R(f_1,f_2;p)}.$$

Integrating vertically, we have

$$A_1(p)=\frac{i\gamma p_m}{kF^2(p_m)f_1(p_U)}\left[F(p_m)\frac{d^2\Omega(p_m)}{dp^2}+\lambda\frac{d\Omega(p_m)}{dp}\right]\int_{p_U}^{p}\frac{\xi(t)f_2(t)}{tW(t)}dt+\tilde{A}_1,$$

$$B_1(p)=\frac{-i\gamma p_m}{kF^2(p_m)f_1(p_U)}\left[F(p_m)\frac{d^2\Omega(p_m)}{dp^2}+\lambda\frac{d\Omega(p_m)}{dp}\right]\int_{p_U}^{p}\frac{\xi(t)f_1(t)}{tW(t)}dt+\tilde{B}_1.$$

Using the upper and lower boundary conditions, we know that $A_1(p_U)=0$ and $B_1(p_L)=0$, which are used to determine the integrating constants, $\tilde{A}_1=0$, and

$$\tilde{B}_1 = \frac{i\gamma p_m}{kF^2(p_m)f_1(p_U)}\left[F(p_m)\frac{d^2\Omega(p_m)}{dp^2} + \lambda\frac{d\Omega(p_m)}{dp}\right]\int_{p_U}^{p_L}\frac{\xi(t)f_1(t)}{tW(t)}dt.$$

Then, we can write the following

$$A_1(p) = \frac{i\gamma p_m}{kF^2(p_m)f_1(p_U)}\left[F(p_m)\frac{d^2\Omega(p_m)}{dp^2} + \lambda\frac{d\Omega(p_m)}{dp}\right]\int_{p_U}^{p}\frac{\xi(t)f_2(t)}{tW(t)}dt,$$

$$B_1(p) = \frac{-i\gamma p_m}{kF^2(p_m)f_1(p_U)}\left[F(p_m)\frac{d^2\Omega(p_m)}{dp^2} + \lambda\frac{d\Omega(p_m)}{dp}\right]\int_{p_L}^{p}\frac{\xi(t)f_1(t)}{tW(t)}dt.$$

Now, we need to know $\frac{d\Omega(p_m)}{dp}$ and $\frac{d^2\Omega(p_m)}{dp^2}$.

It is easy to see that $A_1'(p)f_1(p) + B_1'(p)f_2(p) = 0$, so

$$\begin{aligned}\frac{d\Omega(p_m)}{dp} &= A_1(p_m)f_1'(p_m) + B_1(p_m)f_2'(p_m)\\ &= \frac{i\gamma p_m}{kF^2(p_m)f_1(p_U)}\left[F(p_m)\frac{d^2\Omega(p_m)}{dp^2} + \lambda\frac{d\Omega(p_m)}{dp}\right]\\ &\quad\times\left[f_1'(p_m)\int_{p_U}^{p_m}\frac{\xi(t)f_2(t)}{tW(t)}dt - f_2'(p_m)\int_{p_U}^{p_m}\frac{\xi(t)f_1(t)}{tW(t)}dt\right].\end{aligned}$$

Let us define

$$M_1 \equiv \frac{i\gamma p_m}{kF^2(p_m)f_1(p_U)}\int_{p_U}^{p_m}\frac{\xi(t)f_1(t)}{tW(t)}dt,$$

$$M_2 \equiv \frac{i\gamma p_m}{kF^2(p_m)f_1(p_U)}\int_{p_m}^{p_L}\frac{\xi(t)f_2(t)}{tW(t)}dt.$$

Then, we can arrive at

$$\frac{d\Omega(p_m)}{dp} = \frac{F(p_m)\left[f_1'(p_m)M_2 + f_2'(p_m)M_1\right]}{1-\lambda\left[f_1'(p_m)M_2 + f_2'(p_m)M_1\right]}\frac{d^2\Omega(p_m)}{dp^2}. \tag{C2}$$

Similarly,

$$\frac{d^2\Omega(p)}{dp^2} = A_1''(p)f_1(p) + 2A_1'(p)f_1'(p) + A_1(p)f_1''(p)$$
$$+B_1''(p)f_2(p) + 2B_1'(p)f_2'(p) + B_1(p)f_2''(p).$$

Manipulating the expressions of $A(p)$, $A'(p)$, $A''(p)$, $B(p)$, $B'(p)$, and $B''(p)$, we find

$$\frac{d^2\Omega(p_m)}{dp^2} = A_1'(p_m)f_1'(p_m) + B_1'(p_m)f_2'(p_m) + A_1(p_m)f_1''(p_m) + B_1(p_m)f_2''(p_m)$$
$$= \frac{-i\gamma\xi(p_m)}{kF^2(p_m)}\left[F(p_m)\frac{d^2\Omega(p_m)}{dp^2} + \lambda\frac{d\Omega(p_m)}{dp}\right] + \left[f_1''(p_m)M_2 + f_2''(p_m)M_1\right]. \tag{C3}$$

Substituting (C2) into (C3), we finally obtain

$$\frac{d^2\Omega(p_m)}{dp^2} = \frac{\lambda kF^2(p_m)\left[f_1''(p_m)M_2 + f_2''(p_m)M_1\right] - i\gamma\lambda\xi(p_m)}{kF(p_m) - kF^2(p_m)\left[f_1''(p_m)M_2 + f_2''(p_m)M_1\right] + i\gamma\xi(p_m)}$$
$$\times\frac{f_1'(p_m)M_2 + f_2'(p_m)M_1}{1-\lambda\left[f_1'(p_m)M_2 + f_2'(p_m)M_1\right]}. \tag{C4}$$

We know that the general solution for (C1) can be expressed as

$$\Omega(p) = C_1\Omega_1(p) + C_2\Omega_2(p) + A_1(p)f_1(p) + B_1(p)f_2(p),$$

where C_1 and C_2 are arbitrary constants. Applying the boundary conditions to the general solution, we can construct two solutions:

$$g_1(p) = \Omega_2(p_L)\Omega_1(p) - \Omega_1(p_L)\Omega_2(p) + A_1(p)f_1(p) + B_1(p)f_2(p)$$
$$= (A_1(p)+1)f_1(p) + B_1(p)f_2(p)$$

$$g_2(p) = \Omega_2(p_U)\Omega_1(p) - \Omega_1(p_U)\Omega_2(p) + A_1(p)f_1(p) + B_1(p)f_2(p)$$
$$= A_1(p)f_1(p) + (B_1(p)+1)f_2(p)$$

where $g_1(p)$ satisfies the lower boundary condition and $g_2(p)$ satisfies the upper boundary condition. It is straightforward to show the Wronskian

$$W_R(g_1, g_2; p) = (A_1(p) + B_1(p) + 1)W_R(f_1, f_2; p)$$
$$= f_1(p_U)W(p)(A_1(p) + B_1(p) + 1). \qquad \text{(C5)}$$

For non-Eady cases, the Wronskian can not be zero, therefore, $g_1(p)$ and $g_2(p)$ are two linearly independent solutions.

APPENDIX D. SOLVING EQUATION (12) IN PAPER II

Two linearly independent solutions of (C1), $g_1(p)$ and $g_2(p)$, are obtained in Appendix D. Now, the convective heating term can be viewed as a forcing term adding to (C1). Again, the method of variation of parameters can be used to solve the equation with forcing. Let us assume that the eigenfunction takes different forms below the cloud, inside the cloud, and above the cloud. Equation (24) is rewritten here for convenience:

$$\Omega(p) = \begin{cases} D_1 g_1(p), & p_L \geq p > p_B \\ A_2(p) g_1(p) + B_2(p) g_2(p), & p_B \geq p \geq p_T \\ D_2 g_2(p), & p_T > p \geq p_U \end{cases} \tag{D1}$$

where $A_2(p)$ and $B_2(p)$ are two undetermined functions, and D_1 and D_2 are constants to be determined. According to the interfacial continuity condition (15), we have

$$D_1 g_1(p_B) = A_2(p_B) g_1(p_B) + B_2(p_B) g_2(p_B),$$
$$D_2 g_2(p_T) = A_2(p_T) g_1(p_T) + B_2(p_T) g_2(p_T),$$
$$D_1 g_1'(p_B) = A_2(p_B) g_1'(p_B) + A_2'(p_B) g_1(p_B) + B_2(p_B) g_2'(p_B) + B_2'(p_B) g_2(p_B),$$
$$D_2 g_2'(p_T) = A_2(p_T) g_1'(p_T) + A_2'(p_T) g_1(p_T) + B_2(p_T) g_2'(p_T) + B_2'(p_T) g_2(p_T).$$

The solution is required to satisfy

$$B_2(p_B) = 0, \quad A_2(p_T) = 0, \quad D_1 = A_2(p_B), \quad D_2 = B_2(p_T),$$

and,

$$A_2'(p_B) g_1(p_B) + B_2'(p_B) g_2(p_B) = 0, \quad A_2'(p_T) g_1(p_T) + B_2'(p_T) g_2(p_T) = 0. \tag{D2}$$

Using the method of variation of parameters,

$$A_2'(p) = \frac{i\varepsilon p_m}{kF^2(p_m)}\left[F(p_m)\frac{d^2\Omega(p_m)}{dp^2} + \lambda\frac{d\Omega(p_m)}{dp}\right]\frac{\eta(p)g_2(p)}{pW_R(g_1,g_2;p)},$$

$$B_2'(p) = \frac{-i\varepsilon p_m}{kF^2(p_m)}\left[F(p_m)\frac{d^2\Omega(p_m)}{dp^2} + \lambda\frac{d\Omega(p_m)}{dp}\right]\frac{\eta(p)g_1(p)}{pW_R(g_1,g_2;p)}.$$

Integrating vertically, then,

$$A_2(p) = \frac{i\varepsilon p_m}{kF^2(p_m)}\left[F(p_m)\frac{d^2\Omega(p_m)}{dp^2} + \lambda\frac{d\Omega(p_m)}{dp}\right]\int_{p_T}^{p}\frac{\eta(t)g_2(t)}{tW_R(g_1,g_2;t)}dt + \tilde{A}_2,$$

$$B_2(p) = \frac{-i\varepsilon p_m}{kF^2(p_m)}\left[F(p_m)\frac{d^2\Omega(p_m)}{dp^2} + \lambda\frac{d\Omega(p_m)}{dp}\right]\int_{p_T}^{p}\frac{\eta(t)g_1(t)}{tW_R(g_1,g_2;t)}dt + \tilde{B}_2.$$

Applying $A_2(p_T) = 0$ and $B_2(p_B) = 0$, integration constants $\tilde{A}$ and $\tilde{B}$ can be determined as

$$\tilde{A}_2 = 0,$$

and

$$\tilde{B}_2 = \frac{i\varepsilon p_m}{kF^2(p_m)}\left[F(p_m)\frac{d^2\Omega(p_m)}{dp^2} + \lambda\frac{d\Omega(p_m)}{dp}\right]\int_{p_T}^{p_B}\frac{\eta(t)g_1(t)}{tW_R(g_1,g_2;t)}dt.$$

Thus, we can rewrite $A_2(p)$ and $B_2(p)$ as

$$A_2(p) = \frac{i\varepsilon p_m}{kF^2(p_m)}\left[F(p_m)\frac{d^2\Omega(p_m)}{dp^2} + \lambda\frac{d\Omega(p_m)}{dp}\right]\int_{p_T}^{p}\frac{\eta(t)g_2(t)}{tW_R(g_1,g_2;t)}dt \qquad \text{(D3)}$$

$$B_2(p) = \frac{-i\varepsilon p_m}{kF^2(p_m)}\left[F(p_m)\frac{d^2\Omega(p_m)}{dp^2} + \lambda\frac{d\Omega(p_m)}{dp}\right]\int_{p_B}^{p}\frac{\eta(t)g_1(t)}{tW_R(g_1,g_2;t)}dt \qquad \text{(D4)}$$

It is straightforward to prove that (D3) and (D4) satisfy (D2).

From $D_1 = A_2(p_B)$, $D_2 = B_2(p_T)$, we obtain the following relations:

$$D_1 - A_2(p_B) = D_1 - \frac{i\varepsilon p_m}{kF^2(p_m)}\left[F(p_m)\frac{d^2\Omega(p_m)}{dp^2} + \lambda\frac{d\Omega(p_m)}{dp}\right]\int_{p_T}^{p_B}\frac{\eta(t)g_2(t)}{tW_R(g_1,g_2;t)}dt = 0, \qquad \text{(D5)}$$

$$D_2 - B_2(p_T) = D_2 + \frac{i\varepsilon p_m}{kF^2(p_m)}\left[F(p_m)\frac{d^2\Omega(p_m)}{dp^2} + \lambda\frac{d\Omega(p_m)}{dp}\right]\int_{p_B}^{p_T}\frac{\eta(t)g_1(t)}{tW_R(g_1,g_2;t)}dt = 0. \qquad \text{(D6)}$$

Now, derive the expressions for $\frac{d\Omega(p_m)}{dp}$ and $\frac{d^2\Omega(p_m)}{dp^2}$:

(1) if $p_L \geq p_m > p_B$, we have the elevated convection case (cloud base is above the PBL top). From (D1),

$$\frac{d\Omega(p_m)}{dp} = D_1\dot{g_1}(p_m), \qquad \frac{d^2\Omega(p_m)}{dp^2} = D_1\ddot{g_1}(p_m).$$

(2) if $p_B \geq p_m \geq p_T$, we have the boundary layer case (cloud base is within the boundary layer). Since we know

$$\dot{A_2}(p) = \frac{i\varepsilon p_m}{kF^2(p_m)}\left[F(p_m)\frac{d^2\Omega(p_m)}{dp^2} + \lambda\frac{d\Omega(p_m)}{dp}\right]\frac{\eta(p)g_2(p)}{pW_R(g_1,g_2;p)},$$

and

$$B_2'(p) = \frac{-i\varepsilon p_m}{kF^2(p_m)}\left[F(p_m)\frac{d^2\Omega(p_m)}{dp^2} + \lambda\frac{d\Omega(p_m)}{dp}\right]\frac{\eta(p)g_1(p)}{pW_R(g_1,g_1;p)}.$$

from (D1), we can obtain

$$\begin{aligned}\frac{d\Omega(p)}{dp} &= A_2'(p)g_1(p) + A_2(p)g_1'(p) + B_2'(p)g_2(p) + B_2(p)g_2'(p)\\ &= D_1g_1'(p) + \frac{i\varepsilon p_m}{kF^2(p_m)f_1(p_U)}\left[F(p_m)\frac{d^2\Omega(p_m)}{dp^2} + \lambda\frac{d\Omega(p_m)}{dp}\right]\times\\ &\qquad \int_p^{p_B}\frac{\eta(t)(f_2'(p)f_1(t) - f_1'(p)f_2(t))}{tW(t)(A_1(p) + B_1(p) + 1)}dt.\end{aligned}$$

For brevity, we define

$$I_1(p) = \int^p \frac{\eta(t)g_1(t)}{tW(t)(A_1(t) + B_1(t) + 1)}dt,$$

$$I_2(p) = \int^p \frac{\eta(t)g_2(t)}{tW(t)(A_1(t) + B_1(t) + 1)}dt,$$

and

$$I(p) = g_2'(p)\left[I_1(p_B) - I_1(p)\right] - g_1'(p)\left[I_2(p_B) - I_2(p)\right].$$

Then,

$$\frac{d\Omega(p)}{dp} = D_1g_1'(p) + \frac{i\varepsilon p_m I(p)}{kF^2(p_m)}\left[F(p_m)\frac{d^2\Omega(p_m)}{dp^2} + \lambda\frac{d\Omega(p_m)}{dp}\right].$$

Now, we have

$$\frac{d\Omega(p_m)}{dp} = \frac{D_1 k f_1(p_U) F^2(p_m) g_1^{\cdot}(p_m) + i\varepsilon p_m I(p_m) F(p_m) \dfrac{d^2\Omega(p_m)}{dp^2}}{k f_1(p_U) F^2(p_m) - i\varepsilon p_m \lambda I(p_m)}. \tag{D7}$$

Similarly from (D1) and manipulating the expressions of $A_2(p)$, $A_2^{\cdot}(p)$, $A_2^{\cdot\cdot}(p)$, $B_2(p)$, $B_2^{\cdot}(p)$, and $B_2^{\cdot\cdot}(p)$,, we can obtain

$$\frac{d^2\Omega(p)}{dp^2} = D_1 g_1^{\cdot}(p) + i\varepsilon p_m \frac{pJ(p) - \eta(p) f_1(p_U)}{kpF^2(p_m) f_1(p_U)} \left[F(p_m) \frac{d^2\Omega(p_m)}{dp^2} + \lambda \frac{d\Omega(p_m)}{dp} \right].$$

where $J(p) = g_2^{\cdot\cdot}(p)\left[I_1(p_B) - I_1(p)\right] - g_1^{\cdot\cdot}(p)\left[I_2(p_B) - I_2(p)\right]$. Then we can write

$$\frac{d^2\Omega(p_m)}{dp^2} = \left\{ D_1 k p_m f_1(p_U) F^2(p_m) g_1^{\cdot\cdot}(p_m) + i\varepsilon\lambda p_m \left[p_m J(p_m) - \eta(p_m) f_1(p_U) \right] \frac{d\Omega(p_m)}{dp} \right\} \Big/ \left\{ p_m F(p_m) \left\{ k f_1(p_U) F(p_m) - i\varepsilon \left[p_m J(p_m) - \eta(p_m) f_1(p_U) \right] \right\} \right\}.$$

Substituting (D7) into the above, we finally obtain equation (23). Setting B_1 to 1 for convenience and applying equations (22) and (23) to equation (25) and (26), we get the dispersion equation (21) and express B_2 as equation (31). Then, it is straightforward to get the eigenfunction.

APPENDIX E. TWO FUNDAMENTAL SOLUTIONS OF EQUATION (16) IN PAPER II

Since the nondimensional zonal flow is U(p) = 1 - p, and $\lambda = 1$, (16) becomes

$$\frac{d^2\Omega}{dp^2} + \frac{2}{1-p-c}\frac{d\Omega}{dp} - \mu^2\Omega = 0,$$

or,

$$\frac{1}{\mu}\frac{d^2\Omega}{dp^2} + \frac{2}{\mu(1-p-c)}\frac{d\Omega}{dp} - \mu\Omega = 0. \tag{E1}$$

Let $q = \mu(1-p-c)$, then (E1) can be written as

$$\frac{d^2\Omega}{dq^2} + \frac{2}{q}\frac{d\Omega}{dq} - \Omega = 0. \tag{E2}$$

Assuming $\Omega_1(q) = (aq+b)e^q$, and substituting it into (E2), we can determine $a = -b$ for Ω_1 to be a solution. So, $\Omega_1(q) = a(q-1)e^q$ is a family of solutions with an arbitrary constant a.

Similarly, assuming $\Omega_2(q) = (mq+n)e^{-q}$, and substituting into (E2), we have $m = n$. So, $\Omega_2(q) = m(q+1)e^{-q}$ is another family of solutions with an arbitrary constant m.

Therefore, we obtain two families of fundamental solutions,

$$\Omega_1(p) = ae^{\mu(1-p-c)}[\mu(1-p-c)-1],$$

and

$$\Omega_2(p) = me^{-\mu(1-p-c)}[\mu(1-p-c)+1].$$

In order to utilize hypergeometric functions in the later derivations, the arbitrary constants a and m are chosen to be $1/\sqrt{2}$. Thus,

$$\Omega_1(p) = \frac{1}{\sqrt{2}} e^{\mu(1-p-c)}\left[\mu(1-p-c)-1\right],$$

and

$$\Omega_2(p) = \frac{1}{\sqrt{2}} e^{-\mu(1-p-c)}\left[\mu(1-p-c)+1\right].$$

ACKNOWLEDGMENTS

First of all, I thank God for letting me recover from my serious eye injury so that I can finish my Ph.D. study and visually appreciate the beauty of this world. I thank all my family members, especially my wife, for their support, encouragement, and understanding.

Many thanks go to my thesis advisor Dr. William J. Gutowski, Jr.. Without his continuos support and guidance, this graduate work at Iowa State University would not be possible. I would also like to thank other committee members, Dr. Tsing-Chang Chen, Dr. Gene Takle, Dr. Raymond Arritt, and Dr. John L. Stanford. Their comments are very appreciated.

Thanks also go to Dr. Zekai Otles, Dr. Richard Warren Turner, and Dr. Zaitao Pan who assisted with computer problems, graphing problems, and writing problems at one time or another.

This research was supported by NSF grants ATM-913522 and ATM-9616811 to Iowa State University and by an Iowa State Office of the Provost Global-Change Assistantship.

IMAGE EVALUATION
TEST TARGET (QA-3)

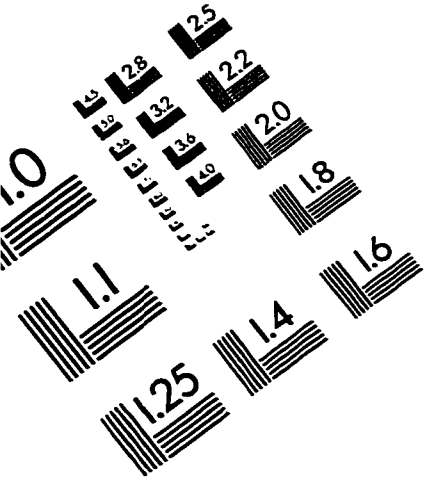

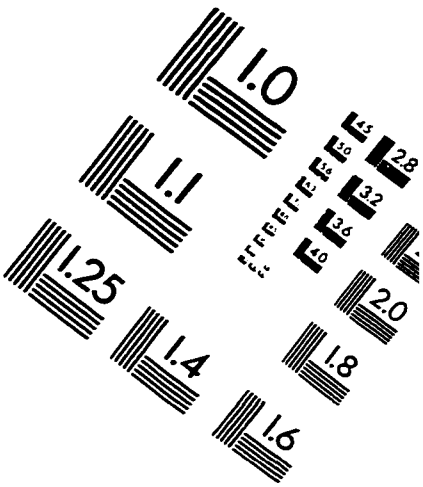

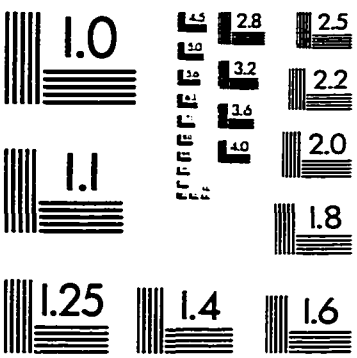

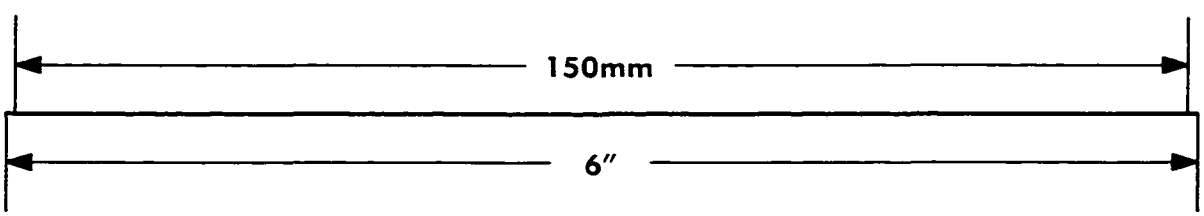

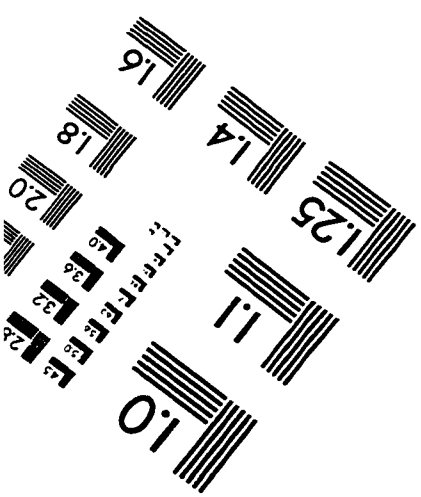

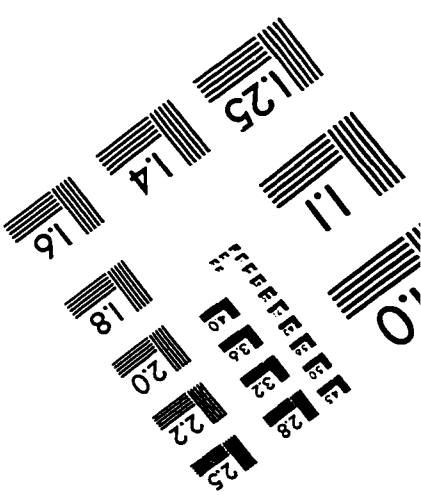

APPLIED IMAGE, Inc
1653 East Main Street
Rochester, NY 14609 USA
Phone: 716/482-0300
Fax: 716/288-5989